Error estimation and adaptive meshing in strongly nonlinear dynamic problems

Thesis by

Raúl A. Radovitzky

Civil Engineer, University of Buenos Aires, Argentina, 1991

M Sc Applied Mathematics, Brown University, USA, 1995

In Partial Fulfillment of the Requirements

for the Degree of

Doctor of Philosophy

California Institute of Technology

Pasadena, California

1998

(Submitted May 21, 1998)

Acknowledgements

I would especially like to express my deep gratitude to my advisor, Prof. Michael Ortiz, for his patience, guidance and support. His inexhaustible wealth of ideas is but one of the many reasons for my admiration.

I am thankful for the support of the Office of Naval Research under grant N00014–96–1–0068 and of the Sandia National Laboratories through contract DE–AC04–76DP00789.

I shall always be grateful to Prof. Eduardo Dvorkin at the University of Buenos Aires for his mentorship.

My former professors at Brown University: L.B. Freund, D. Gottlieb, G. Karniadakis, D. Pathria and C.F. Shih deserve my deep appreciation. I am equally indebted to my professors at Caltech: J. Knowles, A. Leonard, G. Ravichandran and A. Rosakis.

To Enrique, Margo, Maria, Minia and Juan from Brown University I not only owe the enjoyment of my first two years in graduate school but mostly their warm friendship.

I would also like to thank Gustavo Gioia, Eduardo Repetto and David Owen for their help and encouragement.

I will be eternally grateful to Roberto, Leticia, Mari, Gabi and Ricky to whom I not only owe their love and support, but mostly the sheer joy of being part of the same family.

To my wife Flavia for her unconditional support and love and to our son Felipe for bringing further joy to our lives

Abstract

This dissertation is concerned with the development of a general computational framework for mesh adaption such as is required in the three-dimensional lagrangian finite element simulation of strongly nonlinear, possibly dynamic, problems. It is shown that, for a very general constitutive framework, the solutions of the incremental boundary value problem obey a *minimum principle*, provided that the constitutive updates are formulated appropriately. This minimum principle is taken as a basis for asymptotic error estimation. In particular, we chose to monitor the error of a lower-order projection of the finite element solution. The optimal mesh size distribution then follows from *a posteriori* error indicators which are purely local, i. e., can be computed element-by-element.

A *sine qua non* condition for the successful accomplishment of the kind of analysis envisioned in this work is the possibility to mesh the deforming domains of analysis. In the first section of this thesis a method is presented for mesh generation in complex geometries and general—possibly non-manifold—topologies.

The robustness and versatility of the computational framework is demonstrated with the aid of convergence studies and selected examples of application and the results contrasted with previous approaches.

Contents

List of Figures

List of Tables

Chapter 1 Introduction

The response of solids and structures often exhibits structure on multiple length scales. This may be due to a variety of causes including: i) material heterogeneity, e. g., polycrystals, composites; ii) the simultaneous operation of interacting mechanisms possessing vastly disparate characteristic lengths, e. g., macroscopic single-crystal plasticity and dislocation mechanics; iii) instabilities stemming from a lack of convexity of the problem and leading to the development of microstructure, e. g., localization, martensitic transformations, dislocation-cell formation; iv) strong discontinuities in the solution made possible by the hyperbolicity of the problem, e. g., shocks, slip lines. Of course, these categories are not strictly disjoint. For instance, dislocations may be regarded as microstructures resulting from the lack of convexity of the strain-energy density of the crystal lattice; the onset of localization may be understood as a change of type of the problem. Often, the response at the small– or microscopic–length scale determines the behavior of the system at the large–or macroscopic–length scale. The simultaneous resolution of both scales then stems from a desire to root theories of macroscopic behavior directly on first principles of micromechanics, a long-standing aspiration of solid mechanics.

A number of basic strategies have been developed for bridging length scales in solids. One of these strategies revolves around the concept of effective macroscopic behavior. In this approach, the local values of the macroscopic fields are taken to constrain the microscopic fields on *average*. The macroscopic response may then be obtained by recourse to the tools and principles of homogenization and nonlinear analysis (e. g., [32, 112]). For instance, in the case of martensite and single crystal plasticity, the effective macroscopic behavior of the material may be approximated analytically by sequential lamination and energy minimization [66, 106]. The effective macroscopic behavior thus obtained may then be built into conventional finite elements and the subsequent analysis takes place entirely at the macroscopic level

[21, 22]. Alternatively, the macroscopic effective behavior of one element, and by extension of the material, may be approximated by introducing incompatible modes [102, 12, 40, 99, 71, 72, 73, 41], local base functions [59, 56], or other enhancements [128, 101, 2] into the finite elements. These local fields are constrained on average by the conventional element shape functions, and the corresponding degrees of freedom may be eliminated locally by static condensation or a similar device.

An example of this approach is the enhanced elements developed by Ortiz *et al.* [102, 99, 71, 72, 73] for capturing localized shear bands. These elements contain an additional incompatible mode consisting of two variants, namely, the shear band material and the surrounding unloaded matrix, separated by a plane of strain discontinuity. In Ortiz *et al* [102] implementation of the method, the orientation of the plane of discontinuity, follows from a local Hill-Hadamard analysis of the acoustic tensor, which in essence amounts to linearized energy minimization. The amplitudes of the modes are eliminated at the element level, resulting in a much softer–and mesh-orientation independent–response of the element. Because the local modes contain two variants, they may be regarded as instances of lamination.

As is well-known from the mathematical theory of martensitic transformations [8, 32], in a local solid the number of layers in the laminate is immaterial as regards the overall effective behavior: only the volume fractions of the variants matter. Thus, in the case of localization, the critical variable is the ratio of the areas covered by the unstable shear band material and the stable unloaded matrix. From this perspective, variations of the approach based on the introduction of one or more discrete bands into an element [102, 12, 101, 2] may be regarded as fundamentally equivalent. It bears emphasis that the introduction of local element enhancements simply amounts to an explicit numerical construct for the approximation of the effective macroscopic behavior of the material. Indeed, as pointed out by Leroy *et al.* [74], it is possible to obtain an effect identical to the element enhancement by using conventional shape functions and a suitable set of effective constitutive relations which only depend on the volume fractions of shear band and matrix material. It should also be carefully noted that, in any approach based on an effective macroscopic behavior, the finite element

mesh resolves the macroscopic fields only and does not resolve the microstructure explicitly.

An alternative approach is the use of mesh adaption to explicitly resolve multiple length scales. While methods of error estimation and mesh adaption for linear problems are presently well understood (e. g., [134]), our focus here is on strongly nonlinear, possibly dynamic, problems for which the theory is comparatively less developed [105, 31, 70, 13]. Applications involving unconstrained flows of material are amenable to a fully lagrangian finite element simulation provided that the inevitable deformation-induced distortion is eliminated by recourse to continuous remeshing. The versatility of this computational paradigm has been amply demonstrated in a variety of areas of application, including machining [91] and ballistic penetration [19, 20]. As remarked earlier, many of these solutions develop fine structure due to shock formation, microstructural development, material instabilities and other phenomena.

In the second part of this thesis and also in [113] a lagrangian finite element formulation of Newtonian fluid flows is presented with the aim of extending this computational paradigm to fluids problems. The principal advantage of the presented approach lies in the treatment of boundary conditions at material surfaces such as free boundaries, fluid/fluid or fluid/solid interfaces. In contrast to eulerian approaches, boundary conditions are enforced at material surfaces *ab initio* and therefore require no special attention. *Consistent tangents* are obtained for lagrangian implicit analysis of a Newtonian fluid flow which may exhibit compressibility effects. The accuracy of the approach is assessed by comparison of the solution for a sloshing problem with existing numerical results and its versatility demonstrated through a simulation of wave breaking. The finite element mesh is maintained undistorted throughout the computation by recourse to frequent and adaptive remeshing. An h-adaption strategy based on empirical refinement indicators is adopted to estimate the optimal mesh density. Whereas the adopted mesh adaption strategy effectively results in refinement (coarsening) in rapidly (slowly) varying regions of the flow, a theoretical rationale is lacking nor does the method provide any guarantee of resulting in convergent

approximations to the continuum equations.

The aim of this thesis is to develop a a general framework for mesh adaption under the challenging conditions just described. We begin by showing that the solutions of the incremental boundary value problem for a wide class of materials, including nonlinear elastic materials, compressible Newtonian fluids, and viscoplastic solids, obey a minimum principle, provided that the constitutive updates are formulated appropriately. This minimum principle can be taken as a basis for asymptotic error estimation. In particular, we chose to monitor the error of a lower-order projection of the finite element solution. The optimal mesh size distribution then follows from *a posteriori* error indicators which are purely local, i. e., can be computed element-by-element. We demonstrate the robustness and versatility of the computational framework with the aid of convergence studies and selected examples of application.

A *sine qua non* condition for the successful accomplishment of the kind of analysis envisioned in this work is the possibility to mesh the deforming domains of analysis. In the first chapter of this thesis a method is presented for mesh generation in complex geometries and general—possibly non-manifold—topologies. Domains are described by their Boundary representation (*B-Rep*). Surfaces are meshed by recourse to an advancing front algorithm based on a sphere-packing construction. The generation of tetrahedral volume meshes starts with the insertion of nodes arranged as crystal lattice structures. The local lattice parameter is dictated by a prespecified nodal density function, and is attained by spatial decomposition. The insertion of the interior nodes is followed by local transformations and subdivision of the surface mesh such as are required to ensure the compatibility of the surface and interior triangulations. The final triangulation is obtained by a combination of an advancing-front Delaunay algorithm and local transformations. The overall time complexity of the mesher is $O(N \log N)$, where N is the number of elements in the final mesh. The mesh generator is robust, requires minimal user interaction and gives good quality meshes. The versatility of the approach, as well as the quality of the resulting meshes, is demonstrated with the aid of selected examples.

Chapter 2 Unstructured tetrahedral mesh generation

2.1 Introduction

The generation of unstructured meshes is playing an increasingly important role in computational mechanics. Whereas it has been asserted that the subject has attained a maturity in which the problem can be regarded as solved [93], theoretical guarantees of mesh existence and algorithm termination are in general lacking and analysis of existing heuristics remain to be done [26].

A method which has gained considerable success in tetrahedral mesh generation is the advancing front method [109, 83, 78, 61, 96]. In this technique, elements and nodes are generated simultaneously starting from the boundary proceeding to the interior. The boundary discretization is taken as the initial front and a set of heuristics is employed to decide where the new element will be created, to place a new node in the interior and to reconnect the front. The mesh generation process terminates when the front is empty. In order to ensure the validity of the resulting mesh, intersection tests between new and existing mesh entities must be performed. Farestam *et al.* [39] present conditions which ensure that in the two-dimensional case the algorithm terminates and results in a valid mesh. No such theoretical guarantees exist in three dimensions. Therefore, a problem which is often encountered [61, 96]—and our own experience confirms—in the application of the method in three dimensions is the formation of non-tetrahedrizable pockets. In the references cited above attempts to prevent or resolve (cf. [81]) these situations are described.

Another widely used approach to tetrahedral mesh generation is based on the concept of the Delaunay triangulation. This consists in enforcing the condition that the spheres circumscribing the tetrahedra in the mesh be empty of vertices other than

those defining the sphere [34]. Algorithms for the efficient construction of this type of triangulation for the *convex hull* of a set of points are well established [16, 136, 15]. Of utmost concern when meshing three-dimensional volumes by the Delaunay method is the appearance of tetrahedra with vanishingly small volume, also referred to as *slivers* [24]. The sliver problem attests to the lack of optimality properties of the angles of the tetrahedra belonging to a three-dimensional Delaunay triangulation. Optimality properties of the Delaunay triangulation in three and higher dimensions have recently been presented by Rajan [116]. In contrast to the two-dimensional case, these properties do not guarantee the good quality of the triangulations. The constrained problem of constructing a triangulation a subset of which, e. g., the boundary mesh, is prespecified and which otherwise respects the Delaunay condition, has been successfully solved in two dimensions [27]. An additional obstacle inherent to the construction of tetrahedral meshes is that the related problem in three dimensions does not have a solution, i. e., it is not always possible to obtain a tetrahedral mesh of a set of points in which prespecified triangles are enforced to be present in the triangulation [6, 52]. Considerable effort has been devoted to the development of techniques which *recover* the boundary [125, 46, 137, 140, 138]). These techniques can be computationally intensive and lack theoretical analysis. For smooth boundaries, Amenta *et al.* [1] have recently presented conditions on the node sampling density which guarantee that the surface triangulation be a subcomplex of the volume Delaunay mesh. Fleischmann *et al.* [42] provide a set of heuristics to ensure similar conditions.

Techniques of unstructured meshing based on node insertion by spatial decomposition, also known as *octree methods*, have been amply established and successfully used to mesh general three-dimensional domains [17, 111, 126, 127]. The most critical issues in these approaches concern the compatibility between the boundary of the domain and the octree and the compatibility between octants. The former compatibility requirement may restrict the complexity of the domains that can be successfully meshed or may lead to meshes with poor quality at the boundary.

In this work, a new method for the generation of tetrahedral meshes for complex geometries and general topologies is presented. A thorough topological model based

on the *Boundary representation of solids* is developed to describe deforming domains the topology of which may evolve as a result of physical phenomena such as fragmentation, wetting and erosion. The geometry of surfaces is represented by implicit functions for the initial definition and by piecewise polynomial interpolation subordinate to a finite element discretization of the domain in the case of remeshing. A hierarchical approach to mesh generation is adopted in which *edges* are meshed first, then *faces* and finally *sub-bodies*. An underlying element-size distribution function is assumed to be defined throughout the domain to be meshed. In the case of remeshing this distribution derives from suitably defined error estimates (see Chapter 4 and [114]). The meshing of surfaces is based on the advancing front method with nodal insertion by hard-sphere packing in physical space. The hard-sphere packing construction provides a natural means of inserting nodes on a surface in accordance with a prescribed mesh density. Nodes interior to the volumes are inserted in FCC crystal lattice arrangements by recourse to octree spatial subdivision. This node insertion strategy is aimed at producing Delaunay meshes without degeneracies and of the greatest possible regularity. Prior to triangulation of the volumes, the surface mesh is preprocessed through local transformations and subdivision in order to guarantee that the surface mesh be a subset of the volume Delaunay mesh and therefore its existence. For smooth boundaries, theoretical guarantees of the closure of the surface modification algorithm follow from the recent work of Amenta [1]. A Delaunay triangulation of the interior and boundary nodes which respects the—*a priori* modified—surface mesh is obtained *via* an advancing front algorithm. The final triangulation is obtained by mesh improvements based on local transformations. The overall time complexity of the mesher is $O(N \log N)$, where N is the number of elements in the final mesh. The mesh generator is robust, requires minimal user interaction and gives good quality meshes. The versatility of the approach, as well as the quality of the resulting meshes, is demonstrated with the aid of selected examples.

2.2 Model description—Boundary representation of solids

Whereas a complete topological representation of solids is often not necessary for the application of particular meshing algorithms, here we envision a computational framework in which topology plays an active role, e. g., as a consequence of such physical phenomena as fragmentation, necking, erosion, wetting, seizure, and others. Under these circumstances, meshing and mechanics are tightly coupled. The main function of mesh generation is to provide the mechanics module with a good-quality computational mesh. Conversely, the ensuing mechanical analysis determines the mesh density, e. g., by recourse to error estimation. Additionally, physical phenomena such as fragmentation and wetting may cause the topology of the model to evolve. The ability to remesh continuously then requires the adoption of suitable topological structures and the implementation of operations enabling the tracking of evolving topologies [104].

We assume that the domains of interest are topological polyhedra homeomorphic to simplicial complexes which define triangulations of the domains [55]. The outcome of the meshing operation is a particular instance of triangulation. This assumption allows *bodies* to be described by their boundary. This representational paradigm, known as *Boundary representation of solids* (*B-Rep*) in the solid modeling literature [55, 88, 120], is specially convenient as a basis for mesh generation procedures of the advancing front variety. It also facilitates other finite element operations in which boundaries need to be explicitly accounted for, e. g., contact, wetting, erosion, surface tension, fragmentation, and others. A *B-Rep* representation consists of the following:

A topological description of the connectivity, incidence and adjacency of the *vertices*, *edges*, and *faces* which constitute the boundary of the *bodies*, together with a consistent orientation leading to an unambiguous determination of the interior and exterior of the domain of analysis.

A geometrical description of the surface of the domain. This geometrical descrip-

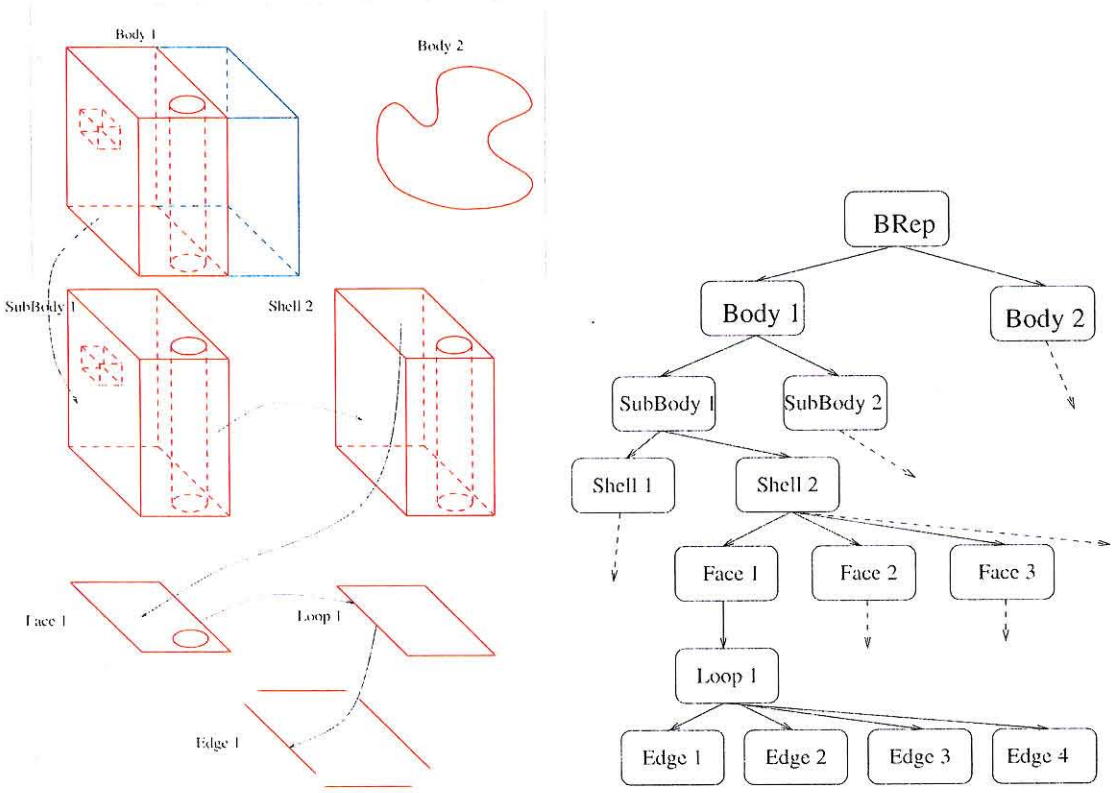

(a) *B-Rep* schematic

(b) corresponding *B-Rep* tree

Figure 2.1: Boundary representation of rolids

tion may be interpreted as an embedding of the model in euclidean space.

The topological hierarchy implicit in a *B-Rep* may be regarded as a graph [88], Fig. 2.1. We adopt a linked representation of this graph using C pointers [130]). The root of the graph points to the *bodies*, which are defined as the connected components of the domain of analysis. Each *body* may consist of several *sub-bodies*, e. g., containing different materials. The boundaries of the *sub-bodies* represent features which must be respected by the mesher. Each *sub-body* therefore constitutes a fundamental unit of volumetric meshing, *i.e.*, is meshed separately.

The boundaries of the *sub-bodies* are 2-manifolds without boundary. The connected components of the boundary of a *sub-body* are termed *shells*. It follows, therefore, that each *shell* defines a connected 2-manifold without boundary. A complete

classification of such objects is known from differential topology [48]. The equivalence classes are represented by spheres with a finite number of handles. The number of handles appended to the sphere is known as the genus of the surface. The *shells* can be oriented consistently so as to unambiguously define an interior and an exterior for each *sub-body*.

The *shells* may be partitioned into *faces* defining smooth regions whose boundary must be preserved by the mesher. The boundaries of the *faces* may represent salient geometric features of the *shell* such as ridges or sharp edges. The trivial case of a *shell* which consists of one single *face* is also possible. The *faces* represent the fundamental unit of surface meshing, *i.e.*, they are meshed separately. The *faces* are also regarded as oriented surfaces, but this orientation is assigned arbitrarily. One *face* may be shared by two *shells*, e. g., at a material boundary, in which case it appears in each *shell* with opposite orientations. The fact that a *face* may be shared by more that one *shell* renders the *B-Rep* graph a general directed acyclic graph.

Each *face* may be regarded as a 2-manifold with boundary. The boundary of a *face* is itself a 1-manifold without boundary. The connected components of the boundary of a *face* are known as *loops*. It is known from differential topology [48] that a *loop* is topological equivalent to the unit circle.

The *loops* may be partitioned into *edges* whose end *vertices* must be preserved by the mesher. The trivial case of a *loop* which consists of one single *edge* is also possible. The edges constitute the fundamental unit of line meshing. The *edges* are regarded as oriented segments, but this orientation is assigned arbitrarily. One *edge* may be shared by two *loops*, in which case it appears in each *loop* with opposite orientations. This completes the topological definition of the *B-Rep*.

The geometry of curves and surfaces can be described either analytically or by interpolation. Most engineering geometrical models are presently generated with the aid of CAD/CAM packages. Often these packages produce analytical representations of surfaces in terms of tensor-product polynomials or rational functions such as splines, B-splines, nonuniform rational B-splines (NURBS surfaces), Bezier functions, Coon's patches, and a variety of other means. Our primary focus, however, concerns

the adaptive lagrangian simulation of solids undergoing large deformations, possibly resulting in unconstrained flows. During a remeshing step, the old mesh provides a natural geometrical description of the domain of analysis. In the context of finite element analysis, this description takes the form of piecewise polynomial interpolation of the geometry of the solid.

We have therefore found it convenient to adopt two complementary representations of the geometry of *faces*. In the first approach, the surfaces are represented by an implicit function $f(\mathbf{x}) = 0$. The surface gradient $\nabla f(\mathbf{x})$ defining the surface normal and orientation is assumed to be continuous in the domain of the *face*. It is important to note that this approach is free of the restriction encountered when representing surfaces with tensor product functions, namely, that the surface be bounded by *loops* consisting of four *edges*. We adopt this representation for the initial definition of *faces* whose geometry may be defined simply in analytical form.

An alternative approach consists of representing the *faces* by piecewise polynomial interpolation subordinate to a finite element discretization of the domain. This representation is used by default during remeshing, in which case the discretization of the domain is furnished by the old mesh. In all cases, the geometry of the *edges* is always described by piecewise quadratic interpolation.

From the standpoint of mechanics, the local mesh size derives from suitably defined error estimates (see Chapter 4 and [114]) or other remeshing indicators. However, the local mesh size required to resolve the solution may be too coarse to adequately represent the geometry of the domain of analysis. An example is provided by a solid undergoing a rigid body motion, in which case the size of the mesh is not restricted by accuracy requirements. Under these conditions, one appealing possibility concerns the use of subdivision surfaces [145, 38] to *enhance* the surface mesh prior to remeshing.

2.3 Meshing of topological entities

Our approach to meshing general domains consists of a traversal of the *B-Rep* tree in a bottom-up fashion, with the *edges* being meshed first, then the *faces* and finally

the *sub-bodies*. This hierarchical approach aims at ensuring the validity of the final mesh [127, 10]. An underlying element-size distribution function $h(\mathbf{x})$ is assumed to be defined throughout the domain Ω to be meshed. For convenience, we define the size h of a tetrahedron as $\sqrt{2/3}$ the radius of its circumscribed sphere. By this convention, for a regular tetrahedron h equals one-half of its side. In calculations, the element-size distribution function $h(\mathbf{x})$ is available in either of the following forms:

- Analytically.
- By a weighted average of an element-size function defined over the boundary, e. g.:

$$h(\mathbf{x}) = \frac{\int_{\partial\Omega} \frac{h(\mathbf{y})d\Gamma(\mathbf{y})}{|\mathbf{x}-\mathbf{y}|^{\alpha}}}{\int_{\partial\Omega} \frac{d\Gamma(\mathbf{y})}{|\mathbf{x}-\mathbf{y}|^{\alpha}}} \tag{2.1}$$

  where $\partial\Omega$ is the boundary of Ω, and $\mathbf{x} \in \Omega$. Evidently, the averaging rule should be such that $h(\mathbf{x}) \to h(\mathbf{y})$ as $\mathbf{x} \to \mathbf{y} \in \partial\Omega$ from the interior of the domain. In eq. (2.1) this is ensured by setting $\alpha = 2d$, where d is the dimension of the boundary. The function $h(\mathbf{y})$ over $\partial\Omega$ may be defined *face* by *face* and should result in an appropriate resolution of the geometry of the *face*, e. g., along regions of high curvature.
- By interpolation on a previous mesh. This is the default representation of $h(\mathbf{x})$ in the case of remeshing.

Algorithms for the consistent meshing of *edges*, *faces* and *sub-bodies* are described in subsequent sections. Specialized data structures help to reduce the time complexity of the requisite insertion, deletion, and search operations. In particular, we choose to keep unordered lists as linked lists, ordered lists as priority queues [130] and spatially dependent entity lists as point-region octrees [124]. These data structures have previously been proven very efficient in finite element mesh generation applications [80].

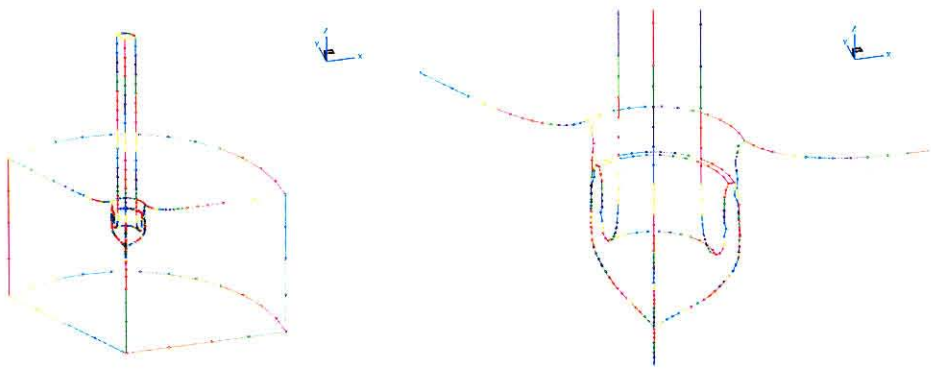

(a) full view (b) zoom view

Figure 2.2: Example of the meshing of *edges*

2.3.1 Meshing of *edges*

Triangulations of one-dimensional objects such as *edges* may conveniently be understood as discrete solutions of the eikonal equation:

$$\left|\frac{dw}{ds}\right| = \frac{1}{h} \tag{2.2}$$

where $s \in [0, L]$ is the arc length and we set $w(0) = 0$. The mesh nodes s_i, $i = 0, \ldots, N$ then follow from the difference equation:

$$w(s_{j+1}) - w(s_j) = \frac{w(L)}{N} \tag{2.3}$$

Thus, the nodes coincide with the level points of w at regular intervals of $1/N$. A simple implementation of the method consists of sequentially packing spheres centered on the *edge* of a radius equal to the target element size h. This operation is akin to adding a bead to a necklace. Evidently, the last sphere in the sequence may not fit exactly at the end of the *edge*. This lack of closure may be corrected by scaling back the distribution of nodes. An example of *edge* meshing, corresponding to a three-dimensional model of ballistic penetration, is shown Fig. 2.2.

2.3.2 Meshing of surfaces

Once all the *edges* in the model have been meshed, we may turn to the triangulation of the objects at the next level in the *B-Rep*, namely, the *faces*. Issues pertaining to the generation of unstructured meshes on surfaces defined analytically have been addressed by Lo [76], Lohner *et al.* [83], Moller *et al.* [96], Lo [79], Lau *et al.* [68] and Rypl *et al.* [123]. Our general approach to surface meshing is based on the advancing front method with nodal insertion by hard-sphere packing. In contrast to common practice, we do not carry out the meshing in parametric space but in physical space directly. The hard-sphere packing construction provides a natural means of inserting nodes on a surface in accordance with a prescribed mesh density.

The surface meshing algorithm proceeds as follows:

0. *Initialization of the front.* The topological attributes of the *face* under consideration are retrieved from the *B-Rep*, including a list of oriented *edges* defining the *face loops*. The initial front is the list of consecutive segments gathered from the discretization of the *edges* (cf Section 2.3.1). The segments are consistently oriented counterclockwise relative to the orientation of the *face*, see Fig. 2.3. The common strategy of sorting the front list in ascending order of the segment sizes to preclude large elements crossing regions of small mesh size [110, 83] has recently been questioned [96]. To this end, we have found that this technique, which may be computationally expensive, is not necessary as long as the gradient of the mesh density distribution is limited. The front is therefore configured as a linked list, which is specially well-suited for the operations of random insertion and deletion of front segments. For each node i of position $\mathbf{x}_i$ on the front, the corresponding local mesh size h_i is obtained from the background mesh-density function. In the case of remeshing, the local mesh size is interpolated from the old mesh. Additionally, in preparation for nodal insertion we consider the spheres S_i of radii h_i and centers $\mathbf{x}_i$. It should be noted that these spheres may not be tightly packed in general, and small gaps and interpenetrations may be present. The first element in the front is

arbitrarily declared as the *active* segment. All the nodes in the initial front, as well as the new nodes added subsequently, are inserted in a point-region octree. This octree is used to search for nodes in the vicinity of the active segment.

1. *Definition of a tentative new node.* The beginning and final nodes of the active segment are labeled 1 and 2, respectively. The corresponding spheres S_1 and S_2 have centers and radii $\{\mathbf{x}_1; h_1\}$ and $\{\mathbf{x}_2; h_2\}$, respectively. A tentative new node is inserted on the *face* at the center $\mathbf{x}$ of a trial sphere S of radius $h(\mathbf{x})$ packed against S_1 and S_2. Thus, the trial sphere S is determined by the following three conditions:

   - $f(\mathbf{x}) = 0$, *i.e.*, the center of the sphere lies on the surface.
   - $h = h(\mathbf{x})$, where $h(\mathbf{x})$ is the mesh-size function, *i.e.*, the radius of the sphere matches the local mesh size.
   - $|\mathbf{x} - \mathbf{x}_1| = h + h_1$ and $|\mathbf{x} - \mathbf{x}_2| = h + h_2$, *i.e.*, the new sphere is packed against–or in contact with–the end spheres of the active segment.

   This system of four nonlinear equations may be reduced to an equivalent system of two equations as follows. Begin by introducing the local orthonormal frame $\{\mathbf{g}_1, \mathbf{g}_2, \mathbf{g}_3\}$ centered at $\mathbf{x}_1$, where $\mathbf{g}_1$ is the unit vector in the direction of the active segment and $\mathbf{g}_3$ is the unit normal to the *face* at the midpoint of the active segment, Fig. 2.3. The point $\mathbf{x}$ must lie on the circle:

$$\mathbf{x}(h, \theta) = \mathbf{x}_1 + \alpha_1(h)\mathbf{g}_1 + \beta(h)\big(\cos\theta\, \mathbf{g}_2 + \sin\theta\, \mathbf{g}_3\big) \tag{2.4}$$

   where

$$\alpha_1(h) = \frac{d^2 + (h_1 - h_2)(2h + h_1 + h_2)}{2d} \tag{2.5}$$

$$\beta(h) = \frac{1}{2d}\sqrt{[d^2 - (h_1 - h_2)^2]\,[(2h + h_1 + h_2)^2 - d^2)]} \tag{2.6}$$

   and $d = |\mathbf{x}_2 - \mathbf{x}_1|$. The unknown parameters h and θ then follow from the

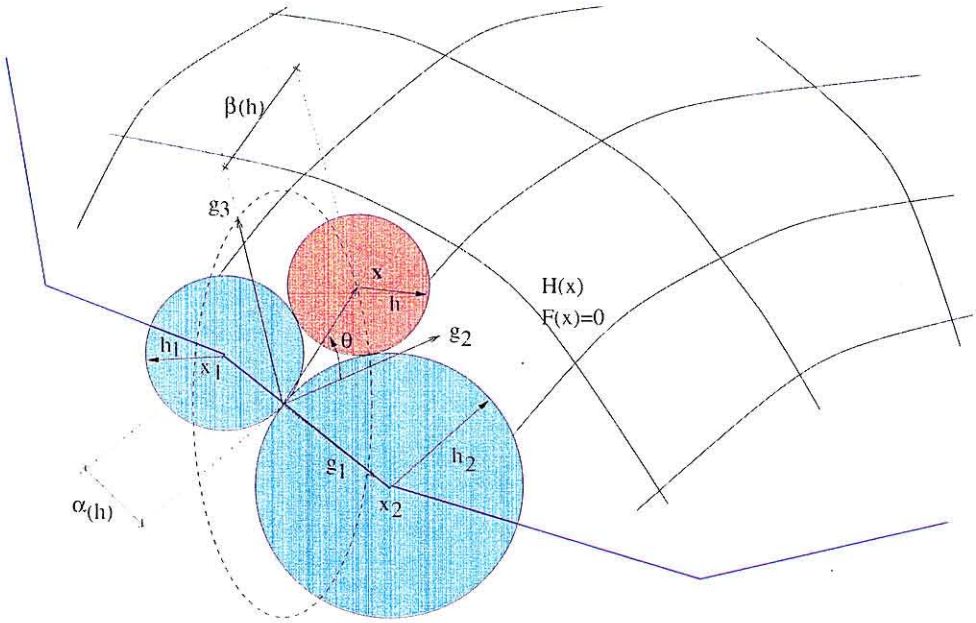

Figure 2.3: Hard-sphere packing on a surface

system of equations:

$$F\big(\mathbf{x}(h,\theta)\big) = 0 \tag{2.7}$$

$$h\big(\mathbf{x}(h,\theta)\big) = h \tag{2.8}$$

Equations (2.7) and (2.8) are readily solved for h and θ by recourse to a Newton-Raphson iteration provided that the functions $f(\mathbf{x})$ and $h(\mathbf{x})$ are sufficiently smooth. Alternatively, an approximate packing may be obtained by estimating h as $(2h1h2)/(h_1 + h_2)$, thus reducing the problem to the solution of the single equation

$$F\big(\mathbf{x}(h,\theta)\big) = 0 \tag{2.9}$$

in the single unknown θ.

2. *Collision detection.* The *face* octree is searched for possible collisions of the trial sphere S with existing spheres in the front. In order to speed-up this operation,

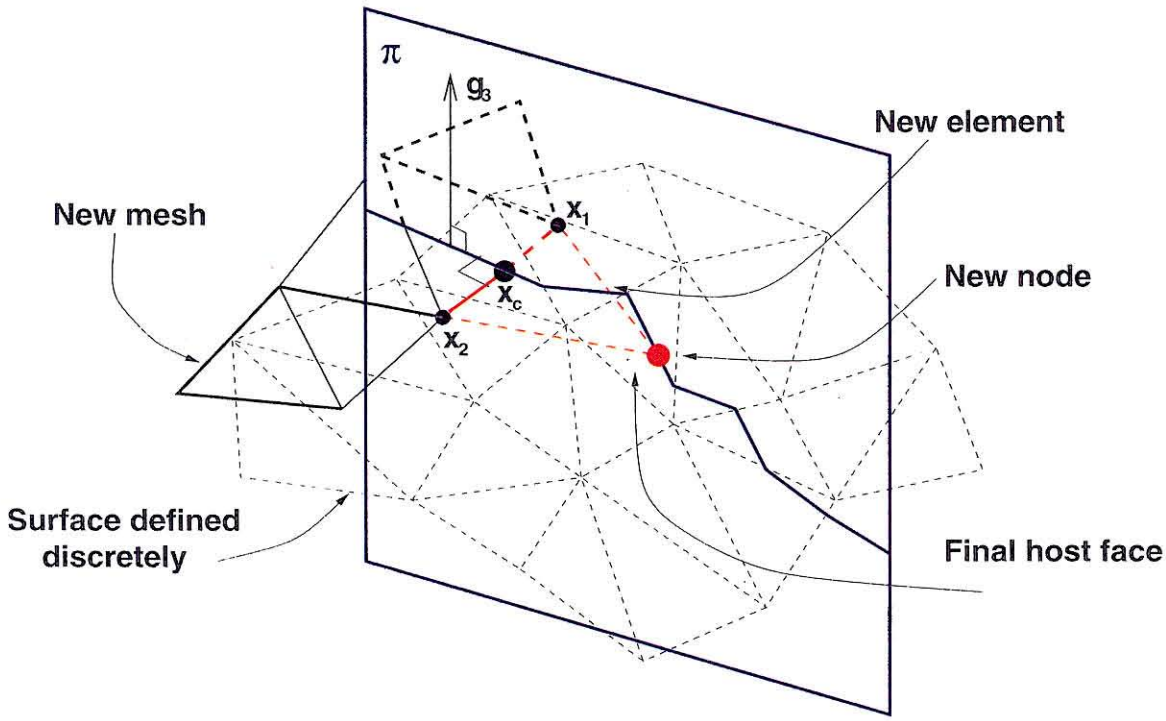

Figure 2.4: Node insertion on a discretized surface

the octree search is further restricted to the nodes lying in the half-space determined by the active segment and the vector $\mathbf{g}_2$. If a collision does indeed occur, the octree query retrieves the sphere resulting in the most interpenetration, which is redesignated as the new trial sphere S.

3. *Enforcement of the empty circumsphere condition.* The aim of this step is to make the final selection of the trial point $\mathbf{x}_3$ involved in the formation of the new triangle. In making this selection we seek to enforce the empty circumsphere condition, namely the condition that the minimal sphere containing the points $\{\mathbf{x}_1, \mathbf{x}_2, \mathbf{x}_3\}$ does not contain any other points on the *face*. The satisfaction of the empty circumsphere criterion is required in order to ensure that the surface mesh is the restriction of a tetrahedral Delaunay triangulation of the volume (cf Section 2.3.3). A list of candidate nodes is compiled by searching in the *face* octree for all the nodes lying inside the circumsphere of the triangle defined by the front segment and the center $\mathbf{x}$ of the trial sphere S

determined in Step 2. If the resulting list is empty, the trial node $\mathbf{x}_3$ is set to $\mathbf{x}$. Otherwise, the node(s) satisfying the empty circumsphere criterion is (are) found among the list of candidates by the following divide-and-conquer procedure:

1: **for all** nodes in the list of candidates **do**
2: consider the sphere circumscribing the triangle formed by the front segment and the node under consideration and discard from the list all the nodes which lie outside.
3: **end for**

4. *Check for intersections.* Before accepting the trial node $\mathbf{x}_3$, a check is made to verify that the newly formed triangle does not intersect any existing edges or triangles. We choose to test for edge-triangle intersections of new edges with existing triangles adjacent to the front segments; and for intersections of the new triangle with existing edge segments in the front. As pointed out by Lohner [82] and Rypl *et al.* [123], the intersection detection algorithm may fail in surfaces of high curvature. A more robust algorithm is obtained if the intersection test is done in a plane approximately tangent to the *face* where the new triangle is to be inserted. If the trial triangle fails the intersection test, it is discarded along with $\mathbf{x}_3$, and Step 3 is repeated.

5. *Front update.* The new triangle $\{\mathbf{x}_1\mathbf{x}_2\mathbf{x}_3\}$ is inserted in the list of *face* elements and the front linked list is updated as follows. The base segment is always deleted from the front linked list. If $\mathbf{x}_3$ is initially connected to the base segment node $\mathbf{x}_1$ ($\mathbf{x}_2$), then a new segment joining $\mathbf{x}_3$ ($\mathbf{x}_1$) and $\mathbf{x}_2$ ($\mathbf{x}_3$) is created and inserted in the linked list of front segments. In this case the segment connecting nodes $\mathbf{x}_3$ ($\mathbf{x}_2$) and $\mathbf{x}_1$ ($\mathbf{x}_3$) is deleted from the front linked list, decreasing the number of segments in the front by one. Also in this case, node $\mathbf{x}_1$ ($\mathbf{x}_2$) ceases to be in the front. If $\mathbf{x}_3$ is otherwise on the front or is a new node, then two new segments are created joining nodes $\mathbf{x}_1$-$\mathbf{x}_3$ and $\mathbf{x}_3$-$\mathbf{x}_2$, increasing the number of segments in the front by one.

6. *Check for completion.* If the list of front segments is empty the algorithm exits. Otherwise the next segment in the front is processed by repeating the steps starting at Step 1.

The case of surface remeshing merits special consideration. Issues of algorithm robustness and efficiency pertaining to the application of the advancing front technique to the meshing of a discretized surface have been addressed by Lohner [82]. Specifically, the nodal insertion operation differs from the continuous case in that the geometry of the *face* is defined by interpolation based on the previous mesh, which provides a piecewise polynomial description of the surface geometry, Fig. 2.4. In calculations, we preferentially use ten-node quadratic tetrahedra in order to avoid volumetric locking and to facilitate the simulation of fracture and fragmentation [103, 104]. The restriction of these volume elements to the surface defines a six-node quadratic element. In order to simplify the insertion of a new node, we begin by faceting the surface elements in the old mesh into assemblies of four piecewise linear elements. New nodes lying on the faceted surface are subsequently projected onto the quadratic mesh.

The implementation of the sphere-packing operation also differs from the construction used in the analytical case, which tends to break down on discretized surfaces owing to the discontinuous variation of the normal. The following approximate packing construction is adopted instead. The new node is assumed to lie on the plane Π defined by (cf Fig. 2.4)

$$(\mathbf{x} - \mathbf{x}_c) \cdot \mathbf{g}_1 = 0, \tag{2.10}$$

where

$$\mathbf{x}_c = \frac{h_1 \mathbf{x}_1 + h_2 \mathbf{x}_2}{h_1 + h_2} \tag{2.11}$$

The intersection of this plane with the old faceted mesh defines a piecewise linear curve on which the sought node $\mathbf{x}$ is forced to lie. The precise sequence of opera-

tions leading to the determination of the triangle containing $\mathbf{x}$ and the corresponding natural coordinates is listed in Algorithm 1, (see also Fig. 2.4).

Algorithm 1 Node insertion in surface remeshing

Require: Define an approximate surface normal $\mathbf{g}_3$ as the normal to the triangle in the new mesh behind the active segment, if available, or as the normal to the triangle in the old mesh hosting point $\mathbf{x}_c$. Compute the advancing direction $\mathbf{g}_2 = \mathbf{g}_3 \times \mathbf{g}_1$. Determine the initial host triangle from a proximity search from the point

$$\mathbf{x}' = \mathbf{x}_c + \frac{\sqrt{3}h_1 h_2}{h_1 + h_2} \frac{\mathbf{g}_2}{|\mathbf{g}_2|}, \tag{2.12}$$

using the octree of triangles of the old mesh.

1: **while** final host triangle not found **do**
2: Visit the current host triangle.
3: Determine the segment intersections $\mathbf{x}_a$ and $\mathbf{x}_b$ of the current host triangle boundary and the plane Π.
4: Let ξ be such that

$$|\mathbf{x}(\xi) - \mathbf{x}_c| = \sqrt{3}h \tag{2.13}$$

where

$$\mathbf{x}(\xi) = (1 - \xi)\mathbf{x}_a + \xi\mathbf{x}_b \tag{2.14}$$

5: **if** $0 \leq \xi \leq 1$ **then**
6: Final host found: set new node to: $\mathbf{x} = \mathbf{x}(\xi)$
7: **else if** $\xi < 0$ $(\xi > 1)$ **then**
8: set the new host triangle equal to the triangle incident to the current host on the side containing $\mathbf{x}_a$ $(\mathbf{x}_b)$.
9: **end if**
10: **end while**

Some of the operations involved in the node-insertion algorithm may be facilitated by the use of special data structures. These structures include a point-region octree of element centroids in the old mesh; and a triangle adjacency list, such as a winged-edge table, which enables a quick access to adjacent elements.

The performance of the algorithm just described is illustrated in Fig. 2.5, which shows an intermediate stage in the meshing of a half sphere. In this case, the model consists of a single *face* bounded by a single *loop*. The geometry of the sphere is

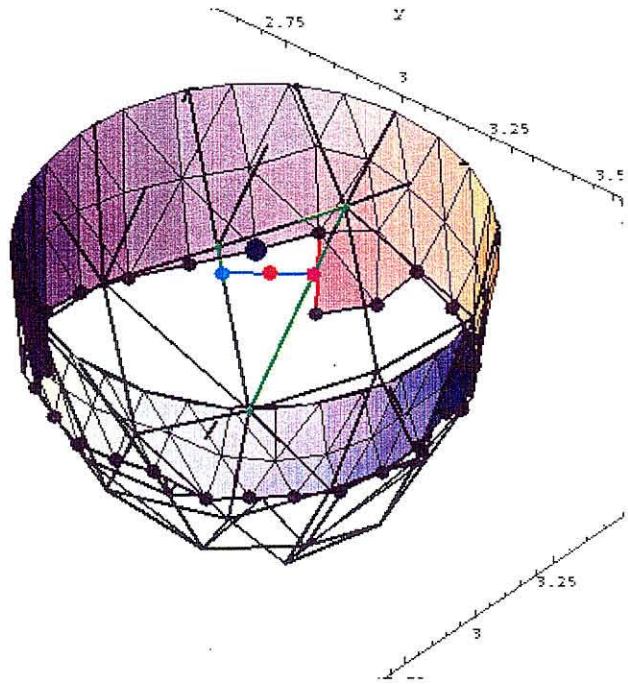

Figure 2.5: Surface remeshing. Snapshot of the advancing front algorithm in progress

described by means of a coarse initial mesh. The new target mesh size is set to one half the initial mesh size. Meshing begins with the remeshing of the *edge*, which is subsequently taken as the initial front. In the particular snapshot depicted in Fig. 2.5, the active segment is shown in red, and the intersection of the Π-plane with the first host triangle is shown in blue. The first trial node is shown as a red dot on the blue line. In this case, the corresponding sphere collides with an existing one centered on the node marked by a large blue dot, which is therefore used to form a new triangle. The complete initial and final meshes are shown in Fig. 2.6.

An example of the coupling between remeshing and mechanical analysis is shown in Fig. 2.7, which concerns a snapshot of a simulation of flag waving in a constant wind. The new mesh has a target size equal to one half the initial mesh size. The ability of the mesher to treat arbitrary discretized surfaces is noteworthy.

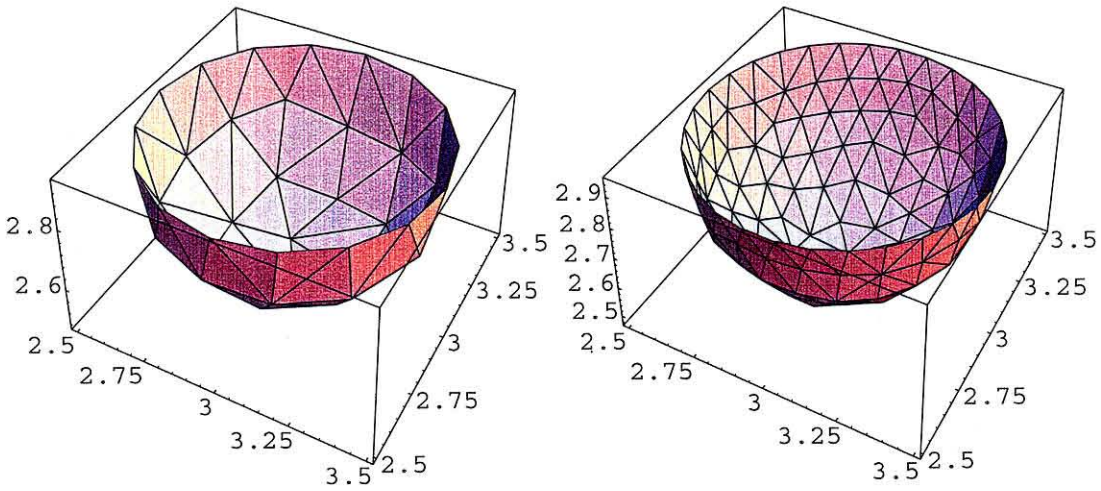

(a) Discretized *face* (b) remeshed *face*

Figure 2.6: Remeshing of *faces*: example corresponding to a sphere sector

2.3.3 Meshing of volumes

The last step in our hierarchical construction of the analysis problem mesh consists in filling the volume of *sub-bodies* with tetrahedra respecting the mesh density distribution. We adopt a hybrid method which consists in node insertion followed by triangulation.

Node insertion by spatial decomposition in crystal lattice arrangements

Techniques based on node insertion by spatial decomposition, also known as *octree methods* have been amply established and successfully used to mesh general three-dimensional domains [17, 111, 126, 127]. In this approach the geometric model is spatially decomposed according to mesh control parameters resulting in an octree whose terminal or leaf octants contain a subset of the domain to be meshed. The octant geometry is much simpler and thus easier to mesh than the original geometry. The octant corners and points defined by the intersection of the boundary of the object with the octant boundaries define the mesh nodes.

The octree approach is not in itself an element generation technique. Elements are generated in the terminal octants by a variety of methods including: the use

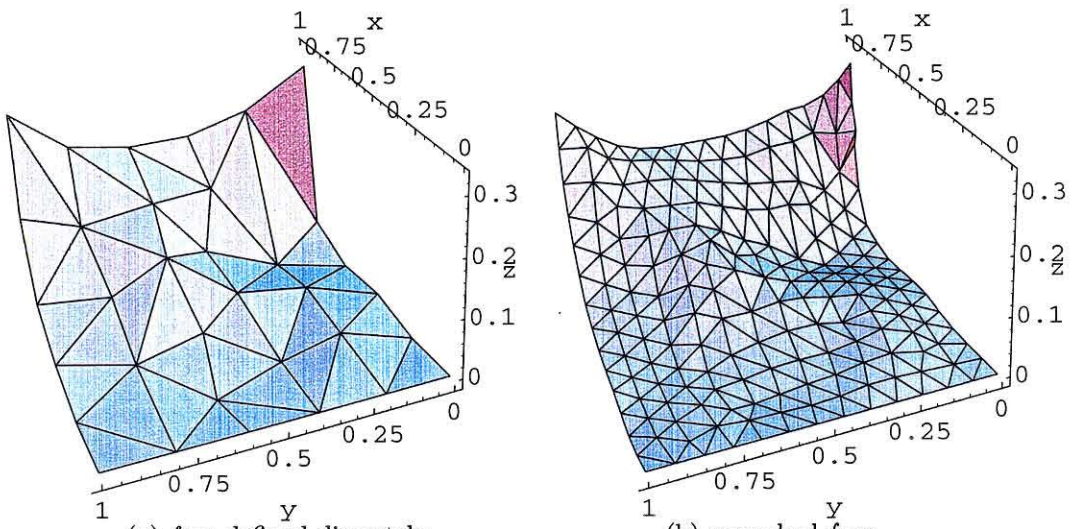

(a) *face* defined discretely (b) remeshed *face*

Figure 2.7: Remeshing of *faces*: snapshot of a simulation of flag waving in a constant wind

of templates and template matching between octants followed by element removal schemes [142]; and Delaunay triangulation on an octant-by-octant basis followed by a procedure to ensure octant compatibility [126]. The most critical issues in these approaches concern the compatibility between the boundary of the domain and the octree and the compatibility between octants. The former compatibility requirement may restrict the complexity of the domains that can be successfully meshed or may lead to meshes with poor quality at the boundary.

In contrast to standard octree methods, we do not place the nodes at leaf octant corners in the spatial-decomposition octree. Instead, we seek to devise a node insertion strategy which, in the case of a uniform target mesh size, results in a periodic lattice supporting tetrahedra of the greatest possible regularity. To this end, we have found it useful to resort to basic concepts of crystallography, e. g., [60, 49]. Thus, the requirement of periodicity implies that the nodes must necessarily be arranged as one of the 14 Bravais lattices. For instance, in two dimensions the hexagonal Bravais lattice leads to a uniform Delaunay mesh consisting of equilateral triangles. In three dimensions, we have analyzed the Delaunay meshes which derive from face-centered

cubic (FCC) and body-centered cubic (BCC) lattices.

In order to compare the qualities of various lattice structures, we define the aspect ratio of a tetrahedron as

$$\sigma = \frac{R}{3\rho} \tag{2.15}$$

where R and ρ are the radii of the circumscribed and inscribed spheres, respectively. The quality of a tetrahedron is in inverse proportion to its aspect ratio. Other alternative tetrahedron quality measures are discussed elsewhere [107, 75]. A plausible measure of the quality of a triangulation $\mathcal{T}$ may be derived from the consideration of the standard interpolation error estimate (e. g., [29]):

$$\|u_h - u\|_m \leq \sum_{K \in \mathcal{T}} C \sigma_K^m h_K^\alpha |u|_k \tag{2.16}$$

where u is a function in the Sobolev space $H^k(\Omega)$, $k \geq 1$ is the order of polynomial interpolation, $\alpha = k + 1 - m > 0$ is the order of convergence, u_h is the interpolant corresponding to the triangulation $\mathcal{T}$, K denotes a tetrahedron in the triangulation, $\|\cdot\|_m$ is the norm in $H^m(\Omega)$ and $|\cdot|$ is the semi-norm of order k in $H^k(\Omega)$. If we now consider a mesh much finer than the characteristic length of variation of u, then $|u|_k$ may be treated as constant in the right-hand side of (2.16), which reduces to

$$I = \sum_{K \in \mathcal{T}} \sigma_K^m h_K^\alpha \tag{2.17}$$

where we have omitted inconsequential constants. This indicator may therefore be taken as a measure of the quality of the triangulation. The mathematical problem of optimal node insertion can now be stated as that of finding the periodic arrangement of nodes which minimizes (2.17).

In the FCC structure, Fig. 2.8, the nodes are located at the corners of the unit cell and at the centers of the cell faces. The nodes in the $\{111\}$ planes define the densest possible arrangement of spheres. The size of the unit cell is a. Fig. 2.9 shows the Delaunay triangulation of the FCC unit cell, which consists of a total of 24 elements,

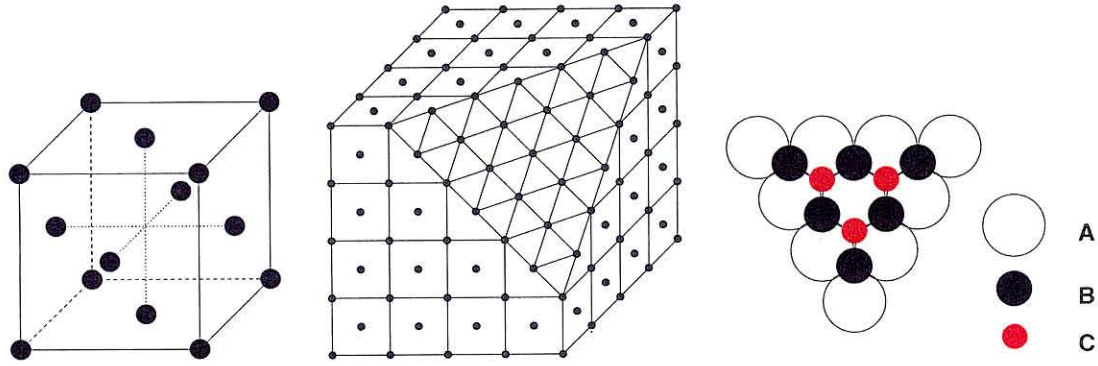

(a) unit cell

(b) arrangement of atoms in a {111} close-packed plane

(c) stacking sequence of {111} planes

Figure 2.8: FCC structure

8 of which are equilateral, with an aspect ratio $\sigma = 1$ and a size $h = 0.356a$, and the remaining 16 have a low aspect ratio $\sigma = (2+\sqrt{3})/3 \sim 1.24$ and a size $h = 0.408a$. All the elements in the Delaunay mesh of the FCC unit cell have the same volume $V = a^3/24$. Fig. 2.9 also highlights the two types of elements encountered in the Delaunay triangulation of the FCC unit cell. Representative elements of each type are defined by the nodal sets:

$$\text{equilateral tetrahedron } (\sigma = 1): \quad \{\{0,0,0\},\{\frac{1}{2},\frac{1}{2},0\},\{0,\frac{1}{2},\frac{1}{2}\},\{\frac{1}{2},\frac{1}{2},0\}\}a$$

$$\text{irregular tetrahedron } (\sigma = 1.24): \quad \{\{0,0,0\},\{1,0,0\},\{\frac{1}{2},\frac{1}{2},0\},\{\frac{1}{2},0,\frac{1}{2}\}\}a$$

An *a posteriori* application of the empty circumsphere test to the Delaunay mesh of the FCC unit cell just described readily uncovers degeneracies, Fig. 2.10 (cf Section 2.3.3 for a discussion of Delaunay degeneracies). These degeneracies stem from the fact that the six face-center nodes in the FCC unit cell lie on a common sphere of radius $a/2$. This coincidence gives rise to an indeterminacy in the Delaunay mesh: the octahedron defined by the six face-center nodes can variously be meshed by inserting an edge between either of the three pairs of opposite nodes and four tetrahedra. Evi-

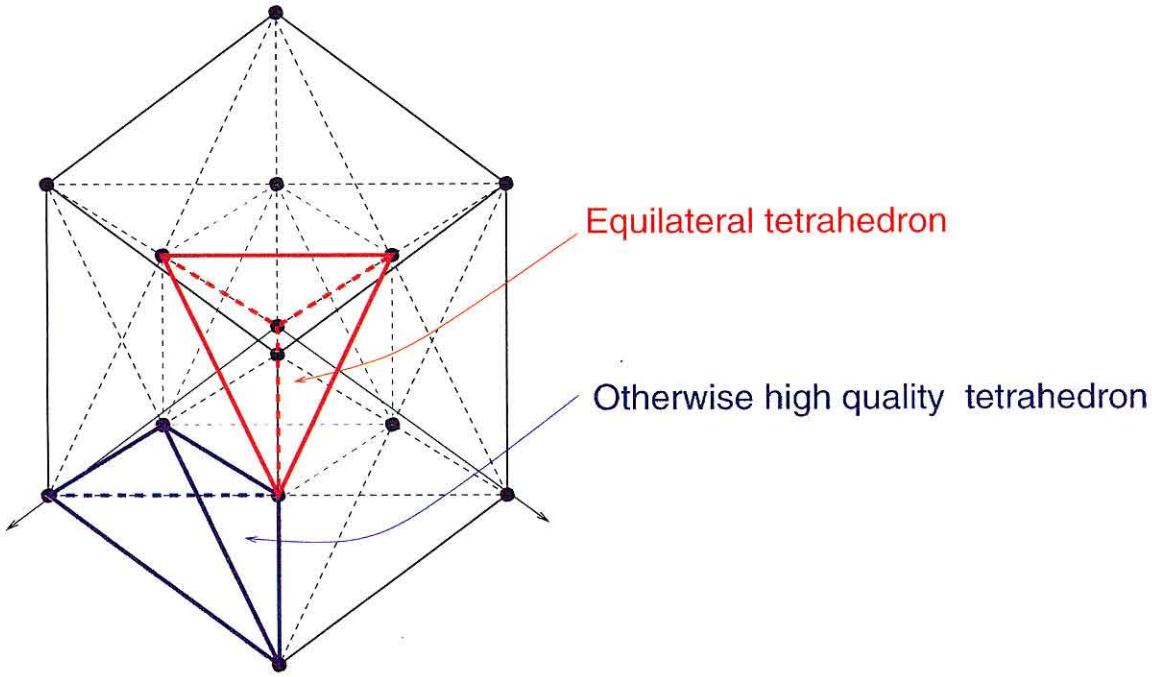

Figure 2.9: Delaunay mesh of an FCC unit cell. Representative tetrahedra of each type ($\sigma = 1$ and $\sigma = \frac{2+\sqrt{3}}{3} \sim 1.24$) are highlighted.

dently, the circumsphere corresponding to any of these tetrahedra coincides with the common sphere containing the six face-center nodes. Therefore, the circumspheres are not empty but contain two extra nodes on their boundaries. Even more worrisome is the fact that a naive Delaunay triangulation may result in slivers defined by groups of four nodes lying on the three $\{100\}$ planes. However, as shown in Section 2.3.3, the introduction of slivers during triangulation in cases of this nature can be readily avoided.

By periodicity, the preceding observations carry over *ipso facto* to uniform meshes. An example of an FCC lattice covering a cube is shown in Fig. 2.11. A careful Delaunay triangulation of this lattice exhibits no slivers and contains two classes of tetrahedra, such as already identified in the triangulation of one FCC cell, of aspect ratios $\sigma = 1$ and $\sigma = (2 + \sqrt{3})/3 \sim 1.24$.

A competing Bravais lattice as regards nodal insertion is the body-centered (BCC) lattice. In this case, the Delaunay mesh of the unit cell consists of 12 identical

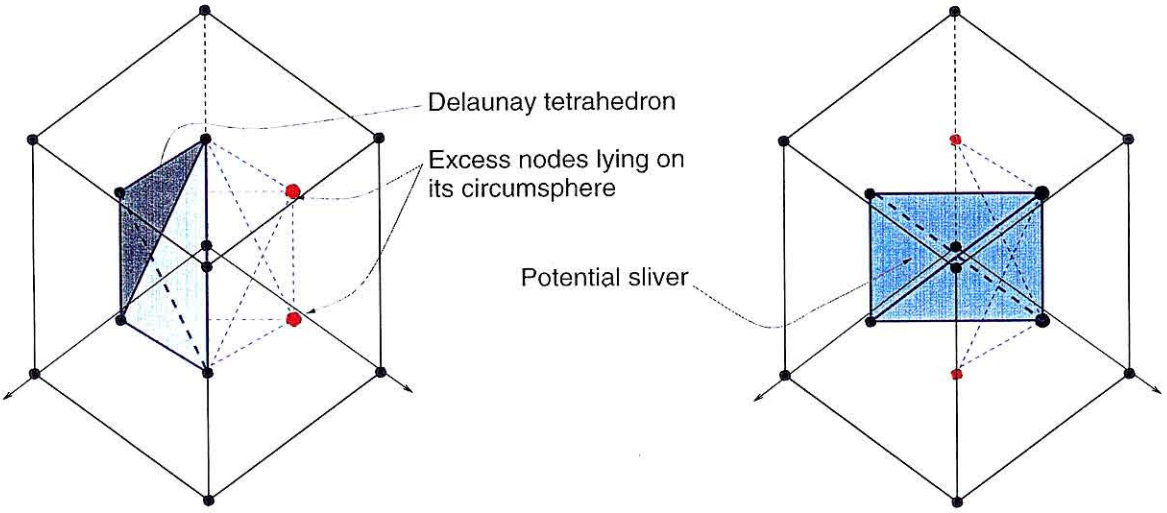

Figure 2.10: Degeneracies present in a Delaunay triangulation of the FCC unit cell: The six face centered nodes lie in the same circumsphere leading to mesh non-uniqueness and potential slivers

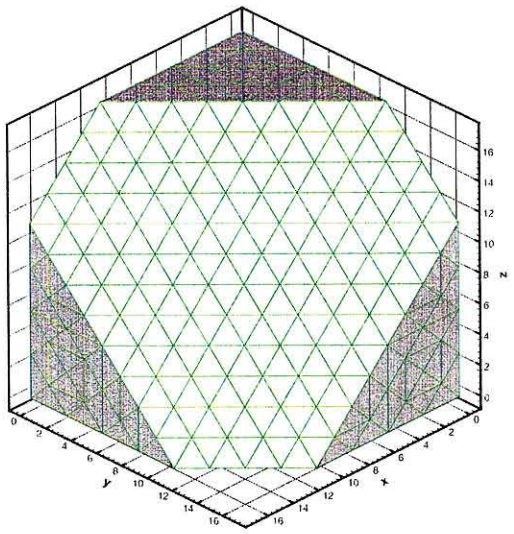

Figure 2.11: Delaunay mesh of an FCC grain

tetrahedra of aspect ratio $\sigma = 1.56$ and size $h = 0.614a$. The volume of the tetrahedra is $V = a^3/12$. As in the FCC structure, the Delaunay triangulation of the unit cell is not unique and care must be exercised to avoid the introduction of slivers. For instance, the four *vertices* of a face and the body-center node are cospherical, giving rise to a situation of non-uniqueness.

A comparison of the quality of triangulations of FCC and BCC lattices may now be based on the measure (2.17). For definiteness, we choose $m = 1$, whereupon the $\|\cdot\|_m$ becomes equivalent to the energy norm of linear elasticity, and $k = 2$, corresponding to quadratic interpolation. With this choice of parameters, $I_{FCC}/I_{BCC} = 0.615$. We conclude, therefore, that the FCC lattice is superior to the BCC lattice as regards optimal node insertion. It seems plausible that the FCC lattice is also superior to the remaining 12 Bravais lattice, although we have not verified this conjecture explicitly.

In order to extend the preceding nodal insertion method to the case of a nonuniform mesh, such as described by a general mesh-size distribution function $h(\mathbf{x})$, and arbitrary domains Ω, we combine the concepts of Bravais lattice and spatial subdivision. The resulting node insertion algorithm is summarized in Algorithm 2. The objective is to insert nodes in a locally-FCC arrangement with a lattice size $a(\mathbf{x})$ commensurate with $h(\mathbf{x})$. This is accomplished by recursive spatial decomposition of the domain into an octree whose leaves are of size $h(\mathbf{x})$, in the spirit of octree methods [17, 111, 126, 127]. However, in our approach the leaves of the octree are not regarded as units of meshing but are solely used for the purpose of node insertion. This is accomplished by designating each octree leave as an FCC cell and inserting nodes accordingly. Conflicts with neighboring cells are avoided by placing all new nodes into a nodal octree, which automatically precludes the duplication of nodes. Once all the nodes have been inserted, the mesh is obtained by the global advancing-front Delaunay triangulation algorithm presented in Section 2.3.3.

The binary character of octree domain decomposition necessarily forces a discretization of $h(\mathbf{x})$ in powers of two. As is common practice [127] we restrict the generational difference between octree leaves to one. A direct consequence of these restrictions is that the number of types of tetrahedra which may arise in the transition

regions between two mesh sizes, which necessarily differ by a factor of two, is finite, and is therefore amenable to a complete classification. In particular, just as in the triangulation of the FCC cells, the transition regions can be triangulated without the introduction of slivers. These attributes of the method ensure the good quality of the volume mesh.

Algorithm 2 Node insertion

Require: A triangulation of all the *faces* in the *B-Rep*; a mesh-size distribution function $h(\mathbf{x})$.

1: **for all** *sub-bodies* in the domain **do**
2: Retrieve the topological information for the *sub-body* under consideration from the *B-Rep*. Form a triangulation of the *shells* by merging the triangulations of the corresponding *faces* taken with consistent orientations.
3: Define the octree root as the bounding box of the *sub-body* boundary oriented along its principal axes of inertia.
4: Recursively subdivide the octree until the size of the leaf octants is commensurate with $h(\mathbf{x})$.
5: Identify the leaf octants as FCC cells.
6: **for all** the 14 nodes in each FCC cell **do**
7: insert the node in the nodal octree.
8: **end for**
9: **end for**

Remark

- The insertion of the nodes in the nodal octree automatically precludes the duplication of nodes with the same spatial location such as may arise from insertion into adjacent FCC cells.

Modification of the surface triangulation

Next we turn to the problem of constructing a tetrahedral mesh of a given *sub-body*. The objective is to construct a joint Delaunay triangulation, i. e., one in which all tetrahedra have empty circumspheres, of the interior and surface nodes and whose restriction to the surface is the given surface triangulation. An inherent difficulty in carrying out this program is that, for arbitrary surface triangulations and interior nodal sets, a triangulation does not exist in general [6, 52, 33]. A well-

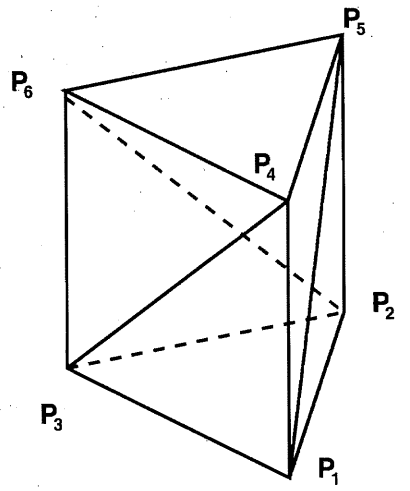

Figure 2.12: Example of a Schönhardt (impossible to mesh) polyhedron

known example of a polyhedron whose Delaunay triangulation is incompatible with the surface triangulation is shown in Fig. 2.12.

Considerable effort has been devoted to the development of techniques which *recover* the boundary as an *a posteriori* step to the Delaunay triangulation [125, 46, 137, 140, 138]). These techniques can be computationally intensive and lack theoretical analysis. For smooth boundaries, Amenta *et al.* [1] have recently presented conditions on the node sampling density which guarantee that the surface triangulation be a subcomplex of the volume Delaunay mesh. Fleischmann *et al.* [42] provide a set of heuristics to ensure similar conditions.

A sufficient condition for a surface triangulation to be the restriction of a volume Delaunay mesh containing a given interior point set is that all triangles in the surface triangulation have empty minimal circumspheres. The sufficiency of this condition is established by the following simple argument. Consider the empty minimal circumsphere of a surface triangle. Expand the sphere by displacing its center towards the interior of the domain in the direction normal to the surface triangle. Eventually, the expanding sphere comes in contact with a fourth node which, in conjunction with the surface triangle, defines a Delaunay tetrahedron. This operation may be repeated until all surface triangles are covered by Delaunay tetrahedra, which shows that the

surface triangulation is a subcomplex of the volume Delaunay mesh.

In view of this result, and as a preliminary step to the meshing of the interior, we modify the surface triangulation by a combination of diagonal swaps and subdivision in an attempt to satisfy the empty minimal circumsphere condition. When the minimal circumsphere of a surface triangle contains a surface node, an attempt is first made to correct the situation by swapping diagonals with adjacent triangles. If this fails, then the offending triangle is bisected along its longest side if the adjacent triangle on this side does not have a longer edge. These operations are repeated until the minimal circumspheres of all surface triangles are empty, or until a minimum mesh size is reached, in which case the algorithm fails. If the algorithm does close, then all interior nodes contained in the minimal circumsphere of a surface triangles are eliminated. This operation has the beneficial effect of removing interior nodes which are too close to the boundary and which, if kept, might result in tetrahedra of poor quality.

For smooth boundaries, theoretical guarantees of the closure of the surface modification algorithm just described follow from the recent work of Amenta [1]. The local feature size of a point of the surface is defined as the radius of the largest sphere tangent to the surface at a point which is contained in the body. A surface triangulation is guaranteed to satisfy the empty minimal circumsphere condition provided that the local mesh size is everywhere a small fraction of the local feature size. No similar sufficient condition for nonsmooth surfaces is known to us.

Triangulation by advancing front Delaunay

A Delaunay triangulation of a set of points in three-dimensional space is a tetrahedral decomposition of the *convex hull* of the point set, where the *vertices* of the tetrahedra belong to the point set, such that the interior of the circumspheres of the tetrahedra does not contain points from the set [34]. The triangulation is unique if situations in which more than four points lie on the surface of the circumsphere of any tetrahedra do not occur. Of utmost concern when meshing three-dimensional volumes by the Delaunay method is the appearance of tetrahedra with vanishingly small volume,

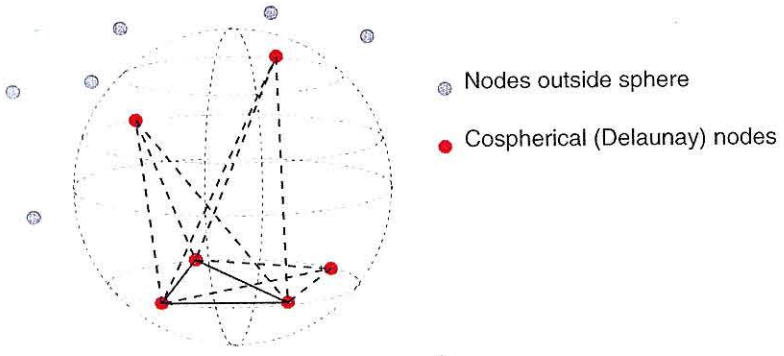

Figure 2.13: Degenerate Delaunay situation including the possible formation of a sliver

also referred to as *slivers* [24]. This situation arises when a cospherical set of points, causing a breakdown of uniqueness in the Delaunay triangulation, contains four or more points which are coplanar, Fig. 2.13. The sliver problem attests to the lack of optimality properties of the angles of the tetrahedra belonging to a three-dimensional Delaunay triangulation. Optimality properties of the Delaunay triangulation in three and higher dimensions have recently been presented by Rajan [116]. In contrast to the two-dimensional case, these properties do not guarantee the good quality of the triangulations. Indeed, it has been shown by Joe [63] that in many cases tetrahedral Delaunay meshes can be improved by *local transformations*, which violate the Delaunay empty circumsphere criterion.

Here we describe an advancing front algorithm for the construction of Delaunay tetrahedral meshes from their restriction to the surface, which is presumed known *a priori* (cf Section 2.3.3). The approach is related to work by Mavriplis [92] in two dimensions and motivated by algorithms proposed by Tanemura [131] and Merriam [94]. A 3D implementation of the Merriam-Tanemura algorithm has been presented recently by Fleischmann *et al.* [42]. The algorithm constructs the Delaunay triangulation incrementally, *i.e.*, one tetrahedron at a time, starting from the boundary triangulation in a bottom-up fashion. Thus the surface triangulation exists in the final triangulation *ab initio* and the problem of surface recovery is thereby obviated. The method searches for nodes which form Delaunay tetrahedra with the active tri-

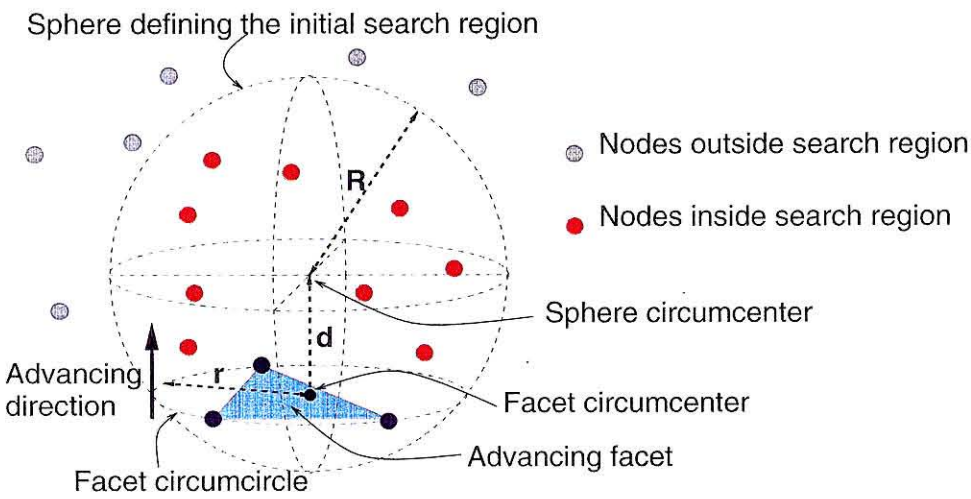

Figure 2.14: Advancing front Delaunay: Initial search region

angle. Among these tetrahedra, a selection is made based on quality criteria and on the avoidance of subsequent slivers, leading to the introduction of a new tetrahedron in the mesh. The algorithmic steps followed to advance the front are otherwise very similar to those in the conventional advancing front method [83, 109, 77, 61, 96, 25]. However, the heuristics attendant to the introduction of nodes and elements are considerably reduced.

The volume meshing algorithm may be summarized as follows:

0. *Initialization of the front.* The initial front is identified with the surface triangulation. The triangles in the initial front are configured as a linked list. Owing to the uniqueness of the volume triangulation the order in which the front triangles are processed is inconsequential, which is in contrast to the conventional advancing front algorithms. The surface triangulation is assumed to conform to the prescribed mesh-size distribution, and to satisfy the empty minimal circumsphere condition discussed in Section 2.3.3. The first triangle in the front is designated as the active triangle. The nodes in the initial front, as well as the interior point set, are inserted in a point-region octree. This octree is used to search for nodes in the vicinity of the active triangle.

1. *Search region.* The purpose of this step is to construct a bounding box which

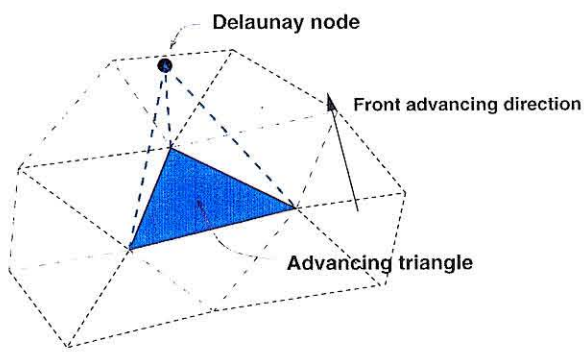

(a) Three edges and three triangles added

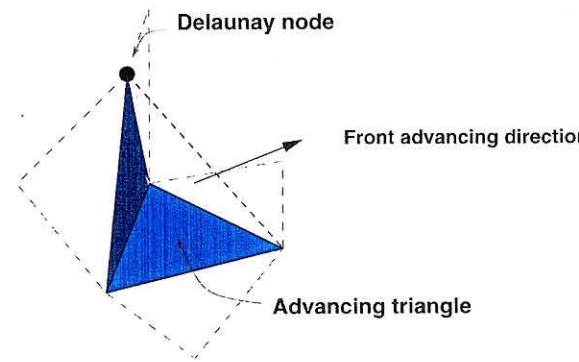

(b) One edge and two triangles added

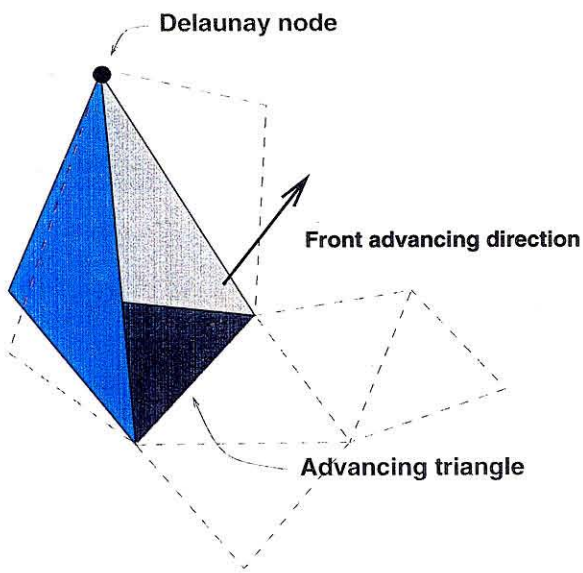

(c) One triangle added

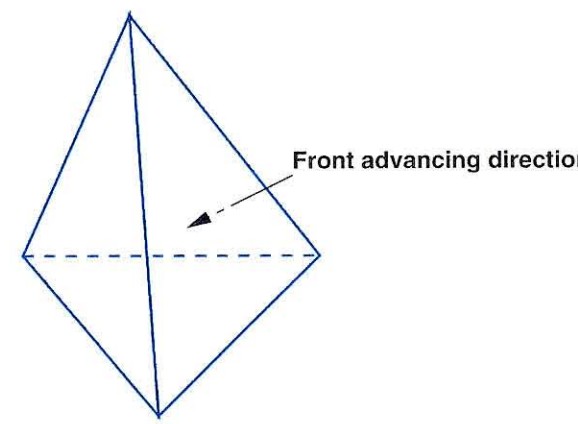

(d) Front closes

Figure 2.15: Front reconnection in 3D

is sure to contain the node or nodes which form Delaunay tetrahedra with the active triangle. We begin by recalling the fact that the projection of the center of the circumsphere of a tetrahedron on the planes of its faces coincides with the centers of the circumspheres of the faces [116]. Consider the sphere which contains the circumcircle of the active triangle and whose center is at distance $d = 2r$ from the active triangle, where r is the radius of the circumcircle, Fig. 2.14. The radius of this sphere is $R = \sqrt{5}r$. The cube parallel to the cartesian axes which strictly contains this sphere defines the initial search region. When the interior point set is generated by the node insertion algorithm described in Section 2.3.3, the bounding box just defined is sure to contain at least one Delaunay node.

2. *Tetrahedron insertion.* In this step, the node which defines the new Delaunay tetrahedron is determined. A list of candidate nodes is formed by searching in the *sub-body* octree for all the nodes lying inside the search box defined in Step 1. Nodes which are already part of the mesh and are not on the front, and nodes in the half-space behind the active triangle are not included in the list. The nodes satisfying the empty circumsphere criterion are readily found among the list of candidate nodes by the following divide-and-conquer strategy:

   1: **for all** nodes in the list of candidate nodes **do**
   2: Discard all candidate nodes not contained in the circumsphere defined by the active triangle and the current candidate node.
   3: **end for**

   If several cospherical candidate nodes are detected, all the corresponding tetrahedra are evaluated and the one of best quality which does not lead to subsequent slivers is selected.

3. *Front update.* The new tetrahedron is inserted in the list of tetrahedra for the *sub-body*. The front is then updated as follows, Fig. 2.15. The active triangle is always deleted from the front linked list. If the Delaunay node found in Step 2 is:

- not a *vertex* of the triangles adjacent to the active triangle, three triangles are added to the front, Fig. 2.15(a).
- a *vertex* of one triangle adjacent to the active triangle, two triangles are added to the front and the adjacent triangle is deleted from the front, Fig. 2.15(b).
- a *vertex* of two triangles adjacent to the active triangle, *i.e.*, the two adjacent triangles share an edge, one triangle is added to the front and the adjacent triangles are deleted, Fig. 2.15(c).
- a *vertex* of the three triangles adjacent to the active triangle, the three adjacent triangles are deleted and the front closes locally. Fig. 2.15(d).

4. *Termination.* The algorithm terminates when the front is empty. Otherwise the next triangle in the front is retrieved and control returns to Step 1.

Remark

- By virtue of the empty minimal circumsphere satisfied by the surface triangulation and the properties of the Delaunay triangulation, the need for costly intersection tests of new and existing mesh entities, such as required in traditional advancing front methods, is eliminated.

Mesh improvement

In two dimensions, Delaunay meshes possess the min-max property for angles and are therefore optimal in this regard. In three dimensions, however, no such property is known to be possessed by Delaunay or other triangulations, and the quality of the tetrahedral meshes may sometimes be improved by the application of operations such as edge-face or octahedral swapping [63, 64, 43] and smoothing [127]. These common mesh improvement operations have been implemented in the mesh generator and their versatility confirmed in the examples of application.

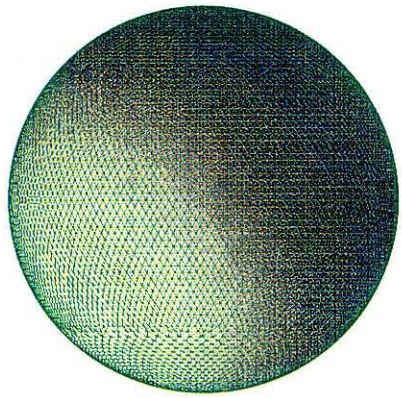

Figure 2.16: Mesh of sphere with uniform mesh size (358024 elements)

2.4 Examples of application

In this section a suite of examples is collected to assess the performance of the mesh generator developed in the foregoing. The emphasis is in establishing the robustness of the method and the quality of the resulting meshes.

The first example corresponds to meshes of a sphere with different uniform sizes. The finest mesh, which contains 358024 elements, is shown in Fig. 2.16. In order to assess the quality of the resulting meshes, statistical measures of the quality of the tetrahedra have been computed. The following tetrahedron quality measure has been adopted:

$$\gamma = \frac{S_{rms}^3}{8.48528V} \tag{2.18}$$

where

$$S_{rms} = \sqrt{\frac{1}{6}\sum_{i=1}^{6} S_i^2} \tag{2.19}$$

is the root mean square of the lengths of the tetrahedron edges S_i, V is the volume of the tetrahedron and the factor 8.48528 normalizes the quality of a regular tetrahedron. This tetrahedron quality measure exhibits good sensitivity to all the

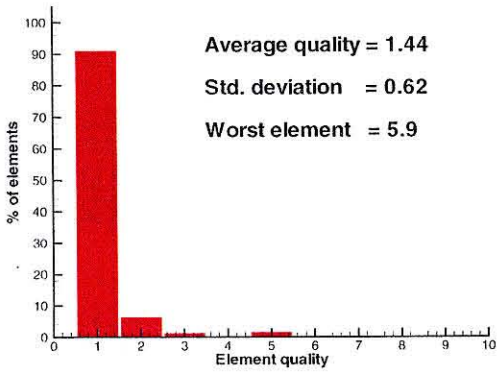

(a) before mesh improvement

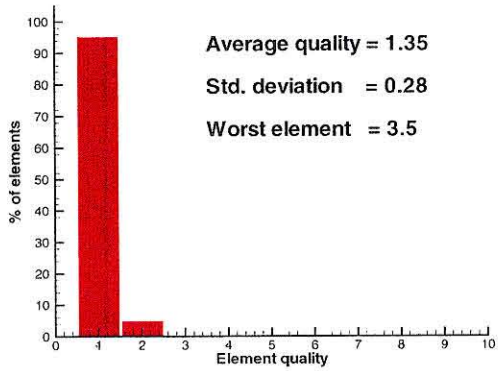

(b) after mesh improvement

Figure 2.17: Mesh quality statistics - 5200 elements

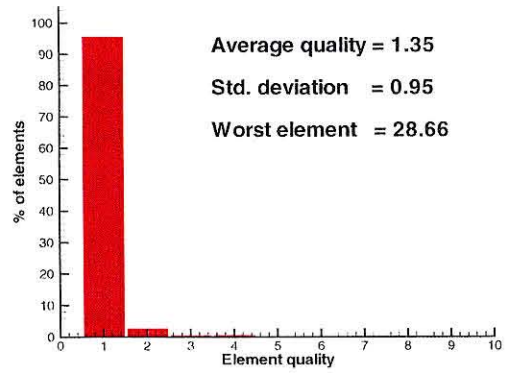

(a) before mesh improvement

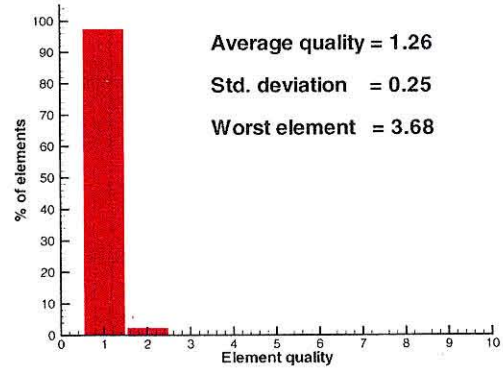

(b) after mesh improvement

Figure 2.18: Mesh quality statistics - 44784 elements

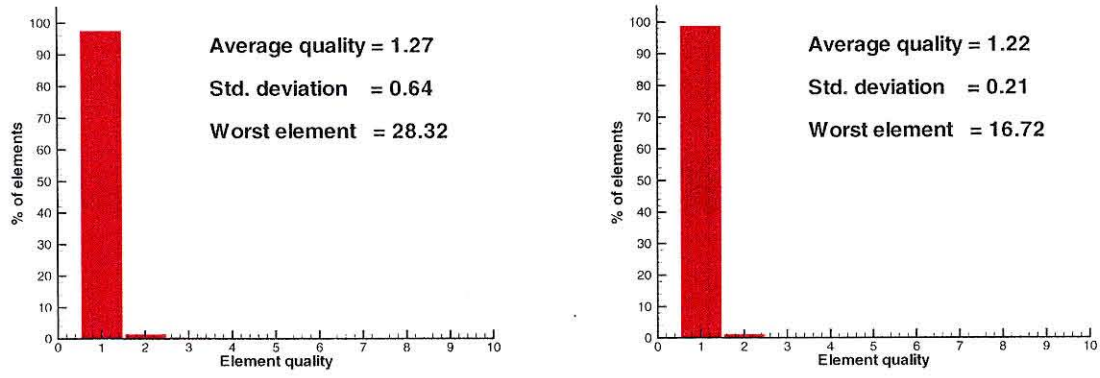

(a) before mesh improvement

(b) after mesh improvement

Figure 2.19: Mesh quality statistics - 358024 elements

different kinds of element distortion [107]. Figs. 2.17, 2.18 and 2.19 show frequency histograms, mean quality, standard deviation and worse element quality for three different meshes consisting of 5200, 44784 and 358024 elements respectively before and after the application of the mesh improvement techniques presented in Section 2.3.3. It can be observed from these figures that this operation effectively results in meshes of better quality.

The example in Fig. 2.20 corresponds to the mesh of a sphere with a strong gradient in the mesh density distribution. A cross section of the mesh is shown in this figure exhibiting six levels of refinement present in the mesh. The different regions of uniform mesh size (FCC grains) as well as the grain boundaries can be easily observed. Fig. 2.20 also depicts the performance of the surface mesher algorithm. It is evident from this figure that the resulting surface meshes are very smooth and that the surface nodes exhibit the optimal value of 6 for the coordination number despite the presence of strong gradients in the mesh density distribution.

Finally, Figs. 2.21, 2.22 and 2.23 illustrate the ability of the proposed method to produce meshes of shapes with practical interest. In the case of the oblique penetrator, Figs. 2.21, the input *B-Rep* is given analytically, whereas in the case of Figs. 2.22 and 2.23 the input *B-Rep* consists of a surface triangulation of the boundary. It can

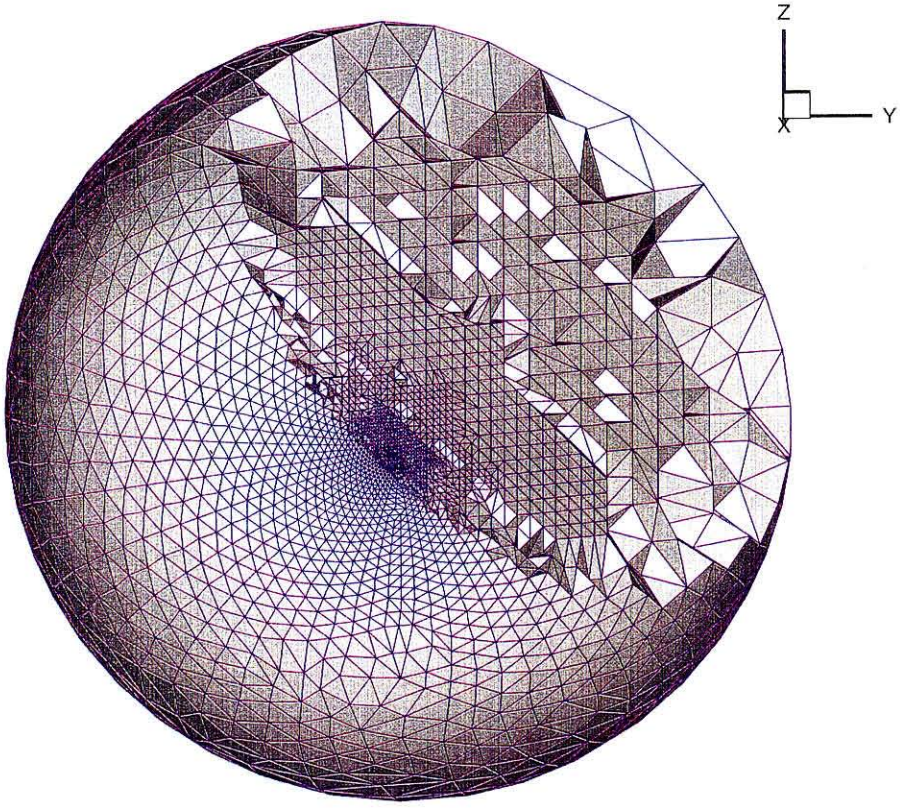

Figure 2.20: Mesh of a sphere (180704 elements)

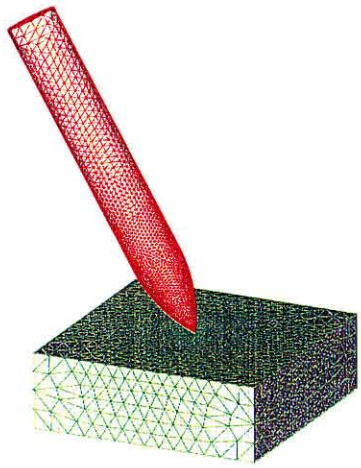

(a) general view of the mesh

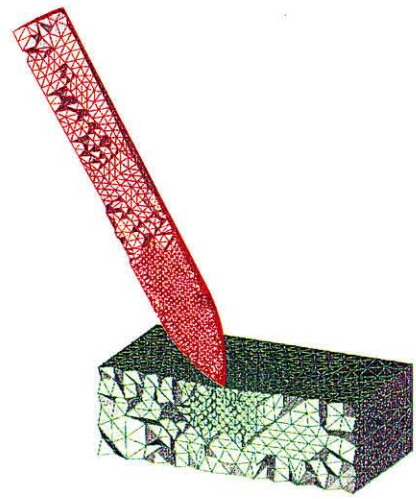

(b) cross section of the mesh

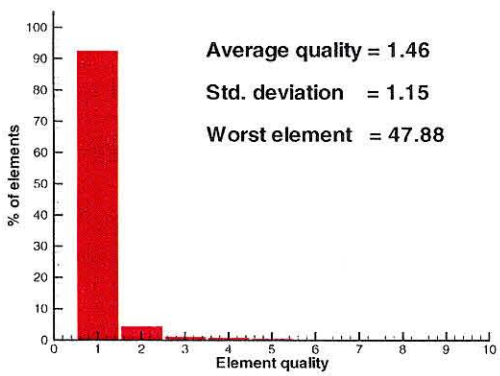

(c) mesh quality before mesh improvement

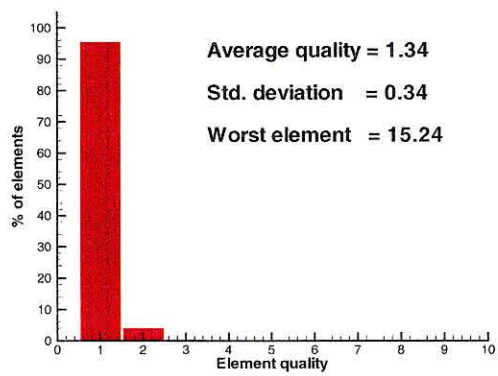

(d) mesh quality after mesh improvement

Figure 2.21: Model of an ogive-nose rod impacting a plate at an oblique angle (63768 elements)

be observed from Fig. 2.21 that in this case the application of the techniques presented in Section 2.3.3 also causes a considerable improvement in the mesh quality. The case corresponding to Fig. 2.22(c) illustrates the effect of the surface modification process near sharp corners. It can be observed from this figure that the algorithm attempts to satisfy the conditions stated in Section 2.3.3 by subdividing the facets in a self-similar manner near the sharp corner.

2.5 Summary and conclusions

We have developed a new automatic method for generation of unstructured tetrahedral meshes in complex geometries and general topologies. We mesh the surfaces by recourse to an advancing front algorithm based on a sphere-packing construction. The first step in the volume meshing consists in inserting nodes in the interior in FCC crystal lattice arrangements with the aid of an octree spatial subdivision. The surface mesh is modified prior to triangulation of the interior and boundary points in order to ensure compatibility of the surface and interior triangulations. The final triangulation is obtained by a combination of an advancing-front Delaunay algorithm and local transformations. The existence of the final mesh is guaranteed for smooth boundaries. We demonstrate the versatility of the approach, as well as the quality of the resulting meshes, with the aid of selected examples.

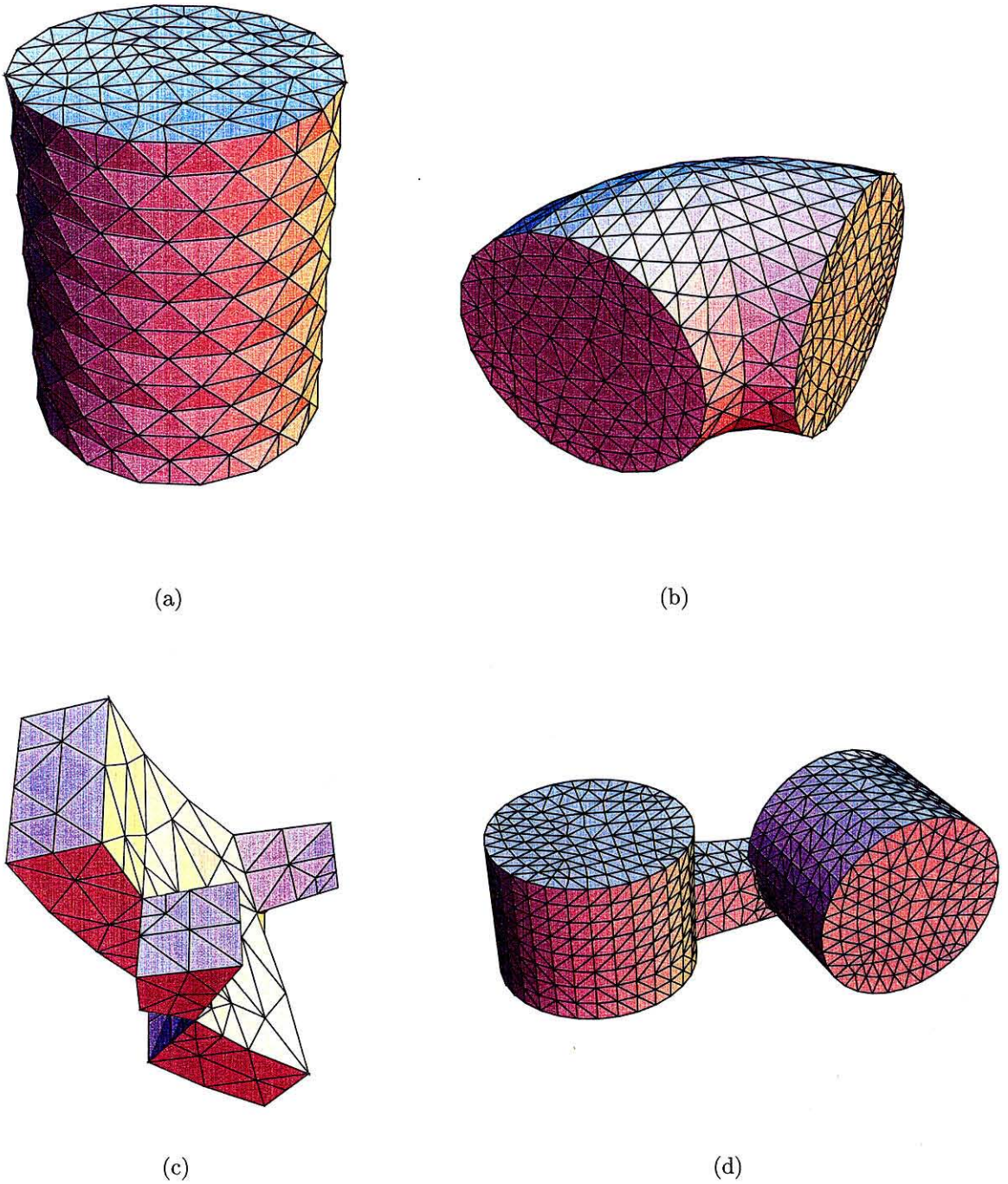

(a) (b)

(c) (d)

Figure 2.22: Meshes corresponding to shapes given by a surface triangulation

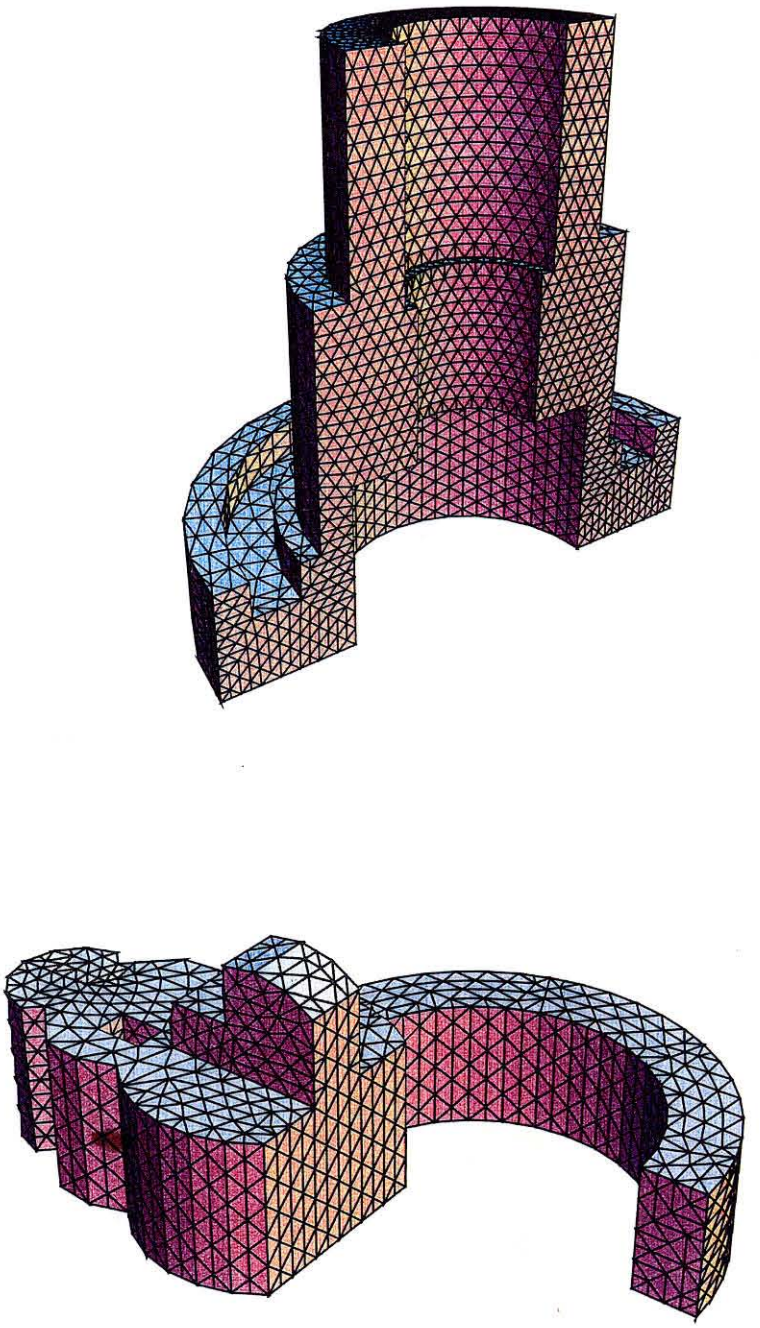

Figure 2.23: Meshes corresponding to shapes given by a surface triangulation (continued)

Chapter 3 Lagrangian finite element analysis of Newtonian fluid flows

3.1 Introduction

The equations of motion of Newtonian fluids are most commonly formulated in eulerian form, leading to the Navier-Stokes equations. In many situations of interest, eulerian formulations permit the simulation of fluid flows using a fixed domain or control volume, which is an attractive feature. There are cases, however, in which the conventional eulerian approach is unduly cumbersome. Such is the case, for instance, of free-surface flows, flows involving interfaces between different species of fluids, and problems in which fluids are coupled to solids undergoing large deformations. The difficulty inherent to the eulerian treatment of these problems has spawned a vast literature. Some attempts to overcome these difficulties have been the mark and cell (MAC) technique originally developed by Harlow and Welch [50] and ALE methods (*e.g.*, [117], [37], [57]).

By contrast, the possibility of describing fluid flows within a fully lagrangian framework, which renders the treatment of free surfaces and interfaces–as well as the compatibility between solids and fluids– trivial, has not correspondingly been explored, barring a few notable exceptions. The earliest fully lagrangian treatment of viscous flows was seemingly advanced by Hirt *et al.* [54]. In their pioneering work [14], Belytschko *et al.* noted the advantages of the lagrangian formulation for problems of fluid-structure interaction involving large structural deformations. Other noteworthy early works are those of Bach *et al* [4] and Ramaswamy *et al.* [119] [118]. These approaches are based on a reformulation of the Navier-Stokes equations in material coordinates, which subsequently are updated via an *ad hoc* iterative procedure. However, because these methods were implemented on a fixed

mesh, they were limited in the extent of the geometrical effects they could account for. As a notable exception, Kawahara *et al.* ([65]) introduced a simple mesh rezoning technique and applied it to the simulation of solitary wave propagation.

In the past, the main technological obstacle standing in the way of fully lagrangian finite element methods for fluids has been the lack of automated and adaptive meshing. Indeed, lagrangian analyses based on a fixed mesh, such as carried out in the references listed above, inevitably lead to severe element distorsion soon after the inception of the flow and, consequently, are of limited scope. However, recent advances in meshing [80], [108] enable the continuous remeshing of the fluid mass as the flow proceeds, which effectively opens the way to the application of lagrangian methods. The feasibility of the lagrangian paradigm as it bears on unconstrained *solid* flows, such as occur in terminal ballistics and high-speed machining, has been amply established, [91], [18], [19].

In the present thesis and in [113], we develop a fully lagrangian finite element method for the analysis of Newtonian flows based on continuous and adaptive remeshing. Our approach furnishes, in effect, a fully lagrangian implementation of the compressible Navier-Stokes equations. The principal advantage of the present approach lies in the treatment of boundary conditions at material surfaces such as free boundaries, fluid/fluid or fluid/solid interfaces, specially where highly deformable solids are concerned. In contrast to eulerian approaches, boundary conditions are enforced at material surfaces *ab initio* and therefore require no special attention. Expressions for the consistent tangents are provided as part of the outcome of the formulation, enabling fully implicit analysis with optimal equilibrium convergence. These consistent tangents are obtained by direct linearization of the incremental equations.

For simplicity, we restrict attention to two-dimensional flows. The accuracy of our approach is assessed by comparison of the solution for the sloshing problem with existing numerical results and its versatility demonstrated through a simulation of wave breaking. The ability of the method to follow simply the evolution of the surface profile as the wave breaks is noteworthy.

3.2 Lagrangian description of Newtonian flows

Consider a body initially occupying a reference configuration B_0, and a motion

$$x_i = \phi_i(\mathbf{X}, t) \tag{3.1}$$

over B_0. Here, $\mathbf{X} \in B_0$ are the material or lagrangian coordinates of a material particle, and $\mathbf{x}$ the corresponding spatial or eulerian coordinates at time t, as determined by the deformation mapping ϕ. We consider a general initial value problem in the lagrangian form:

$$F_{iJ} = \phi_{i,J} \quad \text{in } B_0 \tag{3.2}$$

$$\phi_i = \bar{\phi}_i \quad \text{on } \partial B_{01} \tag{3.3}$$

$$P_{iJ,J} + \rho_0 B_i = \rho_0 \ddot{\phi}_i \quad \text{in } B_0 \tag{3.4}$$

$$P_{iJ} N_J = \bar{T}_i \quad \text{on } \partial B_{02} \tag{3.5}$$

$$P_{iJ} = P_{iJ}(\mathbf{F}, \dot{\mathbf{F}}) \quad \text{in } B_0 \tag{3.6}$$

$$\phi_i(\mathbf{X}, 0) = \phi_i^{(0)}(\mathbf{X}) \quad \text{in } B_0 \tag{3.7}$$

$$\dot{\phi}_i(\mathbf{X}, 0) = V_i^{(0)}(\mathbf{X}) \quad \text{in } B_0 \tag{3.8}$$

where F_{iJ} are the deformation gradients, $\bar{\phi}_i$ are the displacement boundary conditions on the reference displacement boundary ∂B_{01}, P_{iJ} is the Piola-Kirchhoff stress tensor, ρ_0 is the mass density in the reference configuration, B_i are the applied body forces per unit mass in the reference configuration, N_J is the outward unit normal to the reference boundary ∂B_0, $\bar{T}_i$ are the traction boundary conditions on the reference traction boundary ∂B_{02} and $\phi_i^{(0)}(\mathbf{X})$ and $V_i^{(0)}(\mathbf{X})$ are the initial displacement and velocity conditions. The Piola-Kirchhoff stress tensor P_{iJ} and the Cauchy stress tensor σ_{ij} are related as

$$P_{iJ} = (J \sigma_{ij} F_{Jj}^{-1}) \circ \phi \tag{3.9}$$

where $\circ$ denotes composition of functions and

$$J = \det \mathbf{F} \tag{3.10}$$

is the Jacobian of the deformation.

For a Newtonian fluid the constitutive equations are

$$\sigma_{ij} = 2\mu d_{ij}^{\text{dev}} + p\delta_{ij} \tag{3.11}$$

where σ_{ij} are the components of the Cauchy stress tensor, μ is the fluid's viscosity, d_{ij}^{dev} is the deviatoric part of the rate of deformation tensor

$$d_{ij} = \frac{1}{2}(v_{i,j} + v_{j,i}), \tag{3.12}$$

with

$$v_i = \dot{\phi}_i \circ \phi^{-1} \tag{3.13}$$

representing the components of the spatial velocity vector, and p is the pressure, which derives from an equation of state. For a compressible fluid we assume the pressure p to depend only on the volumetric part of the deformation, *i.e.*,

$$p = p(J), \tag{3.14}$$

whereas for an incompressible Newtonian fluid p follows from the constraint

$$J = 1 \tag{3.15}$$

To render these equations in finite element form, we begin by recasting (3.4) in the weak form

$$\int_{B_0} [P_{iJ}\eta_{i,J} - \rho_0(B_i - \ddot{\phi}_i)\eta_i]dV_0 - \int_{\partial B_{02}} \bar{T}_i\eta_i dS_0 = 0 \tag{3.16}$$

where the test functions η_i satisfy the homogeneous essential boundary conditions

$$\eta_i = 0 \quad \text{on } \partial B_{01} \tag{3.17}$$

Pushing (3.16) forward to the spatial configuration leads to

$$\int_B [\sigma_{ij}\eta_{i,j} - \rho(b_i - a_i)\eta_i]dV - \int_{\partial B_2} \bar{t}_i \eta_i dS = 0 \tag{3.18}$$

where $B = \phi(B_0)$ and $\partial B_2 = \phi(\partial B_{02})$ are the deformed domain and traction boundary, respectively. Finally, an application of (3.11) results in

$$\int_B [\sigma_{ij}^{\text{dev}}\eta_{(i,j)} + p div\eta - \rho(b_i - a_i)\eta_i]dV - \int_{\partial B_2} \bar{t}_i \eta_i dS = 0 \tag{3.19}$$

which is the point of departure for the finite element implementation described in the sequel.

3.3 Finite element implementation

3.3.1 Spatial discretization

Next we seek to determine finite element interpolants of the form

$$\phi_{\text{h}i}(\mathbf{X}, t) = \sum_{a}^{nodes} x_{ia}(t) N_a(\mathbf{X}) \tag{3.20}$$

which approximate the exact motion $\phi_i(\mathbf{X}, t)$. In (3.20), $x_{ia}(t) = \phi_{\text{h}i}(\mathbf{X}_a, t)$ are the spatial nodal coordinates, $\mathbf{X}_a$ are the material nodal coordinates, and N_a are the undeformed or material shape functions. Inserting this representation into (3.18), a standard derivation leads to the semi-discrete equations

$$\sum_b M_{iakb}\ddot{x}_{kb} + f_{ia}^{\text{int}}(\mathbf{x}, \dot{\mathbf{x}}) = f_{ia}^{\text{ext}}(t) \tag{3.21}$$

where

$$M_{iakb} = \sum_e \int_{\Omega_o^e} \rho_0 \delta_{ik} N_a^e N_b^e d\Omega_0 \tag{3.22}$$

$$f_{ia}^{\text{int}} = \sum_e \int_{\Omega_o^e} P_{iI} N_{a,I}^e d\Omega_0 \tag{3.23}$$

denote the consistent mass matrix and the internal force array, respectively, $\ddot{\mathbf{x}}$ is the acceleration array and $\mathbf{f}^{\text{ext}}$ is the external force array resulting from the applied body forces and surface tractions.

We adopt the six noded composite finite element devised by Camacho and Ortiz [18] and mass lumping. It should be carefully noted that the element body forces, *i.e.*, gravity forces, must be lumped accordingly in order for constant accelerations to result from the application of a constant force field, as required.

3.3.2 Temporal discretization

For the mass-dominated problems of interest here, such as the propagation of gravity waves, an implicit treatment of time is particularly attractive, if not mandatory. Consequently, we integrate the system of nonlinear ordinary equations (3.21) in time by recourse to Newmark's algorithm (*e.g.*, [58], [11])

$$\begin{aligned}
&\mathbf{x}_{n+1} = \mathbf{x}_n + \Delta t \mathbf{v}_n + \Delta t^2 \left[\left(\frac{1}{2} - \beta \right) \mathbf{a}_n + \beta \mathbf{a}_{n+1} \right] \\
&\mathbf{v}_{n+1} = \mathbf{v}_n + \Delta t [(1-\gamma)\mathbf{a}_n + \gamma \mathbf{a}_{n+1}] \\
&\mathbf{M}\mathbf{a}_n + \mathbf{f}^{\text{int}}(\mathbf{x}_n, \mathbf{v}_n) = \mathbf{f}_n^{\text{ext}} \\
&\mathbf{M}\mathbf{a}_{n+1} + \mathbf{f}^{\text{int}}(\mathbf{x}_{n+1}, \mathbf{v}_{n+1}) = \mathbf{f}_{n+1}^{\text{ext}}
\end{aligned} \tag{3.24}$$

where $\mathbf{x}_n = \mathbf{x}(t_n)$, $\mathbf{v}_n = \dot{\mathbf{x}}(t_n)$, $\mathbf{a}_n = \ddot{\mathbf{x}}(t_n)$, $\mathbf{f}_n^{\text{ext}} = \mathbf{f}^{\text{ext}}(t_n)$, $t_n = n\Delta t$ and $0 \leq \beta \leq 0.5, 0 \leq \gamma \leq 1$ are the algorithm's parameters. It is interesting to note that

Newmark's algorithm can be rephrased in the multistep form

$$\mathbf{M}\frac{\mathbf{x}_{n+1}-2\mathbf{x}_n+\mathbf{x}_{n-1}}{\Delta t^2}+\alpha_{-1}(\mathbf{f}^{\text{int}}-\mathbf{f}^{\text{ext}})_{n-1}+\alpha_0(\mathbf{f}^{\text{int}}-\mathbf{f}^{\text{ext}})_n+\alpha_1(\mathbf{f}^{\text{int}}-\mathbf{f}^{\text{ext}})_{n+1}=0 \tag{3.25}$$

where the parameters $(\alpha_{-1},\alpha_0,\alpha_1)$ are related to Newmark's parameters (β,γ) as

$$\alpha_{-1}=\frac{1}{2}+\beta-\gamma,\qquad \alpha_0=\frac{1}{2}-2\beta+\gamma,\qquad \alpha_1=\beta \tag{3.26}$$

The nonlinear system of equations (3.24) may be solved by a Newton-Raphson iteration, leading to successive iterates $(\mathbf{x}_{n+1}^{(k)},\mathbf{v}_{n+1}^{(k)},\mathbf{a}_{n+1}^{(k)})$, $k=0,\ldots$. The starting iterate coincides with the Newmark predictor

$$\begin{aligned}\mathbf{x}_{n+1}^{(0)}&=\mathbf{x}_n+\Delta t\mathbf{v}_n+\Delta t^2(\frac{1}{2}-\beta)\mathbf{a}_n\\ \mathbf{v}_{n+1}^{(0)}&=\mathbf{v}_n+\Delta t(1-\gamma)\mathbf{a}_n\\ \mathbf{a}_{n+1}^{(0)}&=0\end{aligned} \tag{3.27}$$

By this means, the system of nonlinear equations is reduced to

$$\begin{aligned}\mathbf{x}_{n+1}&=\mathbf{x}_{n+1}^{(0)}+\beta\Delta t^2\mathbf{a}_{n+1}\\ \mathbf{v}_{n+1}&=\mathbf{v}_{n+1}^{(0)}+\gamma\Delta t\mathbf{a}_{n+1}\\ \mathbf{M}\mathbf{a}_{n+1}&+\mathbf{f}^{\text{int}}(\mathbf{x}_{n+1},\mathbf{v}_{n+1})=\mathbf{f}_{n+1}^{\text{ext}}\end{aligned} \tag{3.28}$$

In order to compute the $(k+1)$th iterate, (3.28) is consistently linearized about the kth iterate leading to the equivalent linear static problem

$$\left(\hat{\mathbf{K}}_{n+1}^{(k)}+\frac{\gamma}{\beta\Delta t}\hat{\mathbf{C}}_{n+1}^{(k)}+\frac{1}{\beta\Delta t^2}\mathbf{M}\right)\mathbf{u}=\mathbf{f}_{n+1}^{\text{ext}}-(\mathbf{f}^{\text{int}})_{n+1}^{(k)}-\mathbf{M}\mathbf{a}_{n+1}^{(k)} \tag{3.29}$$

where $\mathbf{u}$ is the incremental displacement array and

$$\mathbf{K}=\frac{\partial\mathbf{f}^{\text{int}}}{\partial\mathbf{x}}(\mathbf{x},\mathbf{v}),\qquad \mathbf{C}=\frac{\partial\mathbf{f}^{\text{int}}}{\partial\dot{\mathbf{x}}}(\mathbf{x},\mathbf{v}) \tag{3.30}$$

are the tangent stiffness and tangent damping matrices, respectively. A trite but straightforward calculation gives the consistent element tangents in the form

$$\begin{aligned} K^e_{iakb} &= \frac{\partial f^e_{ia}}{\partial X_{kb}} \\ &= \int_{\Omega^e_t} [\sigma_{im}(n_{b,k}n_{a,m} - n_{b,m}n_{a,k}) + \mu(v_{i,k}n_{b,j}n_{a,j} - v_{j,k}n_{b,i}n_{a,j} \\ &+ \frac{2}{3}v_{l,k}n_{b,l}n_{a,i}) + \frac{dp}{dJ}Jn_{b,k}n_{a,i}]d\Omega_t \end{aligned} \tag{3.31}$$

and

$$C^e_{iakb} = \frac{\partial f^e_{ia}}{\partial \dot{X}_{kb}} = \int_{\Omega^e_t} \mu(\delta_{i,k}n_{b,m}n_{a,m} + n_{b,i}n_{a,k} - \frac{2}{3}n_{b,k}n_{a,i})dV_t \tag{3.32}$$

where n_a are the deformed or spatial shape functions.

The precise form of these consistent tangents does not seem to have been derived before. Following the computation of $\mathbf{u}$, the nodal coordinates, velocities and accelerations are updated through an application of the Newmark correctors

$$\begin{aligned} \mathbf{x}^{(k+1)}_{n+1} &= \mathbf{x}^{(k)}_{n+1} + \mathbf{u} \\ \mathbf{v}^{(k+1)}_{n+1} &= \mathbf{v}^{(k)}_{n+1} + \frac{\gamma\mathbf{u}}{\beta\Delta t} \\ \mathbf{a}^{(k+1)}_{n+1} &= \mathbf{a}^{(k)}_{n+1} + \frac{\mathbf{u}}{\beta\Delta t^2} \end{aligned} \tag{3.33}$$

The iteration terminates when a certain tolerance is met, *e.g.*, when

$$\frac{\| \mathbf{x}^{(k+1)}_{n+1} - \mathbf{x}^{(k)}_{n+1} \|}{\| \mathbf{x}^{(1)}_{n+1} - \mathbf{x}^{(0)}_{n+1} \|} \leq \text{TOL} \tag{3.34}$$

Provided that the starting point of the iteration is within the radius of convergence of the solution, the use of the exact tangents (3.31) and (3.32) results in quadratic convergence.

3.4 Adaptive meshing

A difficulty which is encountered when Lagrangian methods are applied to problems involving unconstrained flow is the severe deformation-induced mesh distortion which is inevitably incurred. This difficulty can be effectively sidestepped by recourse to continuous and adaptive remeshing [91], [19],[20]. Mesh adaption also furnishes an efficient means of resolving multiple scales in the solution with a minimum of degrees of freedom. An effective adaptive meshing capability must address two types of issues: representational, i. e., issues pertaining to the representation of domains; and analytical, including automatic meshing, adaption indicators and mesh-to-mesh transfer operators. A few salient issues among these are subsequently addressed in turn.

In calculations we represent domains as hierarchical systems ([18], [5], [110], [62]). At the top level, the topological graph points to a set of bodies. A body may in turn comprise several subbodies, *e.g.*, composed of different materials. The boundary of each subbody is decomposed into a collection of closed loops. The loops can be oriented consistently so as to unambiguously define the interior and the exterior of the subbody. Each loop is partitioned into edges. An edge may appear, albeit with different orientations, in the boundaries of two different subbodies. Finally, the geometry of all edges is defined by piecewise quadratic interpolation from a collection of boundary nodes. The use of a sufficiently accurate interpolation of the boundary is essential in order to preserve the mass of the body.

3.4.1 The advancing front algorithm

The boundary representation of the model may be taken as a basis for the triangulation of the interior of the solids. The boundary representation serves the additional purpose of specifying the current contact surfaces in the solid. Advancing front methods [110] constitute specially attractive automatic meshing techniques as they require a minimal set of input data–chiefly, the boundary information–from which both elements and interior nodes are generated simultaneously. Triangular elements are

introduced one by one from the smallest segment on the front, which is taken as the base of the triangle. In the construction of the initial mesh, the size of the elements is determined by recourse to Jin and Wiberg's [62] control line technique. In this approach, the element size is computed as a weighted average of the boundary element sizes. In subsequent meshes, the size of the new elements inserted at the front is selected in accordance with a prespecified mesh density determined *a posteriori* from the solution. The advancing front algorithm terminates when no segments are left in the front. Carefully designed data structures and search algorithms need to be put in place to ensure an $O(N \log N)$ operation count [80].

In our calculations we employ an h-adaption strategy based on empirical refinement indicators to estimate the optimal mesh density, leading to simultaneous coarsening and refinement [105],[18]. The target mesh density is determined so as to equidistribute certain indicators over all elements in the mesh. As refinement indicator we adopt the bounded deformation norm of the velocity field [105] which results in refinement (coarsening) in rapidly (slowly) varying regions of the flow. In our implementation, the element size information is interpolated on the old mesh, which serves as a background mesh for the advancing front algorithm.

3.4.2 Mesh-to-mesh transfer operator

The consistent formulation of transfer operators has been addressed by Ortiz and Quigley [105]. The fundamental question to be ascertained concerns the formulation of consistent finite element equations when all fields at time t_n are supported on a mesh $\mathcal{M}_n$ while the fields at time $t_{n+1} = t_n + \Delta t$ are supported on a different mesh $\mathcal{M}_{n+1}$. Ortiz and Quigley [105] show that, when all finite element representations are introduced into the weak form of the equations of motion, the equilibrium and compatibility equations at t_{n+1} follow directly from the interpolation on $\mathcal{M}_{n+1}$. Ortiz and Quigley [105] further show that the weak form unambiguously determines the transfer operator.

In the context of a total displacement approach, where the reference configuration is fixed at the initial configuration, the deformation and velocity gradients and the

Jacobian of the deformation can be computed directly from the nodal data. Since Newtonian fluids are history independent, *i.e.*, the stresses depend solely on the current spatial velocity gradient and the Jacobian of the deformation (3.11), there is no need to transfer any state variables to the quadrature points of the new mesh. However, in problems of unconstrained flow, such as water waves propagation and breaking, an incremental formulation where the reference configuration is updated frequently is advantageous, as the total deformation mapping nearly loses invertibility with the passage of time. In this case the accumulated Jacobian of the deformation must be transferred from mesh to mesh.

3.5 Validation and applications

3.5.1 Sloshing problems

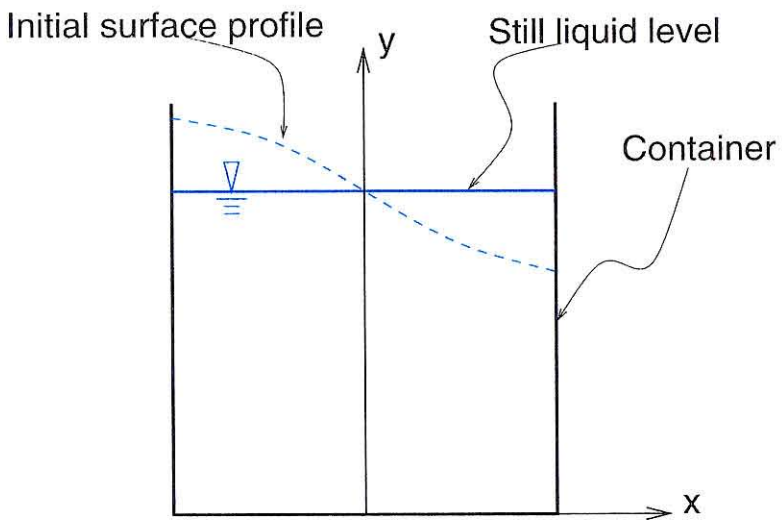

Figure 3.1: Schematic of the sloshing problem

By way of validation of the formulation just described we consider the simple problem of the free oscillation of an incompressible liquid in a container. Numerical results for this problem can be found elsewhere ([119], [117]). Fig. 3.1 depicts a schematic of the problem. Following Ramaswamy *et al.* ([119], [117]) we consider a

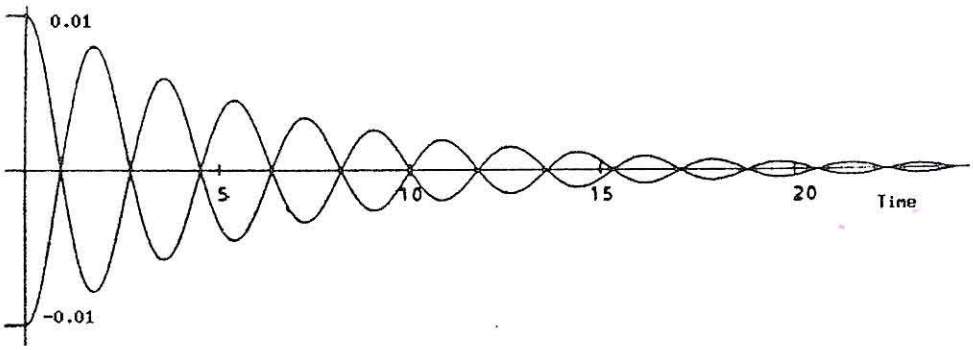

(a) Results from [117]

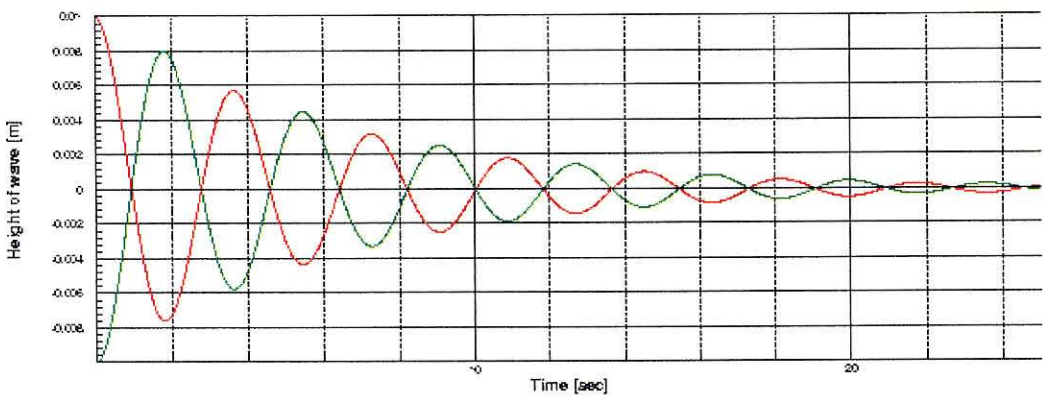

(b) Results for the present method

Figure 3.2: Time histories of surface elevation amplitude for the sloshing problem

square liquid column of width b with an initial surface profile corresponding to the first antisymmetric mode of vibration, i. e.,

$$\eta(x, 0) = a \sin \frac{\pi}{b} x$$

where a is the amplitude of oscillation. For the sake of comparison with previously published numerical results, we adopt a very small value for the amplitude ($a = 0.01$). In view of this small amplitude, the calculations can be carried out on a fixed mesh. The container walls are assumed to be impermeable and allow for free slip. A viscosity $\nu = 0.01$ is adopted in the calculations. Fig. 3.2 shows the computed time histories of

$\eta\left(\pm\frac{b}{2}, t\right)$ together with the same time histories reported by Ramaswamy *et al.* ([119], [117]). As is evident from the figure, the two sets of results are in close agreement. It should be noted, however, that the geometric effects in this example are insignificant and that, in consequence, the full potential of the present method is not realized.

3.5.2 Wave breaking

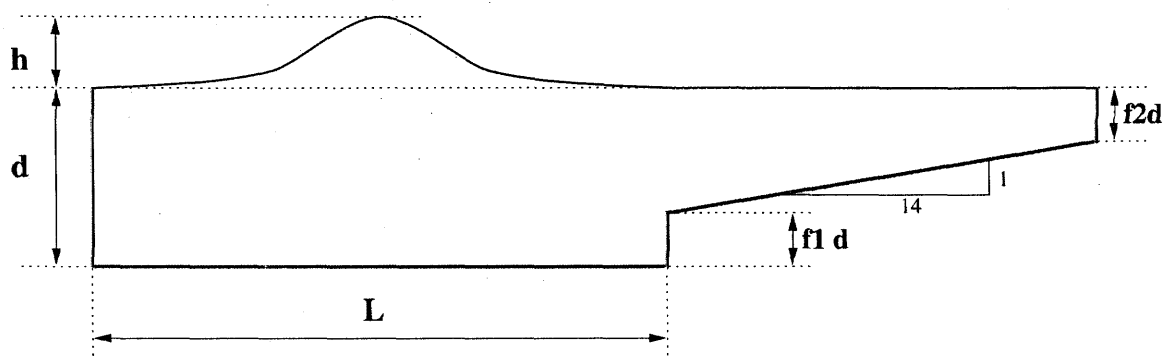

Figure 3.3: Schematic of the analysis problem

In this section we present a simulation of the propagation of a water wave and its breaking due to shoaling over a plane slope. The geometry of the problem is shown in Fig. 3.3. The inviscid problem has been analyzed using boundary elements [47] and the viscous case using ALE methods [117]. The initial conditions are taken from the potential theory solution of a solitary wave of finite amplitude propagating without change of shape [67]. In Laitone's solution, which is frequently used for comparison,

the velocity, pressure and free surface elevation are:

$$u = \sqrt{gd}\frac{H}{d} sech^2 \left[\sqrt{\frac{3H}{4d^3}}(x - ct)\right] \tag{3.35}$$

$$v = \sqrt{3gd}\left(\frac{H}{d}\right)^{3/2} \frac{y}{d} sech^2 \left[\sqrt{\frac{3H}{4d^3}}(x - ct)\right] tanh \left[\sqrt{\frac{3H}{4d^3}}(x - ct)\right] \tag{3.36}$$

$$\eta = d + H sech^2 \left[\sqrt{\frac{3H}{4d^3}}(x - ct)\right] \tag{3.37}$$

$$p = \rho g(\eta - y) \tag{3.38}$$

$$c = \sqrt{gd\left(1 + \frac{H}{d}\right)} \tag{3.39}$$

As noted by Ramaswamy [117], Laitone's solution holds for an infinitely long channel. However, for purposes of simulation it suffices to truncate the domain of analysis at a distance $L/2$ from the wave crest where the fluid is essentially still, *e.g.*, where the surface elevation $\eta = 0.01H$. The result is

$$\frac{L}{d} = 6.9\left(\frac{d}{H}\right)^{1/2}$$

In simulations, we take the constant depth region to be of length L. The still water depth d is set to 10 m and the wave height H to 5 m. The slope of the shoaling bottom is set to 1/14. The acceleration of gravity is set to 9.8 m/s. The density of water is $\rho = 1000$ Kg/m^3, the viscosity is $\mu = 1.01 \times 10^{-3}$ Ns/m^2, and the compressibility modulus is $K = 2.04 \times 10^9$ N/m^2.

Fig. 3.4 shows the initial adapted mesh and the velocity and pressure initial conditions. The initial mesh is adapted applying the refinement criterion presented in section 3.4 to the initial velocity field. Figs. 3.5 - 3.9 chronicle the evolution of the solution at times 4.0, 8.0, 9.0, 9.5 and 9.8, respectively. Four stages can be identified in the solution:

Propagation: The wave travels over the constant depth bottom towards the slope with no ostensible change of shape other than a small dispersion effect, Fig. 3.5.

Steepening As the wave hits the slope, a strongly nonlinear behavior becomes apparent. In particular, the crest of the wave accelerates while the trough lags behind. Eventually, the wave profile develops a vertical tangent and ceases to be a graph, Fig. 3.6.

Breaking Subsequently, the water jet formed at the crest plunges until it comes into contact with the nearly still surface of the water ahead, at which point the simulation is stopped, Figs. 3.7 - 3.9.

The ability of the model to faithfully simulate the various stages of wave breaking is noteworthy. Good aspect ratios are maintained throughout the simulation. In addition, the mesh adaptively resolves the regions of rapid variation of the velocity field while remaining comparatively coarse in the quiescent regions, which tends to keep the number of degrees of freedom within reasonable bounds. The analysis requires 9800 implicit time steps of size $\Delta t = 10^{-3}$ s. A strong quadratic convergence is maintained throughout the simulation, with a maximum of three Newton-Raphson iterations per time step required to attain a relative tolerance TOL of 10^{-13}. The number of equilibrium iterations to convergence typically increases to as many as four immediately following a mesh adaption. This slow-down in convergence is caused by the interpolation errors introduced by the mesh-to-mesh transfer operator.

Wave profiles at various time steps, shifted to the nominal (unperturbed) wave front center according to the nominal celerity (Eq. 3.39), are presented in Fig. 3.10.

3.6 Summary and conclusions

A fully lagrangian finite element method for the analysis of Newtonian flows based on continuous and adaptive remeshing has been developed. The method is specially advantageous for problems involving free fluid surfaces and interfaces; or the coupling of fluid flows and highly deformable solids. As the flow proceeds, the finite element mesh is maintained undistorted by recourse to continuous and adaptive remeshing. In addition, mesh adaption enables the simultaneous resolution of multiple scales in the

solution. The versatility of the approach has been demonstrated through a simulation of wave breaking. The ability of the model to faithfully simulate the various stages of wave breaking is noteworthy.

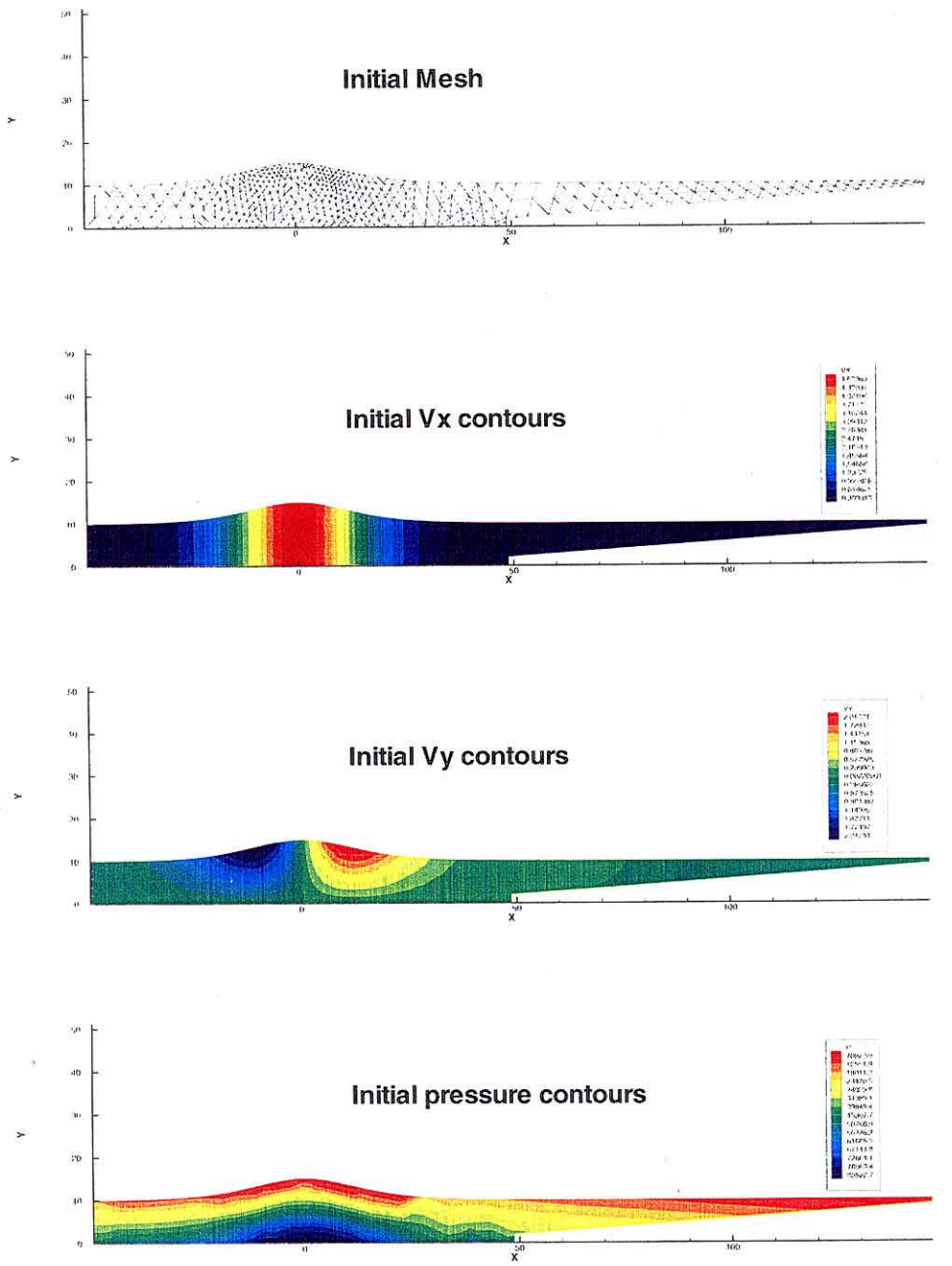

Figure 3.4: Initial conditions and computational mesh

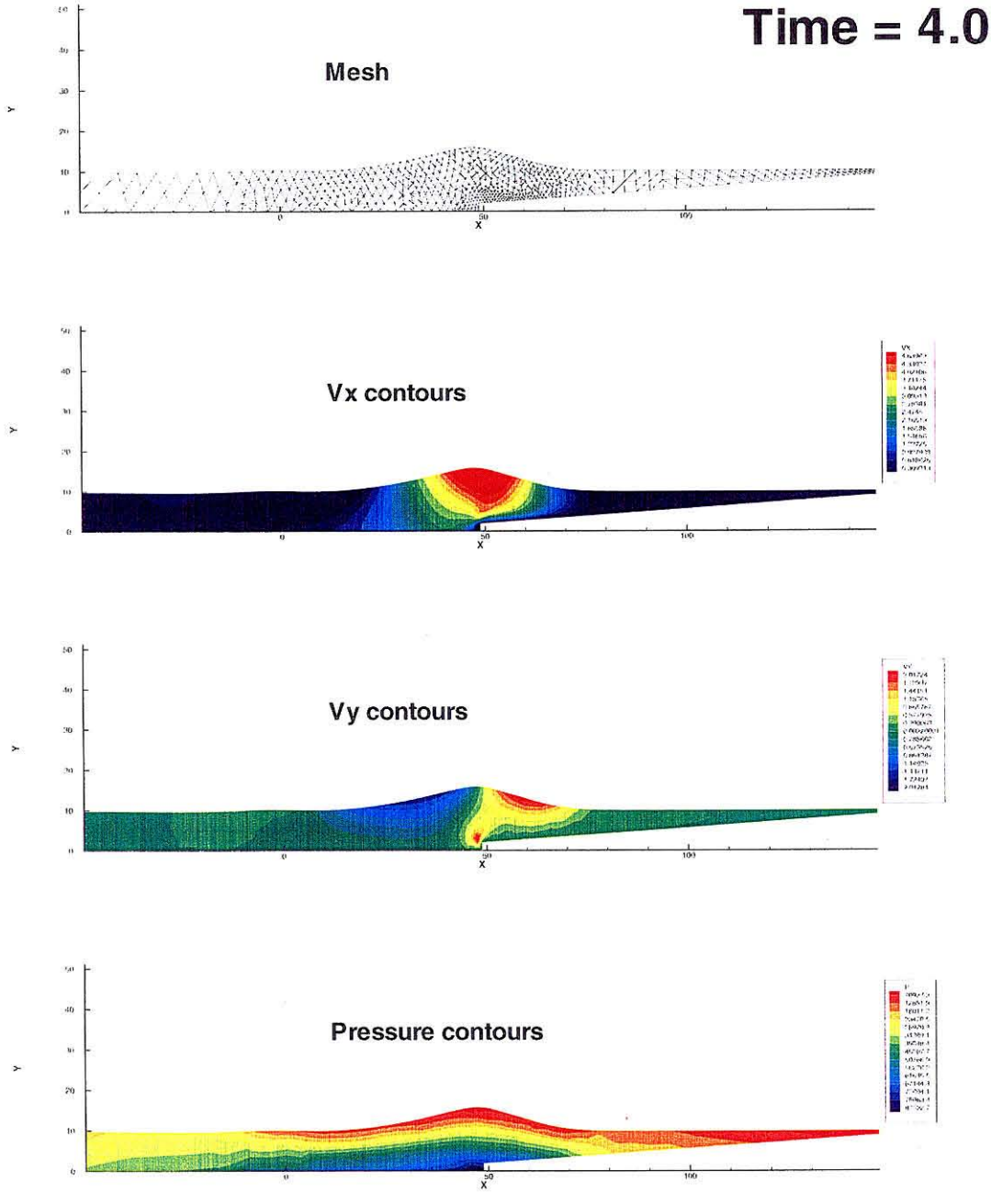

Figure 3.5: Solution fields and wave profile at time=4 sec

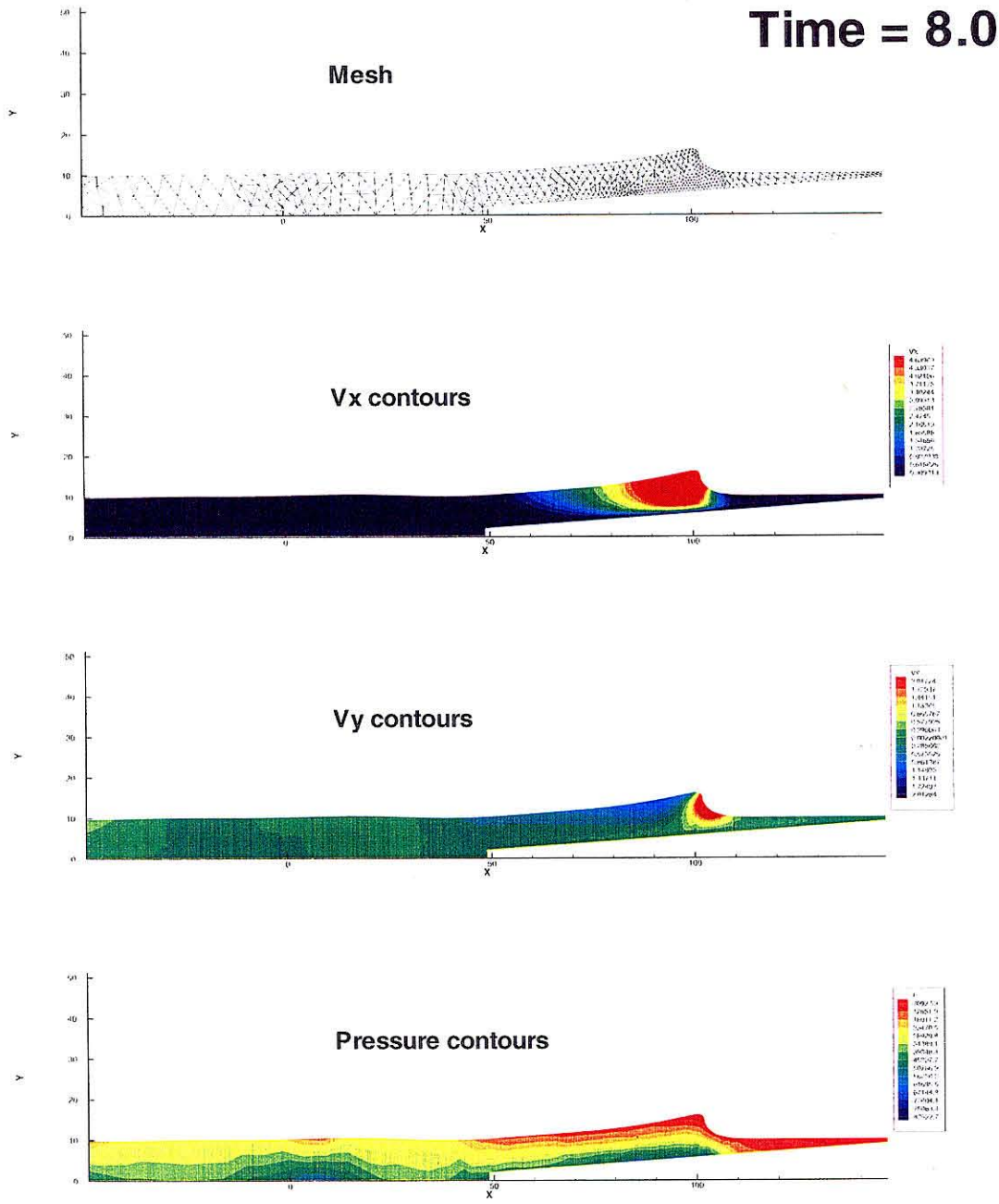

Figure 3.6: Solution fields and wave profile at time=8.0 sec

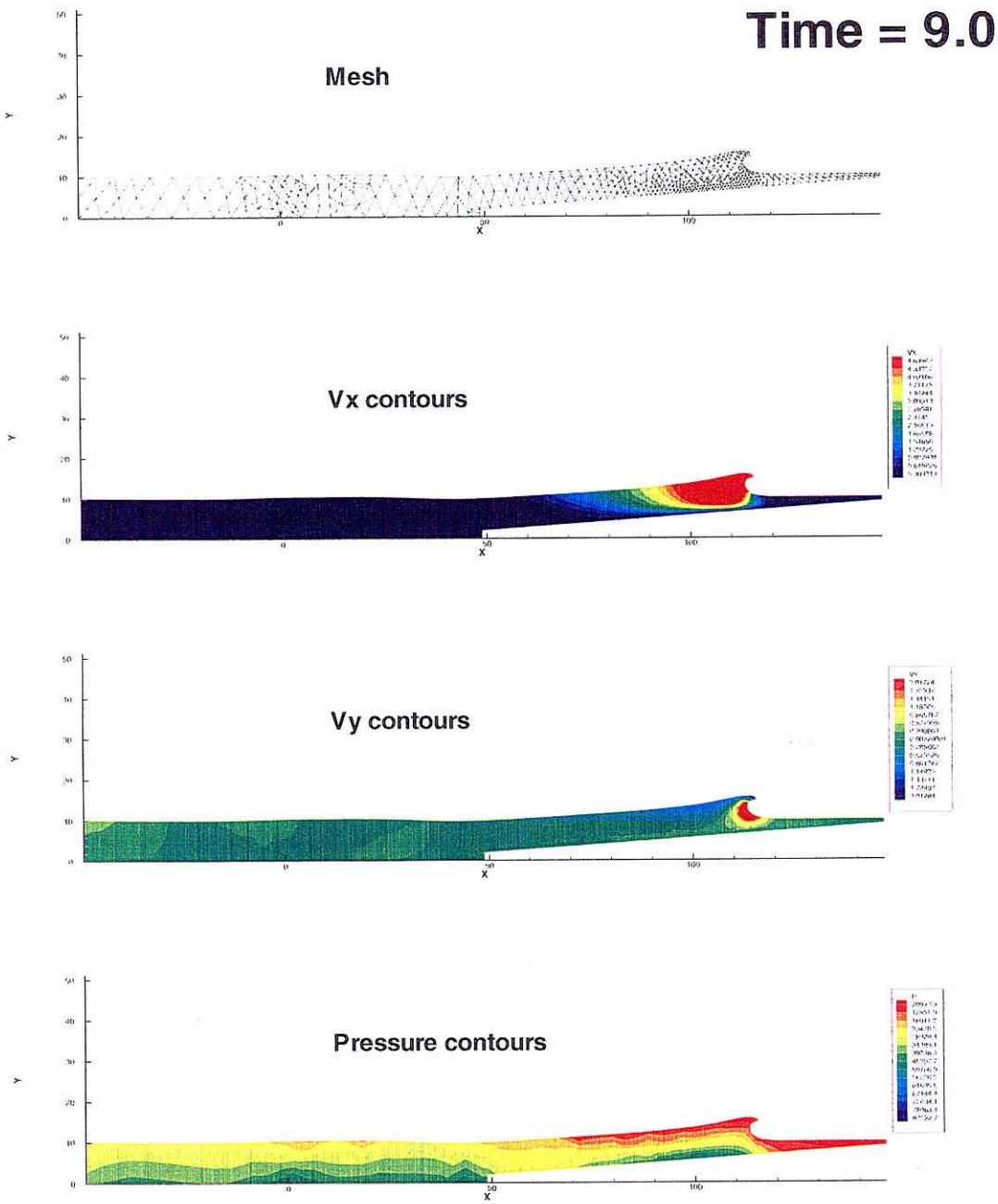

Figure 3.7: Solution fields and wave profile at time=9.0 sec

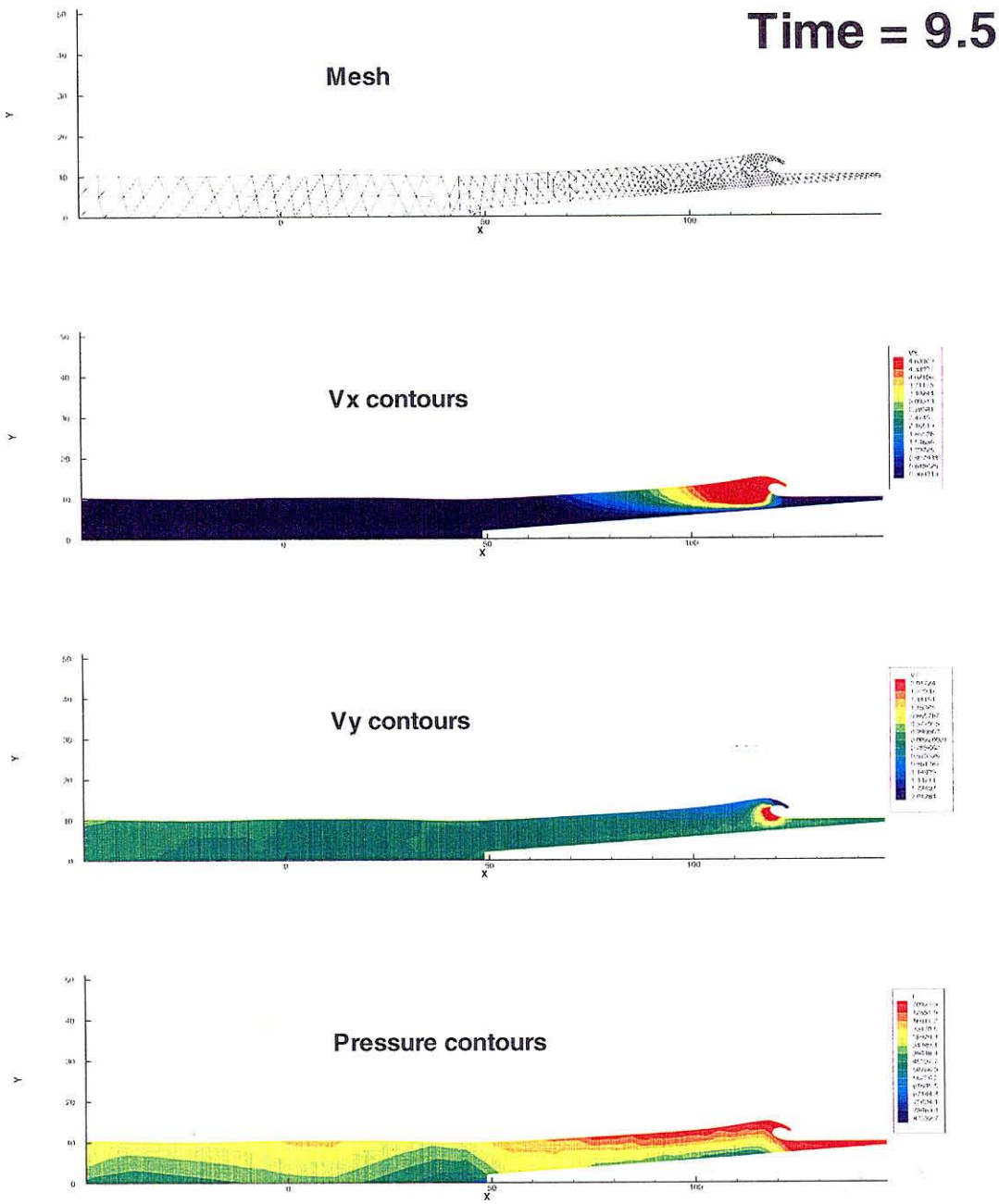

Figure 3.8: Solution fields and wave profile at time=9.5 sec

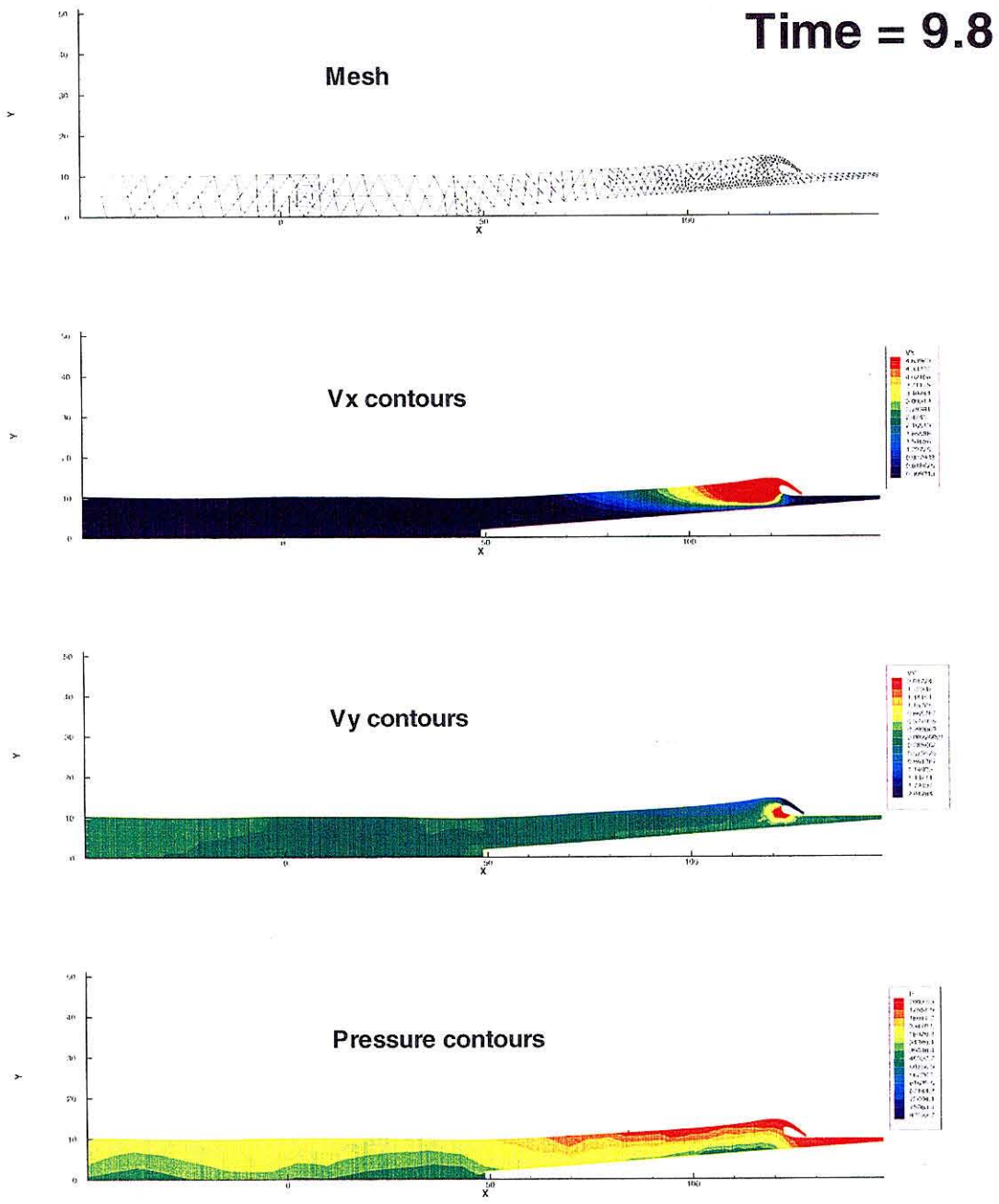

Figure 3.9: Solution fields and wave profile at time=9.8 sec

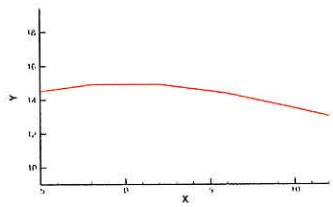

(a) $t = 0sec$

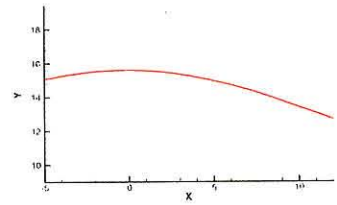

(b) $t = 4.7sec$

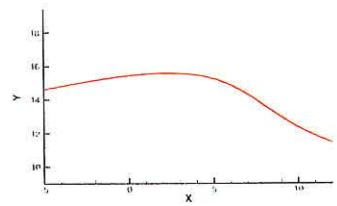

(c) $t = 6.4sec$

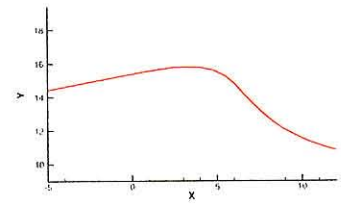

(d) $t = 7.2sec$

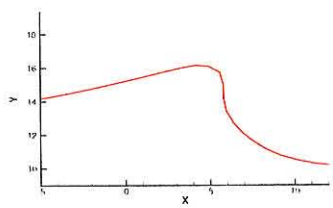

(e) $t = 8.2sec$

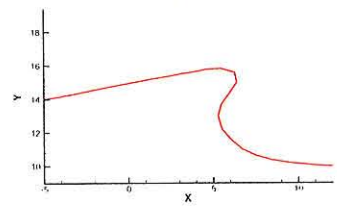

(f) $t = 8.9sec$

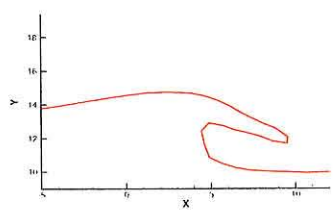

(g) $t = 9.7sec$

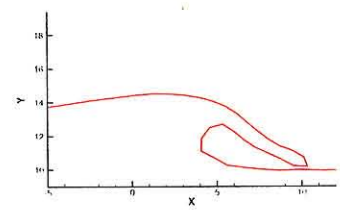

(h) $t = 9.9sec$

Figure 3.10: Details of wave profile at various times

Chapter 4 Mesh adaption in nonlinear dynamic problems

4.1 Introduction

The adaptive remeshing strategy adopted in Chapter 3 is based in estimating the optimal mesh size distribution in accordance with empirical refinement indicators. Whereas the adopted mesh adaption strategy effectively results in refinement (coarsening) in rapidly (slowly) varying regions of the flow, a theoretical rationale is lacking nor does the method provide any guarantee of resulting in convergent approximations to the continuum equations.

The ultimate goal of this thesis is to develop a general framework for mesh adaption in strongly nonlinear dynamic problems. Following [45], the dynamic problem is reduced to an equivalent static problem by recourse to time discretization. The solutions of the incremental boundary value problem for a wide class of materials, including nonlinear elastic materials, compressible Newtonian fluids, and viscoplastic solids, are then shown to obey a minimum principle, provided that the constitutive updates are formulated appropriately. This minimum principle can be taken as a basis for error estimation. In particular, we chose to monitor the error of a lower-order projection of the finite element solution. The optimal mesh size distribution then follows from error indicators which are: purely local, i. e., can be computed element-by-element; and *a posteriori*, i. e., follow directly from the finite element solution. This is in contrast to the presently available error indicators, even for linear problems, whose evaluation requires cumbersome—and often *ad hoc*—smoothing steps involving patches of elements (e. g., [143, 144, 30]). As noted by Ortiz and Quigley [105], the requisite mesh-to-mesh transfer operators, whereby the nodal and state variables are remapped to the new mesh, also follow consistently from the variational

principle.

We demonstrate the accuracy, robustness and versatility of the computational framework with the aid of convergence studies and selected examples of application, including nonlinear elastic fracture mechanics and isothermal and adiabatic shocks in highly compressible media.

4.2 General framework

We begin by formulating the general initial-boundary value problem of bodies undergoing large dynamic deformations. We place particular emphasis in the development of a constitutive framework encompassing a wide range of material behavior, including finite elasticity, viscosity, and viscoplasticity. In subsequent sections, this framework is taken as the basis for formulating constitutive updates possessing a potential structure, which in turn will enable a variational characterization of the initial-boundary value problem.

4.2.1 Field equations

We shall be concerned with the motions of continuous bodies. We select the configuration $B_0 \subset \mathbb{R}^d$ of the body at time t_0 as the reference configuration. The coordinates $\mathbf{X}$ of points in B_0 are used to identify material particles throughout the motion. The motion of the body is described by the deformation mapping

$$\mathbf{x} = \boldsymbol{\varphi}(\mathbf{X}, t), \qquad \mathbf{X} \in B_0 \tag{4.1}$$

Thus, $\mathbf{x}$ is the location of material particle $\mathbf{X}$ at time t. We shall denote by B_t the deformed configuration of the body at time t. The material velocity and acceleration fields follow from (4.1) as $\dot{\boldsymbol{\varphi}}(\mathbf{X}, t)$ and $\ddot{\boldsymbol{\varphi}}(\mathbf{X}, t)$, $\mathbf{X} \in B_0$, respectively, where a superposed dot denotes partial differentiation with respect to time at fixed $\mathbf{X}$. The local deformation of infinitesimal material neighborhoods is described by the deformation

gradients

$$\mathbf{F} = \nabla_0 \boldsymbol{\varphi}(\mathbf{X}, t), \qquad \mathbf{X} \in B_0 \tag{4.2}$$

where the components of the material gradient $\nabla_0 f$ of a function $f(\mathbf{X})$ are the partial derivatives of f with respect to $\mathbf{X}$. The scalar function

$$J = \det\big(\mathbf{F}(\mathbf{X}, t)\big) \tag{4.3}$$

is the Jacobian of the deformation.

The motion of the body is subject to conservation of linear momentum. The local form of linear momentum balance is (*cf.* [89])

$$\rho_0 \ddot{\boldsymbol{\varphi}} - \nabla_0 \cdot \mathbf{P} = \rho_0 \mathbf{B}, \qquad \text{in } B_0 \tag{4.4}$$

where $\rho_0(\mathbf{X})$ is the mass density over B_0, $\mathbf{B}(\mathbf{X}, t)$ are the body forces per unit mass, and $\mathbf{P}(\mathbf{X}, t)$ is the first Piola-Kirchhoff stress tensor. The Cauchy stress tensor follows from $\mathbf{P}$ in the form

$$\boldsymbol{\sigma} = J^{-1} \mathbf{P} \mathbf{F}^T \tag{4.5}$$

Conservation of angular momentum requires $\boldsymbol{\sigma}$ to be symmetric.

For the purpose of formulating boundary conditions, we partition the boundary ∂B_0 of B_0 into a Dirichlet or displacement boundary ∂B_{01} and a Neumann or traction boundary ∂B_{02}. The displacement boundary conditions then take the form:

$$\boldsymbol{\varphi} = \bar{\boldsymbol{\varphi}}, \qquad \text{on } \partial B_{01} \tag{4.6}$$

where $\bar{\boldsymbol{\varphi}}(\mathbf{X}, t)$ is the prescribed deformation mapping on ∂B_{01}. The traction boundary

conditions then take the form:

$$\mathbf{P} \cdot \mathbf{N} = \bar{\mathbf{T}}, \qquad \text{on } \partial B_{02} \tag{4.7}$$

where $\mathbf{N}$ is the unit outward normal to ∂B_{02} and $\bar{\mathbf{T}}(\mathbf{X}, t)$ are the prescribed tractions applied to ∂B_{02}. Finally, dynamic problems require initial conditions $\boldsymbol{\varphi}_0(\mathbf{X})$ and $\dot{\boldsymbol{\varphi}}_0(\mathbf{X})$ to be specified over B_0.

4.2.2 Constitutive relations

In addition to the preceding field equations, we require a constitutive framework within which to describe general classes of materials. To this end, we adopt an internal variable formalism ([84, 85]) to describe inelastic processes and postulate the existence of a Helmholtz free energy density $A(\mathbf{F}, \mathbf{Q})$ per unit undeformed volume, where $\mathbf{Q} \in R^N$ is some suitable collection of internal variables. For simplicity, we restrict attention to isothermal processes and omit the dependence of A and all other state functions on temperature. We assume an additive decomposition

$$\mathbf{P} = \mathbf{P}^{\mathrm{e}} + \mathbf{P}^{\mathrm{v}} \tag{4.8}$$

of the first Piola-Kirchhoff stress tensor $\mathbf{P}$ into an equilibrium part $\mathbf{P}^{\mathrm{e}}$ and a viscous part $\mathbf{P}^{\mathrm{v}}$. The equilibrium stress follows from Coleman's relations as

$$\mathbf{P}^{\mathrm{e}} = A_{,\mathbf{F}}\,(\mathbf{F}, \mathbf{Q}) \tag{4.9}$$

If, in addition, the material possesses viscosity, the stresses follow in the form

$$\mathbf{P} = A_{,\mathbf{F}}\,(\mathbf{F}, \mathbf{Q}) + \mathbf{P}^{v}(\dot{\mathbf{F}}; \mathbf{F}, \mathbf{Q}) \tag{4.10}$$

where $\mathbf{P}^v$ is the viscous part of the stresses. We shall assume the usual regularity condition of $\mathbf{P}^v$, namely, that

$$\mathbf{P}^v(\dot{\mathbf{F}};\mathbf{F},\mathbf{Q})\cdot\dot{\mathbf{F}} = o(|\dot{\mathbf{F}}|) \tag{4.11}$$

where, here and subsequently, the dot product between two second-order tensors $\mathbf{A}$ and $\mathbf{B}$ is understood to be $\mathbf{A}\cdot\mathbf{B} \equiv A_{ij}B_{ij}$. The regularity condition (4.11) ensures that quasistatic processes do not result in any viscous dissipation. In order to determine the evolution of the internal variables, suitable kinetic equations must be supplied. Assuming that the rate of the internal processes is determined solely by the local thermodynamic state, the general form of the kinetic equations is

$$\dot{\mathbf{Q}} = \mathbf{f}(\mathbf{F},\mathbf{Q}) \tag{4.12}$$

Additionally,

$$\mathbf{Y} = -A_{,\mathbf{Q}}\,(\mathbf{F},\mathbf{Q}) \tag{4.13}$$

are the thermodynamic 'forces' conjugate to $\mathbf{Q}$. The kinetic relations are said to derive from an inelastic potential if there exists a differentiable function $\psi(\mathbf{Y},\mathbf{Q})$ such that

$$\dot{\mathbf{Q}} = \psi_{,\mathbf{Y}}\,(\mathbf{Y},\mathbf{Q}) \tag{4.14}$$

For single crystals, the concept of inelastic potential was introduced by Rice [122]. Likewise, the viscosity law $\mathbf{P}^v(\dot{\mathbf{F}};\mathbf{F},\mathbf{Q})$ is said to derive from a potential if there exists a function $\phi(\dot{\mathbf{F}};\mathbf{F},\mathbf{Q})$ such that

$$\mathbf{P}^v = \phi_{,\dot{\mathbf{F}}}\,(\dot{\mathbf{F}};\mathbf{F},\mathbf{Q}) \tag{4.15}$$

All the preceding constitutive relations are subject to material frame indifference, i. e., must remain invariant under superimposed rigid body motions.

As an illustration of how particular classes of materials fit into the general constitutive framework just outlined, and for subsequent reference, we conclude this section with a brief discussion of hyperelastic solids, Newtonian fluids and plastic solids.

Hyperelastic solids

The simplest example of material is furnished by hyperelastic solids, for which

$$A = W(\mathbf{F}), \qquad \mathbf{P}^v = \mathbf{0} \tag{4.16}$$

An essential difficulty in dealing with hyperelastic solids is that $W(\mathbf{F})$ is not convex in general [7], and it fails to be quasiconvex for any material which exhibits phase transitions (see, e. g., [32]). This lack of quasiconvexity often gives rise to arbitrarily fine oscillations in the solution (see, e. g., [8, 28]), which compounds matters of mesh adaption. However, Friesecke and Dolzmann have shown that certain forms of linear viscosity regularize the problem and render the effective time-discretized energy density (cf. Section 4.3.2) quasiconvex for sufficiently small time step.

In the calculations reported in subsequent sections, we employ a simple model of a Neo-Hookean solid extended to the compressible range characterized by a strain energy density of the form

$$W(\boldsymbol{C}) = \frac{\lambda_0}{2}(\log J)^2 - \mu_0 \log J + \frac{\mu_0}{2} tr(\boldsymbol{C}) \tag{4.17}$$

where $J = \det(F)$ is the Jacobian of the deformation and λ_0 and μ_0 are material constants. We have used the Neo Hookean model in the numerical tests and examples reported in subsequent sections. The corresponding stress-strain relations are

$$S_{IJ} = 2\frac{\partial W}{\partial C_{IJ}} = \lambda_0 \log J C^{-1}_{IJ} + \mu_0(\delta_{IJ} - C^{-1}_{IJ}) \tag{4.18}$$

while the material tangent moduli are

$$D_{IJKL} = 4\frac{\partial^2 W}{\partial C_{IJ}\partial C_{KL}} = \lambda_0 C^{-1}_{IJ} C^{-1}_{KL} + (\mu_0 - \lambda_0 \log J)(C^{-1}_{IK} C^{-1}_{JL} + C^{-1}_{IL} C^{-1}_{JK}) \tag{4.19}$$

These are positive definite provided that

$$\mu(J) = \mu_0 - \lambda_0 \log J > 0, \qquad k(J) = \lambda_0 + \frac{2}{3}\mu(J) > 0 \tag{4.20}$$

These conditions ensure the convexity of $W(\boldsymbol{C})$.

Compressible Newtonian fluids

Compressible Newtonian fluids provide the foremost example of a material with viscosity. In this case, the free energy density $A(J)$ is a function of the Jacobian of the deformation J, and the viscous stresses follow as

$$\mathbf{P}^v = J\boldsymbol{\sigma}^v\mathbf{F}^{-T} \tag{4.21}$$

where

$$\boldsymbol{\sigma}^v = 2\eta\mathbf{d}^{\text{dev}} \tag{4.22}$$

is the viscous part of the Cauchy stress tensor. In this latter relation,

$$\mathbf{d} = \text{sym}(\dot{\mathbf{F}}\mathbf{F}^{-1}) \tag{4.23}$$

is the rate of deformation tensor, $\mathbf{d}^{\text{dev}}$ is its deviatoric component, and η is the viscosity of the fluid. A simple calculation reveals that the Newtonian viscosity law possess the potential structure (4.15), and that the viscous potential is given by

$$\phi = \eta J\mathbf{d}^{\text{dev}} \cdot \mathbf{d}^{\text{dev}} \tag{4.24}$$

For a compressible Newtonian fluid, eq. (4.10) reduces to

$$\boldsymbol{\sigma} = p(J)\mathbf{I} + 2\eta\mathbf{d}^{\text{dev}} \tag{4.25}$$

where

$$p(J) = A'(J) \tag{4.26}$$

is the equilibrium pressure. A fully lagrangian treatment of Newtonian fluids has been developed in Chapter 3.

Viscoplastic solids

Our final example of material concerns plastic solids. These solids are characterized by the existence of a certain class of deformations $\mathbf{F}^p$, or 'plastic' deformations, which leave the crystal lattice undistorted and unrotated, and, consequently, induce no long-range stresses. In addition to the plastic deformation $\mathbf{F}^p$, some degree of lattice distortion $\mathbf{F}^e$ may also be expected in general. One therefore has, locally,

$$\mathbf{F} = \mathbf{F}^e\mathbf{F}^p \tag{4.27}$$

This multiplicative elastic-plastic kinematics was first suggested by Lee [69] and further developed by others ([132, 3, 51, 53, 87, 121]) within the context of ductile single crystals. The free energy density follows in the form

$$A = A(\mathbf{F}^e, \boldsymbol{\gamma}) = A(\mathbf{F}\mathbf{F}^{p-1}, \boldsymbol{\gamma}) \tag{4.28}$$

where $\boldsymbol{\gamma} \in R^N$ denotes some suitable collection of hardening variables. Thus, the complete set of internal variables is, in this case, $\mathbf{Q} = (\mathbf{F}^p, \boldsymbol{\gamma})$. Correspondingly, the complete set of thermodynamic forces is now $\mathbf{Y} = (\mathbf{T}, -\boldsymbol{\tau})$, where

$$\mathbf{T} = -A_{,\mathbf{F}^p} \qquad \boldsymbol{\tau} = A_{,\boldsymbol{\gamma}} \tag{4.29}$$

The symmetric stress measure

$$\mathbf{S} = \mathbf{F}^{eT}A_{,\mathbf{F}^e} = \mathbf{T}\mathbf{F}^{pT} \tag{4.30}$$

is also noted for subsequent reference. In the special case of metals, in which the elastic response is ostensibly independent of the plastic processes, the free energy (4.28) decomposes additively in the form

$$A = W^e(\mathbf{F}\mathbf{F}^{p-1}) + W^p(\mathbf{F}^p, \mathbf{Q}) \tag{4.31}$$

The function W^e determines the elastic response of the metal, e. g., upon unloading, whereas the function W^p describes the hardening of the material. In the presence of an inelastic potential ψ, the flow rule and rate equations follow jointly in the form

$$\dot{\mathbf{F}}^p = \psi_{,\mathbf{T}}\,(\mathbf{T}, \boldsymbol{\tau}; \mathbf{F}^p, \boldsymbol{\gamma}), \qquad \dot{\boldsymbol{\gamma}} = \psi_{,\boldsymbol{\tau}}\,(\mathbf{T}, \boldsymbol{\tau}; \mathbf{F}^p, \boldsymbol{\gamma}) \tag{4.32}$$

However, plastic deformations are often isochoric, i. e., volume preserving. A class of isochoric flow rules is obtained by letting the inelastic potential ψ be a function of $(\mathbf{S}, \boldsymbol{\tau})$, whereupon (4.32) becomes

$$\dot{\mathbf{F}}^p\mathbf{F}^{p-1} = \psi_{,\mathbf{S}}\,(\mathbf{S}, \boldsymbol{\tau}), \qquad \dot{\boldsymbol{\gamma}} = -\psi_{,\boldsymbol{\tau}}\,(\mathbf{S}, \boldsymbol{\tau}) \tag{4.33}$$

The isochoricity condition is now

$$\mathrm{tr}(\dot{\mathbf{F}}^p\mathbf{F}^{p-1}) = 0 \tag{4.34}$$

the satisfaction of which may be ensured simply by restricting the dependence of ψ on $\mathbf{S}$ to its deviatoric component $\mathbf{S}^{\mathrm{dev}}$.

As a specific example, let

$$s = \max_{(\mathbf{s},\mathbf{m})} \mathbf{S} \cdot (\mathbf{s} \otimes \mathbf{m}) \tag{4.35}$$

be the maximum shear stress acting on the material. In (4.35), the maximization is

subject to the constraints

$$\|\mathbf{s}\| = \|\mathbf{m}\| = 1, \qquad \mathbf{s} \cdot \mathbf{m} = 0 \tag{4.36}$$

The unit vectors $\mathbf{s}$ and $\mathbf{m}$ may be regarded as the instantaneous slip direction and slip-plane normal. Next assume that the material hardens isotropically, and let γ be the sole hardening parameter of the model. With (4.31) in force, let $W^p(\gamma)$ depend solely on γ. Then, the second of (4.29) reduces to

$$\tau = W^{p\prime}(\gamma) \tag{4.37}$$

In addition, assume that the inelastic potential is a function of the overstress $s - \tau$, i. e.,

$$\psi = \psi(s - \tau) \tag{4.38}$$

Then, (4.33) gives

$$\dot{\mathbf{F}}^p \mathbf{F}^{p-1} = \dot{\gamma}\mathbf{s} \otimes \mathbf{m}, \qquad \dot{\gamma} = \psi'(s - \tau) \tag{4.39}$$

which is Tresca's flow rule. Evidently, the second of (4.36) ensures plastic isochoricity, eq. (4.34). In the special case of power-law viscosity and hardening one has

$$W^p = \frac{n\tau_0\gamma_0}{n+1}\left(1 + \frac{\gamma}{\gamma_0}\right)^{(n+1)/n} \tag{4.40}$$

$$\psi = \begin{cases} \frac{\tau_0\dot{\gamma}_0}{m+1}\left(\frac{s-\tau}{\tau_0}\right)^{m+1}, & s \geq \tau; \\ 0 & \text{otherwise} \end{cases} \tag{4.41}$$

where $\dot{\gamma}_0$ is a reference shear strain rate, γ_0 is a reference shear strain, τ_0 is the shear yield stress, m is the rate-sensitivity exponent and n is the hardening exponent. An

insertion of (4.40) into (4.37) and (4.39) gives

$$\tau = \tau_0 \left(1 + \frac{\gamma}{\gamma_0}\right)^{1/n} \tag{4.42}$$

$$\dot{\gamma} = \begin{cases} \dot{\gamma}_0 \left(\frac{s-\tau}{\tau_0}\right)^m, & s \geq \tau; \\ 0 & \text{otherwise} \end{cases} \tag{4.43}$$

Clearly, in this model τ plays the role of a critical resolved shear stress.

4.3 Temporal discretization

In the remainder of this chapter we turn to the problem of approximating the solutions of the class of initial-boundary value problems just formulated. In the finite element method it is costumary to effect a *spatial* discretization first, leading to a semidiscrete system of governing equations, i. e., a system of ordinary differential equations in the time variable. Then, the semidiscrete system is discretized in *time* by recourse to a suitable time-stepping algorithm. Here, we reverse the order of the discretization, and begin by discretizing the initial-boundary value problem in time, leading to the definition of an *equivalent static problem.* A key observation is that the solutions of this equivalent static problem obey a minimum principle, provided that the constitutive update possesses a potential structure. The variational structure of the equivalent static problem is subsequently exploited for purposes of error estimation.

4.3.1 Field equations

Here and subsequently, we envision an incremental solution procedure aimed at sampling the solution at discrete times $t_0, \ldots, t_n$, $t_{n+1} = t_n + \triangle t, \ldots$. The linear-momentum balance equation (4.4) can be discretized in time by recourse to a standard multistep algorithm. For definiteness, we consider a general three-point algorithm of

the form:

$$\rho_0 \frac{\boldsymbol{\varphi}_{n+1} + \boldsymbol{\varphi}_{n-1} - 2\boldsymbol{\varphi}_n}{\triangle t^2} - (\alpha_{-1}\nabla_0 \cdot \mathbf{P}_{n-1} + \alpha_0 \nabla_0 \cdot \mathbf{P}_n + \alpha_1 \nabla_0 \cdot \mathbf{P}_{n+1}) = \rho_0(\alpha_{-1}\mathbf{B}_{n-1} + \alpha_0 \mathbf{B}_n + \alpha_1 \cdot \mathbf{B}_{n+1}) \tag{4.44}$$

where α_{-1}, α_0 and α_1 are algorithmic parameters. The consistency of the algorithm requires

$$\alpha_{-1} + \alpha_0 + \alpha_1 = 1 \tag{4.45}$$

The multistep scheme (4.44) may equivalently be restated as Newmark's algorithm:

$$\boldsymbol{\varphi}_{n+1} = \boldsymbol{\varphi}_n + \triangle t\, \dot{\boldsymbol{\varphi}}_n + \triangle t^2[(1/2 - \beta)\ddot{\boldsymbol{\varphi}}_n + \beta \ddot{\boldsymbol{\varphi}}_{n+1}] \tag{4.46}$$

$$\dot{\boldsymbol{\varphi}}_{n+1} = \dot{\boldsymbol{\varphi}}_n + \triangle t\,[(1-\gamma)\ddot{\boldsymbol{\varphi}}_n + \gamma \ddot{\boldsymbol{\varphi}}_{n+1}] \tag{4.47}$$

$$\rho_0 \ddot{\boldsymbol{\varphi}}_{n+1} - \nabla_0 \cdot \mathbf{P}_{n+1} = \rho_0 \mathbf{B}_{n+1} \tag{4.48}$$

where β and γ are Newmark's parameters. The parameters $(\alpha_{-1}, \alpha_0, \alpha_1)$ are related to (β, γ) as

$$\begin{aligned} \alpha_{-1} &= \frac{1}{2} + \beta - \gamma \\ \alpha_0 &= \frac{1}{2} - 2\beta + \gamma \\ \alpha_1 &= \beta \end{aligned} \tag{4.49}$$

It is evident from (4.45) that Newmark's algorithm is consistent for all values of (β, γ). The performance of Newmark's algorithm, including its range of stability, has been extensively documented in the literature (e. g., [11, 58]). A standard implementation of Newmark's algorithm is to eliminate $\ddot{\boldsymbol{\varphi}}_{n+1}$ from (4.46) to obtain the equivalent static problem:

$$\frac{\rho_0}{\beta \triangle t^2}\boldsymbol{\varphi}_{n+1} - \nabla_0 \cdot \mathbf{P}_{n+1} = \rho_0 \bar{\mathbf{B}}_{n+1} \tag{4.50}$$

where

$$\bar{\mathbf{B}}_{n+1} \equiv \mathbf{B}_{n+1} + \frac{1}{\beta \triangle t^2}[\boldsymbol{\varphi}_n + \triangle t\, \dot{\boldsymbol{\varphi}}_n + (1/2 - \beta)\triangle t^2 \ddot{\boldsymbol{\varphi}}_n] \tag{4.51}$$

is an effective body force field entirely defined in terms of the initial data for the time step and which accounts for the inertia of the body. It should be carefully noted that the equivalent static problem (4.50) reflects both the inertia as well as the constitution of the body.

4.3.2 Constitutive update

Finally, we address the time-integration of the constitutive equations (4.10) and (4.12). As will become apparent in subsequent discussions, it is essential for the purpose of error estimation that the resulting stress update algorithm derive from an incremental potential, or energy density, so that the incremental displacements be governed by a minimum principle. A stress update having the requisite potential structure may be obtained by integration of the constitutive relations along 'minimizing paths', i. e., along such deformation histories which minimize the incremental work of deformation. The work of deformation itself then supplies the sought strain energy potential. This approach has been used in the past to derive deformation, or pseudoelastic, theories of plasticity ([90, 86, 129, 23]). A recent application of minimizing paths to the study of dislocation structures in ductile single crystals may be found in [106]. However, the task of determining minimizing paths for specific models is often daunting, specially for rate-sensitive materials, which detracts from the practicality of the approach. Here, we give an alternative and more direct method for formulating updates possessing the requisite potential structure.

As in the foregoing, we envision an incremental solution procedure and concern ourselves with a generic time interval $[t_n, t_{n+1}]$. Since the constitutive equations (4.10) and (4.12) are local, the material coordinates $\mathbf{X}$ play the role of parameters as regards the constitutive update and, for clarity, will be omitted throughout in the discussion that follows. Let the initial state $(\mathbf{F}_n, \mathbf{Q}_n)$ and the updated deformations $\mathbf{F}_{n+1}$ be

given. Suppose that the kinetic equations and the viscosity law possess a potential structure such as expressed in eqs. (4.14) and (4.15). Furthermore, introduce the dual potential $\psi^*(\dot{\mathbf{Q}}, \mathbf{Q})$ by recourse to the Legendre transformation

$$\psi^*(\dot{\mathbf{Q}}, \mathbf{Q}) = \mathbf{Y} \cdot \dot{\mathbf{Q}} - \psi(\mathbf{Y}, \mathbf{Q}) \tag{4.52}$$

Then one has

$$\mathbf{Y} = \psi^*{}_{,\dot{\mathbf{Q}}}\,(\dot{\mathbf{Q}}, \mathbf{Q}) \tag{4.53}$$

which constitutes a restatement of the kinetic equations (4.14). Finally, define the incremental energy density as

$$\begin{aligned} W(\mathbf{F}_{n+1}; \mathbf{F}_n, \mathbf{Q}_n) &= \triangle t \phi \left(\frac{\mathbf{F}_{n+1} - \mathbf{F}_n}{\triangle t}; \mathbf{F}_n \right) + \\ \min_{\mathbf{Q}_{n+1}} &\left\{ A(\mathbf{F}_{n+1}, \mathbf{Q}_{n+1}) - A(\mathbf{F}_n, \mathbf{Q}_n) + \triangle t \psi^* \left(\frac{\mathbf{Q}_{n+1} - \mathbf{Q}_n}{\triangle t}, \mathbf{Q}_n \right) \right\} \end{aligned} \tag{4.54}$$

Minimization with respect to $\mathbf{Q}_{n+1}$ gives the condition

$$\mathbf{Y}_{n+1} = \psi^*{}_{,\dot{\mathbf{Q}}} \left(\frac{\mathbf{Q}_{n+1} - \mathbf{Q}_n}{\triangle t}, \mathbf{Q}_n \right) \tag{4.55}$$

in accordance with (4.53). Imagine now perturbing $\mathbf{F}_{n+1} \rightarrow \mathbf{F}_{n+1} + \delta\mathbf{F}_{n+1}$. The corresponding variation of W is

$$\begin{aligned} \delta W = \quad & \left\{ A_{,\mathbf{F}}\,(\mathbf{F}_{n+1}, \mathbf{Q}_{n+1}) + \mathbf{P}^v \left(\frac{\mathbf{F}_{n+1} - \mathbf{F}_n}{\triangle t}; \mathbf{F}_n \right) \right\} \cdot \delta\mathbf{F}_{n+1} \\ - \quad & \left\{ \mathbf{Y}_{n+1} - \psi^*{}_{,\dot{\mathbf{Q}}} \left(\frac{\mathbf{Q}_{n+1} - \mathbf{Q}_n}{\triangle t}, \mathbf{Q}_n \right) \right\} \cdot \delta\mathbf{Q}_{n+1} \end{aligned} \tag{4.56}$$

But the last term in this identity vanishes by virtue of the stationarity condition (4.55), with the result

$$\delta W = \left\{ A_{,\mathbf{F}}\,(\mathbf{F}_{n+1}, \mathbf{Q}_{n+1}) + \mathbf{P}^v \left(\frac{\mathbf{F}_{n+1} - \mathbf{F}_n}{\triangle t}; \mathbf{F}_n \right) \right\} \cdot \delta\mathbf{F}_{n+1} \tag{4.57}$$

Using (4.10) to write

$$\mathbf{P}_{n+1} = A_{,\mathbf{F}}\left(\mathbf{F}_{n+1}, \mathbf{Q}_{n+1}\right) + \mathbf{P}^{v}\left(\frac{\mathbf{F}_{n+1} - \mathbf{F}_{n}}{\triangle t}; \mathbf{F}_{n}\right) \tag{4.58}$$

eq. (4.57) reduces to

$$\delta W = \mathbf{P}_{n+1} \cdot \delta \mathbf{F}_{n+1} \tag{4.59}$$

But, since $\delta \mathbf{F}_{n+1}$ is arbitrary, this identity implies that

$$\mathbf{P}_{n+1} = W_{,\mathbf{F}_{n+1}}\left(\mathbf{F}_{n+1}; \mathbf{F}_{n}, \mathbf{Q}_{n}\right) \tag{4.60}$$

Eqs. (4.58), or, equivalently, (4.60), furnishes the sought stress update. In particular, we verify that W indeed acts as a potential for $\mathbf{P}_{n+1}$, as desired. The consistency of the stress-update algorithm with the constitutive relations follows simply by taking the limit $\triangle t \to 0$ in (4.55) and (4.58), with the result

$$\mathbf{Y}_{n} = \psi^{*}{}_{,\dot{\mathbf{Q}}}\left(\dot{\mathbf{Q}}_{n}, \mathbf{Q}_{n}\right); \qquad \mathbf{P}_{n} = A_{,\mathbf{F}}\left(\mathbf{F}_{n}, \mathbf{Q}_{n}\right) + \mathbf{P}^{v}(\dot{\mathbf{F}}_{n}; \mathbf{F}_{n}) \tag{4.61}$$

in accordance with (4.53) and (4.10), respectively.

A distinct advantage of stress updates possessing a potential structure, such as just formulated, is that the tangent moduli $\partial \mathbf{P}_{n+1}/\partial \mathbf{F}_{n+1}$ are symmetric, which in turn results in symmetric tangent stiffness matrices upon finite element discretization. The existence of a symmetric and coercive Dirichlet form, leading to error estimates in the energy norm, is, as we shall see, directly related to the convexity properties of the incremental strain energy density $W(\mathbf{F}_{n+1}; \mathbf{F}_{n}, \mathbf{Q}_{n})$. An example of a nonconvex W in the theory of ductile single crystals, leading to the formation of dislocation structures, has been given by Ortiz and Repetto [106]. A somewhat more general formulation than developed in the foregoing has been given by Ortiz and Stainier [106], where additional examples of application and numerical tests may also be found.

By way of illustration, we close this section by applying the constitutive updates

just formulated to the examples of materials discussed in Section 4.2.2.

Hyperelastic solids

In the case of a hyperelastic solid, the incremental energy density (4.54) reduces to

$$W = A(\mathbf{F}_{n+1}) - A(\mathbf{F}_n) \tag{4.62}$$

Thus, W and A coincide modulo an inconsequential constant. Likewise, the stress update reduces to

$$\mathbf{P}_{n+1} = A_{,\mathbf{F}}\left(\mathbf{F}_{n+1}\right) \tag{4.63}$$

which amounts simply to the evaluation of the stress-strain relations at time t_{n+1}.

Newtonian fluids

For a Newtonian fluid, the incremental energy density (4.54) specializes to

$$W = A(J_{n+1}) - A(J_n) + \triangle t\phi\left(\frac{\mathbf{F}_{n+1} - \mathbf{F}_n}{\triangle t}; \mathbf{F}_n\right) \tag{4.64}$$

where ϕ is given by (4.24). A revealing form of (4.64) may be obtained as follows. Let

$$\mathbf{u} = \boldsymbol{\varphi}_{n+1} - \boldsymbol{\varphi}_n \tag{4.65}$$

be the incremental displacements,

$$\nabla_n \mathbf{u} = \mathbf{F}_{n+1}\mathbf{F}_n^{-1} - \mathbf{I} \tag{4.66}$$

the displacement gradients on configuration B_n, and

$$\nabla_n^S \mathbf{u} = \mathrm{sym}(\nabla_n \mathbf{u}) \tag{4.67}$$

the corresponding symmetric gradient operator. Then (4.64) may be rewritten in the form

$$W = A(J_{n+1}) - A(J_n) + \frac{\eta}{\triangle t} J_n (\nabla_n^S \mathbf{u})^{\mathrm{dev}} \cdot (\nabla_n^S \mathbf{u})^{\mathrm{dev}} \tag{4.68}$$

We further note that the updated Jacobian of the deformation may be expressed in terms of the incremental displacements as

$$J_{n+1} = \det(\mathbf{I} + \nabla_n \mathbf{u}) J_n \tag{4.69}$$

It therefore follows that, within the present framework, the incremental problem is identical to that of an elastic material treated within the linearized kinematics approximation. Furthermore, the deviatoric response of this equivalent elastic material is linear with shear modulus $\mu = \eta/\triangle t$. In the limit of an incompressible fluid, the hydrostatic pressure becomes a Lagrange multiplier, and the incremental displacements $\mathbf{u}$ follow from a *linear* problem. By contrast, the pressure follows from the nonlinear constraint

$$J_{n+1} = 1 \tag{4.70}$$

As noted by Ball, [7], the energy density is necessarily nonconvex under conditions of near-incompressibility. However, the incremental energy density can be regularized locally by decreasing the time step $\triangle t$ sufficiently, or, equivalently, by increasing the viscosity. Consider, by way of example, the free energy density

$$A(J) = \frac{1}{2\epsilon} \log^2 J.$$

Evidently, the incompressible limit is attained by letting $\epsilon \to 0^+$. Then, in the two-dimensional case (4.68) reduces to

$$W = \frac{1}{\epsilon} \log^2(\lambda_1 \lambda_2) + \frac{\eta}{3\triangle t} \left(1 - \lambda_1 - \lambda_2 + \lambda_1^2 - \lambda_1 \lambda_2 + \lambda_2^2\right)$$

where λ_1, λ_2 are the principal stretches. Fig. 4.1 shows contour and surface plots of W for two different sets of parameters $\{\epsilon, \eta, \triangle t\}$. For the first set of parameters, corresponding to a low viscosity or a large time step, W is nonconvex, as is evident from the 'banana'-shape level contours [7]. By contrast, for the second set of parameters, corresponding to a high viscosity or a small time step, the incremental energy density may be made to be locally convex. Indeed, a straightforward calculation reveals that the hessian of W is positive definite at (λ_1, λ_2) provided that

$$\frac{\triangle t}{\eta} \leq \frac{\epsilon}{3} \frac{\lambda_1^2 \lambda_2^2}{(\lambda_1 + \lambda_2)^2 - (\lambda_1^2 + \lambda_2^2) \log(\lambda_1 \lambda_2)} \tag{4.71}$$

Viscoplastic solids

For a viscoplastic solid, the incremental energy density (4.54) reduces to

$$W(\mathbf{F}_{n+1}; \mathbf{F}_n, \mathbf{Q}_n) = \min_{\mathbf{F}^p_{n+1}, \boldsymbol{\gamma}_{n+1}} \left\{ A(\mathbf{F}_{n+1}\mathbf{F}^{p-1}_{n+1}, \boldsymbol{\gamma}_{n+1}) - A(\mathbf{F}_n \mathbf{F}^{p-1}_n, \boldsymbol{\gamma}_n) + \triangle t \psi^* \left(\frac{\mathbf{Q}_{n+1} - \mathbf{Q}_n}{\triangle t}, \mathbf{Q}_n \right) \right\} \tag{4.72}$$

For the specific example of a power-law isotropic hardening, power-law rate-sensitive Tresca material developed in Section 4.2.2, the incremental strain energy density takes the form

$$W(\mathbf{F}_{n+1}; \mathbf{F}_n, \mathbf{Q}_n) = \min_{\mathbf{s}, \mathbf{m}, \gamma_{n+1}} \left\{ A(\mathbf{F}_{n+1}\mathbf{F}^{p-1}_{n+1}, \gamma_{n+1}) - A(\mathbf{F}_n \mathbf{F}^{p-1}_n, \gamma_n) + \triangle t \psi^* \left(\frac{\triangle \gamma}{\triangle t} \right) \right\} \tag{4.73}$$

where the minimization with respect to $\mathbf{s}$ and $\mathbf{m}$ is subject to constraints (4.36). Additionally, we have written $\triangle \gamma = \gamma_{n+1} - \gamma_n$, and

$$\mathbf{F}^p_{n+1} = (\mathbf{I} + \triangle \gamma \mathbf{s} \otimes \mathbf{m}) \mathbf{F}^p_n \tag{4.74}$$

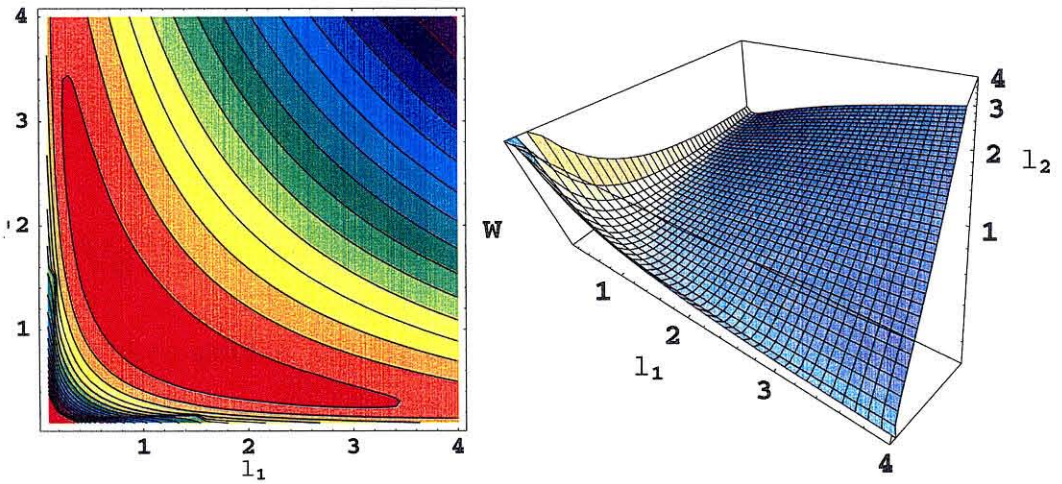

(a) $\eta = 1$, $\epsilon = 10^{-4}$ and $\triangle t = 10^{-3}$, breakdown of quasiconvexity

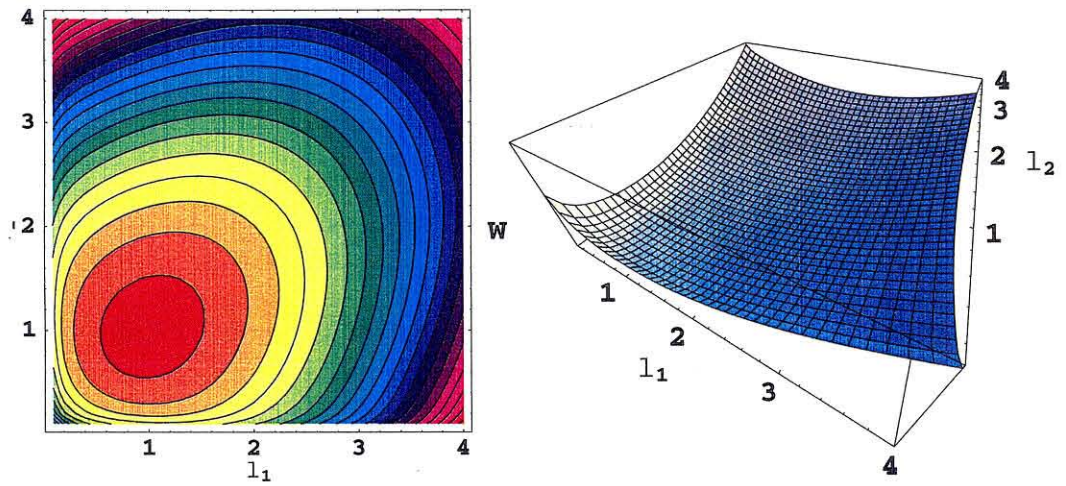

(b) $\eta = 1$, $\epsilon = 10^{-4}$ and $\triangle t = 10^{-5}$, regularization by choice of suitably small $\triangle t$

Figure 4.1: Contour levels and surface plots of incremental energy density for a near-incompressible viscous fluid

It should be noted that this update preserves the isochoricity of $\mathbf{F}^p$ exactly since, by the second of (4.36), the tensor $(\mathbf{I} + \triangle\gamma \mathbf{s} \otimes \mathbf{m})$ is unimodular. Finally, the dual inelastic potential for this example is

$$\psi^* = \frac{m\tau_0\dot{\gamma}_0}{m+1}\left(\frac{\dot{\gamma}}{\dot{\gamma}_0}\right)^{(m+1)/m} \tag{4.75}$$

which completes the definition of W.

4.4 Variational structure

In the sequel we assume that the constitutive update possesses a potential structure and derives from an incremental energy density $W(\mathbf{F}_{n+1}; \mathbf{F}_n, \mathbf{Q}_n)$. The existence–and practicality–of such algorithms has been established in the preceding section for a wide class of materials. Next we show that, under these conditions, the solutions of the equivalent static problem (4.50) obey a minimum principle. To see this, introduce the potential energy:

$$\Phi[\boldsymbol{\varphi}_{n+1}] = \int_{B_0}\left[\frac{1}{2}\frac{\rho_0}{\beta\triangle t^2}|\boldsymbol{\varphi}_{n+1}|^2 + W(\nabla_0\boldsymbol{\varphi}_{n+1}; \mathbf{F}_n, \mathbf{Q}_n)\right] dV_0 \tag{4.76}$$

$$- \int_{B_0}\rho_0\bar{\mathbf{B}}_{n+1}\cdot\boldsymbol{\varphi}_{n+1}dV_0 - \int_{\partial B_{02}}\bar{\mathbf{T}}_{n+1}\cdot\boldsymbol{\varphi}_{n+1}dS_0 \tag{4.77}$$

Then $\boldsymbol{\varphi}_{n+1}$ follows from the variational problem:

$$\Phi[\boldsymbol{\varphi}_{n+1}] = \inf_{\boldsymbol{\eta}\in V}\Phi[\boldsymbol{\eta}] \tag{4.78}$$

where V is the space of deformation mappings in $W^{1,\infty}(B_0; \mathbb{R}^d)$ satisfying the essential boundary conditions (4.6) (in the sense of trace). It is readily verified that (4.50) are indeed the Euler-Lagrange equations of (4.77). In writing (4.78) as a *minimum* principle, we are tacitly identifying the *stable* solutions of the problem with the weak relative minima of Φ. We recall that $\boldsymbol{\varphi}_{n+1}$ is a weak relative minima of Φ if there exists $\delta > 0$ such that $\Phi[\boldsymbol{\eta}]$ exists and $\Phi[\boldsymbol{\eta}] \geq \Phi[\boldsymbol{\varphi}_{n+1}]$ for all $\boldsymbol{\eta} \in V$ such that

$\|\boldsymbol{\eta} - \boldsymbol{\varphi}_{n+1}\|_V < \delta$.

Consider now a pair of incremental displacements $\mathbf{u}$ and $\mathbf{v}$ applied to the deformed configuration B_{n+1} satisfying homogeneous essential boundary conditions over ∂B_{10}. We then define the Dirichlet form of the problem as the second variation of the potential energy Φ at $\boldsymbol{\varphi}_{n+1}$, i. e.,

$$a[\boldsymbol{\varphi}_{n+1}](\mathbf{u},\mathbf{v}) = \delta^2\Phi[\boldsymbol{\varphi}_{n+1}](\mathbf{u},\mathbf{v})$$
$$= \int_{B_0}\left[\frac{\rho_0}{\beta\triangle t^2}\mathbf{u}\cdot\mathbf{v} + W_{,\mathbf{F}_{n+1}\mathbf{F}_{n+1}}(\nabla_0\boldsymbol{\varphi}_{n+1};\mathbf{F}_n,\mathbf{Q}_n)\cdot(\nabla_0\mathbf{u}\otimes\nabla_0\mathbf{v})\right]dV_0 \quad (4.79)$$

which, evidently, is symmetric. Thus, the variational structure of the problem ensures the existence of a symmetric Dirichlet form. We further recall from the classical calculus of variations that if W is C^2 and $\boldsymbol{\varphi}_{n+1} \in C^1(B_0;\mathbb{R}^d)$ is a solution of the Euler-Lagrange equations (4.50) for Φ, then a sufficient condition for $\boldsymbol{\varphi}_{n+1}$ to be a weak relative minimum of Φ is that

$$a[\boldsymbol{\varphi}_{n+1}](\mathbf{u},\mathbf{u}) \geq C\|\mathbf{u}\|_1^2 \quad (4.80)$$

for some constant C and all $\mathbf{u} \in W^{1,2}(B_0;\mathbb{R}^d)$ satisfying homogeneous essential boundary conditions over ∂B_{10} [133, 9]. In the sequel, we shall confine our attention to solutions $\boldsymbol{\varphi}_{n+1}$ for which (4.80) holds. It is clear from the form of (4.79) that the inertia term has a stabilizing effect for small time steps, in as much as it tends to shift the eigenspectrum towards the positive axis. The stabilizing effect of viscosity has been discussed in Section 4.3.2. Friesecke and Dolzmann have shown that certain forms of linear viscosity regularize the problem and render the effective time-discretized energy density quasiconvex for sufficiently small time steps. All these observations suggest that, as a practical matter, the combination of inertia, viscosity and small time steps may in many cases suffice to ensure the satisfaction of the coercivity condition (4.80). The stabilizing effect of viscosity and inertia in solids undergoing localization has been studied numerically by Needleman [100].

4.5 Spatial discretization

Next, we take the minimum principle (4.78) for the equivalent static problem as a basis for a finite element spatial discretization. We suppose that, as a consequence of remeshing, the reference configuration B_0 is discretized into different meshes $\mathcal{T}_n$ and $\mathcal{T}_{n+1}$ at times t_n and $t_n + 1$, respectively. As a specific remeshing strategy, the new mesh $\mathcal{T}_{n+1}$–on which the as yet unknown solution at time t_{n+1} is to be computed–can be constructed based on error indicators corresponding to the solution at time t_n. In this approach, the sequence of operations is therefore: i) given $\mathcal{T}_n$ compute the solution at t_n; ii) based on the solution at t_n construct $\mathcal{T}_{n+1}$; iii) reset $n \to n+1$ and go to (i). This and similar approaches lead to an incremental problem in which the initial conditions at time t_n are interpolated on one mesh $\mathcal{T}_n$, whereas the updated solution at time t_{n+1} is interpolated on a *different* mesh $\mathcal{T}_{n+1}$. This distinction is significant in dynamic problems and in problems involving history-dependent materials, which result in a dependence of the updated solution on the initial conditions at time t_n. As we shall see, the variational principle (4.78) furnishes a precise recipe for computing on two meshes in the manner just described. In particular, it results in specific forms of mesh-to-mesh transfer operators for nodal and state data.

For definiteness, we envision a finite element interpolation of the form:

$$\boldsymbol{\varphi}_{h,n}(\mathbf{X}) = \sum_{a=1}^{N_n} \mathbf{x}_{a,n} N_{a,n}(\mathbf{X}) \tag{4.81}$$

$$\mathbf{Q}_{h,n}(\mathbf{X}) = \sum_{e=1}^{E_n} \sum_{q=1}^{Q} \mathbf{Q}^e_{q,n} M^e_{q,n}(\mathbf{X}) \tag{4.82}$$

where $\boldsymbol{\varphi}_{h,n}$ is the displacement interpolant at t_n; $\mathbf{Q}_{h,n}$ is the state variable interpolant at t_n; $N_{a,n}$ and $M^e_{q,n}$ are the displacement and state-variable shape functions corresponding to mesh $\mathcal{T}_n$, respectively; the sum on a ranges over the N_n nodes of $\mathcal{T}_n$; the sum on e ranges over the E_n elements of $\mathcal{T}_n$; and the sum over q ranges over the Q quadrature points in element e. The shape functions $N_{a,n}$ must be conforming so that $\boldsymbol{\varphi}_{h,n} \in V$. By contrast, the state-variable interpolation need only ensure that $\mathbf{Q}_{h,n}$

be in $L^\infty(B_0;\mathbb{R}^d)$ and, consequently, the shape functions $M^e_{q,n}$ can be chosen to be piecewise polynomials. Again for definiteness, assume that the shape functions $M^e_{q,n}$ satisfy the normalization condition

$$M^e_{p,n}(\Xi^e_{q,n}) = \delta_{pq} \tag{4.83}$$

where $\Xi^e_{q,n}$ are the quadrature points in element e of $\mathcal{T}_n$. A more general approach in which the deformation gradients and stresses are interpolated as in (4.82), and the constitutive and compatibility conditions are enforced weakly *a la* Hu-Washizu, has been proposed by Ortiz and Quigley [105].

Inserting the interpolation (4.81) and (4.82) into (4.78) and rendering the resulting discrete potential energy stationary leads, after some straightforward manipulations, to the system of nonlinear algebraic equations:

$$\mathbf{x}_{n+1} = \mathbf{T}\mathbf{x}_n + \triangle t\,\mathbf{T}\dot{\mathbf{x}}_n + \triangle t^2[(1/2-\beta)\mathbf{T}\ddot{\mathbf{x}}_n + \beta\ddot{\mathbf{x}}_{n+1}] \tag{4.84}$$

$$\dot{\mathbf{x}}_{n+1} = \mathbf{T}\dot{\mathbf{x}}_n + \triangle t\,[(1-\gamma)\mathbf{T}\ddot{\mathbf{x}}_n + \gamma\ddot{\mathbf{x}}_{n+1}] \tag{4.85}$$

$$\mathbf{M}_{n+1}\ddot{\mathbf{x}}_{n+1} + \mathbf{f}^{\text{int}}(\mathbf{x}_{n+1}) = \mathbf{f}^{\text{ext}}_{n+1} \tag{4.86}$$

where $\mathbf{x}$, $\dot{\mathbf{x}}$ and $\ddot{\mathbf{x}}$ are the array of nodal values of $\boldsymbol{\varphi}_h$, $\dot{\boldsymbol{\varphi}}_h$ and $\ddot{\boldsymbol{\varphi}}_h$, and

$$\mathbf{M}_{n+1} = \int_{B_0} \rho_0 \mathbf{N}_{n+1}\cdot\mathbf{N}_{n+1}dV_0 \tag{4.87}$$

$$\mathbf{f}^{\text{int}} = \int_{B_0} W_{,\mathbf{F}_{n+1}}(\mathbf{F}_{h,n+1};\mathbf{T}\mathbf{F}_{h,n},\mathbf{T}\mathbf{Q}_{h,n})\cdot\nabla_0\mathbf{N}_{n+1}dV_0 \tag{4.88}$$

$$\mathbf{f}^{\text{ext}}(\mathbf{x}_{n+1}) = \int_{B_0} \rho_0\mathbf{B}_{n+1}\cdot\mathbf{N}_{n+1}dV_0 \tag{4.89}$$

are the mass matrix, internal and external force arrays over $\mathcal{T}_{n+1}$, respectively. In these expressions, we have collected all the nodal shape functions in an array of the form $\mathbf{N} = \{\mathbf{I}N_a, a = 1,\ldots,N\}$, where $\mathbf{I}$ signifies the identity matrix, and the integrals are to be carried out by numerical quadrature.

Of particular interest in eqs. (4.84 - 4.86) are the transfer operators $\mathbf{T}$ applied to the initial data. Within the present interpolation scheme, the precise form of these

transfer operators is

$$\mathbf{T}\mathbf{x}_n = \left[\mathbf{M}_{n+1}^{-1}\int_{B_0}\rho_0\mathbf{N}_{n+1}\cdot\mathbf{N}_n dV_0\right]\mathbf{x}_n \tag{4.90}$$

$$\mathbf{T}\dot{\mathbf{x}}_n = \left[\mathbf{M}_{n+1}^{-1}\int_{B_0}\rho_0\mathbf{N}_{n+1}\cdot\mathbf{N}_n dV_0\right]\dot{\mathbf{x}}_n \tag{4.91}$$

$$\mathbf{T}\ddot{\mathbf{x}}_n = \left[\mathbf{M}_{n+1}^{-1}\int_{B_0}\rho_0\mathbf{N}_{n+1}\cdot\mathbf{N}_n dV_0\right]\ddot{\mathbf{x}}_n \tag{4.92}$$

$$\mathbf{T}\mathbf{F}_{h,n} = \sum_{e=1}^{E_{n+1}}\sum_{q=1}^{Q}\mathbf{F}_{h,n}(\Xi_{q,n+1}^e)M_{q,n+1}^e \tag{4.93}$$

$$\mathbf{T}\mathbf{Q}_{h,n} = \sum_{e=1}^{E_{n+1}}\sum_{q=1}^{Q}\mathbf{Q}_{h,n}(\Xi_{q,n+1}^e)M_{q,n+1}^e \tag{4.94}$$

It follows from these identities and (4.83) that all transfer operators reduce to the identity if $\mathcal{T}_{n+1} = \mathcal{T}_n$, as required. The transfer operator for displacements, velocities and accelerations is a mass-weighted L^2-projection from $\mathcal{T}_n$ to $\mathcal{T}_{n+1}$. The transfer operator for the state variables is a simple extrapolation from the quadrature points in $\mathcal{T}_n$ to the quadrature points in $\mathcal{T}_{n+1}$.

It is interesting to note that, by recourse of mass lumping, the mesh-to-mesh transfer operator for nodal fields, eqs. (4.90-4.92), reduces simply to a direct evaluation of the fields, as interpolated on the old mesh $\mathcal{T}_n$, at the nodes in the new mesh $\mathcal{T}_{n+1}$. Likewise, the transfer of the state variables, eqs. (4.93-4.94), amounts simply to an extrapolation from the quadrature points in $\mathcal{T}_n$ to the quadrature points in $\mathcal{T}_{n+1}$.

In the numerical tests discussed subsequently, the state variables are assumed to be piecewise constant over the Voronoi cells attendant to the quadrature points. Thus, $M_{q,n}^e$ is the characteristic function of the Voronoi cell containing the qth quadrature point in element e of $\mathcal{T}_n$. Under these conditions, the state variable transfer simply assigns to each new quadrature point on $\mathcal{T}_{n+1}$ the complete collection of state variables at the nearest old quadrature point on $\mathcal{T}_n$. Fast search algorithms and specialized data structures based on nodal octrees and mesh adjacency graphs may be utilized to minimize the complexity of the transfer algorithm (cf. Chapter 2 and also [115]).

The overriding advantage of piecewise constant representation for the state vari-

ables, and the resulting transfer operator, is that whole collections of state variables attendant are transferred from quadrature point to quadrature point as blocks, thus preserving all internal constraints and the compatibility between the various state variables. These requirements may be violated by transfer operators which involve extrapolation from several quadrature points. Thus, for instance, in the context of isochoric plasticity, eq. (4.34), the plastic part of the deformation gradient $\mathbf{F}^p$ must have a determinant of 1. This nonlinear constraint is preserved by the piecewise constant transfer operator, but is violated upon extrapolation in general. Likewise, in the context of ideal plasticity, stresses transferred in accordance with the piecewise constant transfer operator, unlike extrapolated stresses, are guaranteed to satisfy the yield conditions.

It bears emphasis that these transfer operators are not formulated arbitrarily but, as noted by Ortiz and Quigley [105], follow uniquely and unambiguously from the variational principle once the displacement and state-variable interpolation has been specified. Thus, the variational principle (4.78), or any other variational principle to suit different applications as the case may be, consistently governs all aspects of the computations, including the appropriate form of the mesh-to-mesh transfer operators.

4.6 Error estimation

The preceding developments provide a suitable framework for error estimation and mesh adaption. We adopt a 'fine-mesh' viewpoint and confine our efforts to optimizing fine meshes leading to high-quality finite element approximations. Mathematically, this focus gives us license to investigate the behavior of the finite element solutions *asymptotically* as the mesh size $h \to 0$. Throughout this section, we concern ourselves with the finite element solution at a fixed time, e. g., time t_n, and we shall omit the corresponding label n for clarity.

The Euler-Lagrange equations corresponding to the variational problem (4.78)

take the form

$$\langle D\Phi[\boldsymbol{\varphi}], \mathbf{v}\rangle \equiv \left\{ \frac{d}{d\epsilon}\Phi[\boldsymbol{\varphi} + \epsilon\mathbf{v}] \right\}_{\epsilon=0^+} = 0 \tag{4.95}$$

for all $\mathbf{v} \in V$ satisfying homogeneous boundary conditions on ∂B_{01}. Similarly the finite element solution satisfies the stationarity condition

$$\langle D\Phi[\boldsymbol{\varphi}_h], \mathbf{v}_h\rangle = 0 \tag{4.96}$$

for all $\mathbf{v}_h \in V_h$ satisfying homogeneous boundary conditions on ∂B_{01}. Choosing $\mathbf{v} = \mathbf{v}_h$ in (4.95) and subtracting gives

$$\langle D\Phi[\boldsymbol{\varphi}_h] - D\Phi[\boldsymbol{\varphi}], \mathbf{v}_h\rangle = 0 \tag{4.97}$$

But, in the asymptotic regime of interest, $\boldsymbol{\varphi}_h$ may be expected to be close to $\boldsymbol{\varphi}$, and, to leading order as $h \to 0$, (4.97) becomes

$$a[\boldsymbol{\varphi}](\boldsymbol{\varphi}_h - \boldsymbol{\varphi}, \mathbf{v}_h) = 0 \tag{4.98}$$

where a is the Dirichlet form (4.79). Identity (4.98) expresses the orthogonality of the error function $\boldsymbol{\varphi}_h - \boldsymbol{\varphi}$ and V_h in the Dirichlet form at $\boldsymbol{\varphi}$ asymptotically as $h \to 0$. It also shows that the finite element solution $\boldsymbol{\varphi}_h$ possesses the 'best-approximation' property, namely,

$$\|\boldsymbol{\varphi}_h - \boldsymbol{\varphi}\|_E = \min_{\boldsymbol{\eta}_h \in V_h} \|\boldsymbol{\eta}_h - \boldsymbol{\varphi}\|_E \tag{4.99}$$

where

$$\|\mathbf{u}\|_E = \sqrt{a[\boldsymbol{\varphi}](\mathbf{u}, \mathbf{u})} \tag{4.100}$$

is the energy norm at $\boldsymbol{\varphi}$.

At this point, we have reached a standard situation. Indeed, as it is well-known

(*cf.* [29]), the best-approximation property (4.99) and the coercivity assumption (4.80) give the error bound:

$$\|\boldsymbol{\varphi}_h - \boldsymbol{\varphi}\|_1 \leq C \sum_{e=1}^{E} (h^e)^k |\boldsymbol{\varphi}^e|_{k+1} \tag{4.101}$$

where k is the order of polynomial interpolation, $|\cdot|_{k+1}$ is the Sobolev H^{k+1}-seminorm, $\boldsymbol{\varphi}^e$ is the restriction of $\boldsymbol{\varphi}$ to the domain Ω_0^e of finite element e, h^e is the size of element e and we assume regular refinement and a lower bound for the aspect ratio of all elements. Evidently, in (4.101) the terms $(h^e)^k$ account for the dependence of the error to the element size, and $|\boldsymbol{\varphi}^e|_{k+1}$ furnishes a measure of the variation of the exact solution over element e.

The problem of mesh adaption may now be identified with that of minimizing the bound (4.101), e. g., for a fixed number of elements E. To make analytical progress, we begin by noting the equivalent bound

$$\|\boldsymbol{\varphi}_h - \boldsymbol{\varphi}\|_1^2 \leq C \sum_{e=1}^{E} (h^e)^{2k} |\boldsymbol{\varphi}^e|_{k+1}^2 \tag{4.102}$$

Explicating the seminorms gives

$$\|\boldsymbol{\varphi}_h - \boldsymbol{\varphi}\|_1^2 \leq C \sum_{e=1}^{E} (h^e)^{2k} \left(\sum_{|\alpha|=k+1} \int_{\Omega_0^e} |D^\alpha \boldsymbol{\varphi}^e|^2 dV_0 \right) \tag{4.103}$$

In order to obtain a continuous–rather than a discrete–optimization problem, we introduce an element-size distribution function $h(\mathbf{X})$ giving the target element size at all points $\mathbf{X}$ in B_0, and approximate (4.103) as

$$\begin{aligned} \|\boldsymbol{\varphi}_h - \boldsymbol{\varphi}\|_1^2 &\leq C \sum_{e=1}^{E} \int_{\Omega_0^e} (h^e)^{2k} \left(\sum_{|\alpha|=k+1} |D^\alpha \boldsymbol{\varphi}^e|^2 \right) dV_0 \\ &\approx C \int_{B_0} h^{2k} \left(\sum_{|\alpha|=k+1} |D^\alpha \boldsymbol{\varphi}|^2 \right) dV_0 \end{aligned} \tag{4.104}$$

On the other hand, the number of elements in the mesh is of the order of

$$E \sim \int_{B_0} h^{-d} dV_0 \tag{4.105}$$

Consequently, the optimal mesh-size distribution for a fixed number of elements follows from the problem:

$$\text{minimize} \int_{B_0} \left\{ h^{2k} \left(\sum_{|\alpha|=k+1} |D^\alpha \boldsymbol{\varphi}|^2 \right) + \lambda h^{-d} \right\} dV_0 \tag{4.106}$$

where λ is a Lagrange multiplier. The solution of this problem is

$$h(\mathbf{X}) = A \left(\sum_{|\alpha|=k+1} |D^\alpha \boldsymbol{\varphi}(\mathbf{X})|^2 \right)^{-1/(2k+d)} \tag{4.107}$$

where the constant A follows from the constraint (4.105) as

$$A = \left[\frac{1}{E} \int_{B_0} \left(\sum_{|\alpha|=k+1} |D^\alpha \boldsymbol{\varphi}(\mathbf{X})|^2 \right)^{d/(2k+d)} dV_0 \right]^{1/d} \tag{4.108}$$

which, in conjunction with (4.107), give the sought optimal mesh-size distribution over B_0.

There are at least two practical problems with (4.107): i) $h(\mathbf{X})$ is given in terms of the unknown exact solution $\boldsymbol{\varphi}$; and ii) it is not possible to simply replace $\boldsymbol{\varphi}^e$ by $\boldsymbol{\varphi}_h^e$ as this latter function is a polynomial of degree k and, consequently, $D^\alpha \boldsymbol{\varphi}_h^e = 0$ when $|\alpha| = k+1$. A number of schemes have been devised to estimate derivatives of order $k+1$ of $\boldsymbol{\varphi}_h$ (e. g., [36, 35, 144]). Inevitably, these schemes entail awkward smoothing and extrapolation steps connecting the finite element solution over several adjacent elements. These procedures often lack a theoretical basis and are *ad hoc* at best.

Next we propose a simpler–and more rigorous–approach which leads to purely local *a posteriori* error estimates. Assume that $k \geq 2$ and $\tilde{\boldsymbol{\varphi}}_h$ be the $(k-1)$-interpolant of $\boldsymbol{\varphi}_h$, Fig. 4.2. The method consists of estimating–and optimizing the mesh so as to

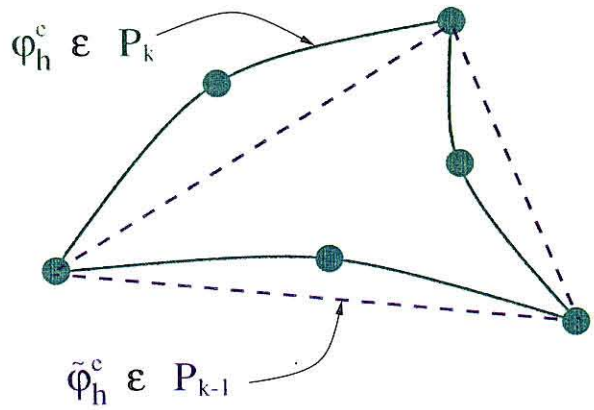

Figure 4.2: $(k-1)$-interpolant of φ_h

minimize–the error in $\tilde{\varphi}_h$, as opposed to the error in the finite element solution φ_h itself. Begin by noting that, by the triangular inequality,

$$\|\tilde{\varphi}_h - \varphi\|_1 = \|(\tilde{\varphi}_h - \varphi_h) + (\varphi_h - \varphi)\|_1 \leq \|\tilde{\varphi}_h - \varphi_h\|_1 + \|\varphi_h - \varphi\|_1 \tag{4.109}$$

But, asymptotically as $h \to 0$, the first term in the right-hand side is of order $O(h^{k-1})$, whereas the second term is of order $O(h^k)$. Consequently, the first term dominates asymptotically with the result that

$$\|\tilde{\varphi}_h - \varphi\|_1 \leq C\|\tilde{\varphi}_h - \varphi_h\|_1 \tag{4.110}$$

for some constant C, asymptotically as $h \to 0$. An application of the error bound (4.101) to the right-hand side of (4.110) then gives

$$\|\tilde{\varphi}_h - \varphi\|_1 \leq C \sum_{e=1}^{E} (h^e)^{k-1} |\varphi_h^e|_k \tag{4.111}$$

asymptotically as $h \to 0$.

A careful examination of (4.111) reveals that two key improvements have been obtained over conventional error estimates: i) we have rigorously replaced φ by φ_h in the error bound, rendering the method truly 'a posteriori'; and ii) we have obtained

an error estimate involving derivatives of order k of φ_h^e, which are well defined. In particular, an optimization of the bound in (4.111)–by exactly the same means leading to (4.107)–now gives

$$h(\mathbf{X}) = A \left(\sum_{|\alpha|=k} |D^\alpha \varphi_h(\mathbf{X})|^2 \right)^{-1/(2(k-1)+d)} \tag{4.112}$$

and

$$A = \left[\frac{1}{E} \int_{B_0} \left(\sum_{|\alpha|=k} |D^\alpha \varphi_h(\mathbf{X})|^2 \right)^{d/(2(k-1)+d)} dV_0 \right]^{1/d} \tag{4.113}$$

Again we emphasize that the target mesh size distribution (4.112) is now defined in terms of purely local elementwise indicators requiring only the evaluation of the kth-order derivatives of the local finite element solution, which greatly facilitates the application of the method.

In lagrangian simulations of unconstrained flows, the deformation mapping φ may become extremely convoluted and mesh adaption over the undeformed configuration, such as just described, may lead to unacceptable mesh distortion over the deformed configuration. In order to sidestep this difficulty, the roles of the undeformed and deformed configurations may be exchanged, and error estimation may be performed on the inverse deformation mapping φ^{-1}. This leads to the error estimate:

$$\|\tilde{\varphi}_h^{-1} - \varphi^{-1}\|_1 \leq C \sum_{e=1}^{E} (h^e)^{k-1} |(\varphi^e)_h^{-1}|_k \tag{4.114}$$

where all mesh attributes refer to the mesh over the deformed configuration B_t. Proceeding as before, minimization of the error bound in (4.114) for a fixed number of elements E yields the optimal mesh size distribution over B_t as

$$h(\mathbf{x}) = A \left(\sum_{|\alpha|=k} |D^\alpha \varphi_h^{-1}(\mathbf{x})|^2 \right)^{-1/(2(k-1)+d)} \tag{4.115}$$

and

$$A = \left[\frac{1}{E} \int_{B_0} \left(\sum_{|\alpha|=k} |D^\alpha \boldsymbol{\varphi}_h^{-1}(\mathbf{x})|^2 \right)^{d/(2(k-1)+d)} dV_0 \right]^{1/d} \tag{4.116}$$

It should be carefully noted that $h(\mathbf{x})$ differs from the push-forward to B_t of the mesh size distribution (4.107) in general.

4.7 Numerical tests

In this section we collect a suite of tests designed to assess the performance of the approach developed in the foregoing under conditions of strong nonlinearity, history dependency and dynamics. The emphasis is in establishing the accuracy and convergence characteristics of the *overall* procedure, including spatial discretization, temporal discretization and mesh-to-mesh transfer errors.

4.7.1 Static convergence tests

We begin by testing the performance of the method of mesh adaption in the presence of static singularities. Numerically determined convergence curves for an L-shaped and a cracked solid are shown in Figs. 4.3 and 4.4. The material is variously assumed to be linear or nonlinear elastic. In this latter case, the material obeys the compressible Neo-Hookean constitutive laws (4.17), (4.18) and (4.19). In all cases we assume a Poisson's ratio $\nu = 0.25$. These problems contain elastic singularities of varying strengths. The singularity in the L-shaped body owes to the presence of the re-entrant corner, whereas the cracked body exhibits a stronger near-tip singularity. In this latter case, the optimal mesh density (4.112) near the crack tip may be

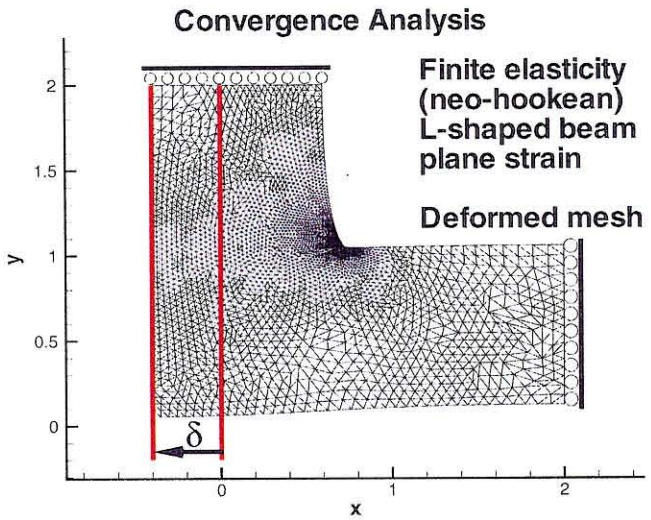

(a)

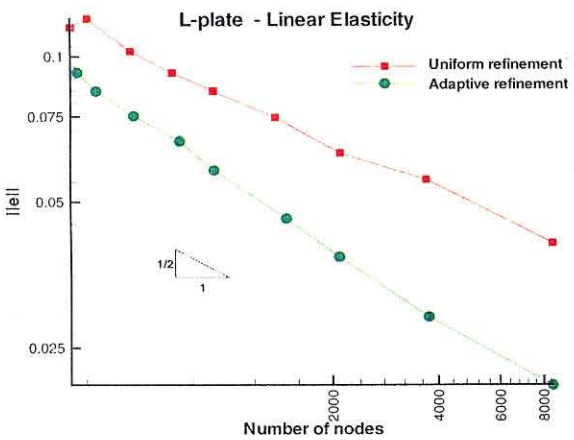

(b)

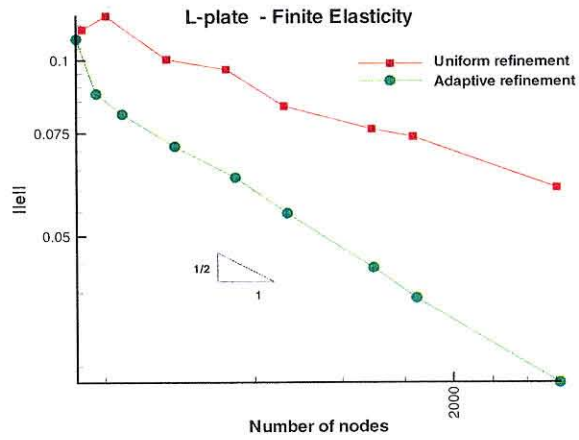

(c)

Figure 4.3: L-shaped elastic 2D solid. a) Schematic; b) convergence rates for linear elastic behavior; c) convergence rates for nonlinear elastic behavior

estimated from the asymptotic linear elastic displacement field:

$$u_1 = \frac{K_I}{2\mu}\sqrt{\frac{r}{2\pi}}\cos\frac{\theta}{2}\left[3-4\nu-1+2\sin^2\frac{\theta}{2}\right] \tag{4.117}$$

$$u_2 = \frac{K_I}{2\mu}\sqrt{\frac{r}{2\pi}}\sin\frac{\theta}{2}\left[3-4\nu+1-2\cos^2\frac{\theta}{2}\right] \tag{4.118}$$

with the result:

$$h(r,\theta) = A\left(\frac{2^7\pi\mu^2}{K_I^2}\right)^{1/4} r^{3/4}\Big[\left(33-56\nu+32\nu^2+3(-7+8\nu)\cos(2\theta)-4\cos(3\theta)\right)^2 + \left(21-40\nu+32\nu^2+3(5-8\nu)\cos(2\theta)+4\cos(3\theta)\right)^2\Big]^{\frac{1}{8}} \tag{4.119}$$

where A follows from (4.113). It is interesting to note that the mesh size reduces to zero as $r^{3/4}$ as the crack tip is approached.

This mesh-size distribution is closely matched by the numerical solution, Fig. 4.4. It bears emphasis, however, that the mesh layout is determined automatically from the numerical solution itself. The details of the mesh generation are given in Chapter 2 and also in [115]. The meshes consist of quadratic six-node triangular elements. The analysis starts with a uniform coarse mesh. The target mesh-size distribution $h(\mathbf{X})$ is then computed and stored on a background octree mesh. The mesh-size distribution thus stored is subsequently used to generate a new mesh comprising the target number of elements E. This process is iterated until the mesh-size distribution $h(\mathbf{X})$ remains ostensibly unchanged.

The convergence curves for the error $\|\tilde{\boldsymbol{\varphi}}_h - \boldsymbol{\varphi}_h\|_1$, eq. (4.110), predicted by the method are also shown in Figs. 4.3 and 4.4. The convergence curves clearly exhibit the optimal convergence rate $O(N^{-(k-1)/d})$ corresponding to the piecewise-linear projection in $\mathbb{R}^d$, despite the presence of singularities. The optimal convergence rate appears to be maintained in the nonlinear case. By contrast, the convergence rate is sub-optimal in the case of uniform refinement, as expected from the presence of singularities in the solution.

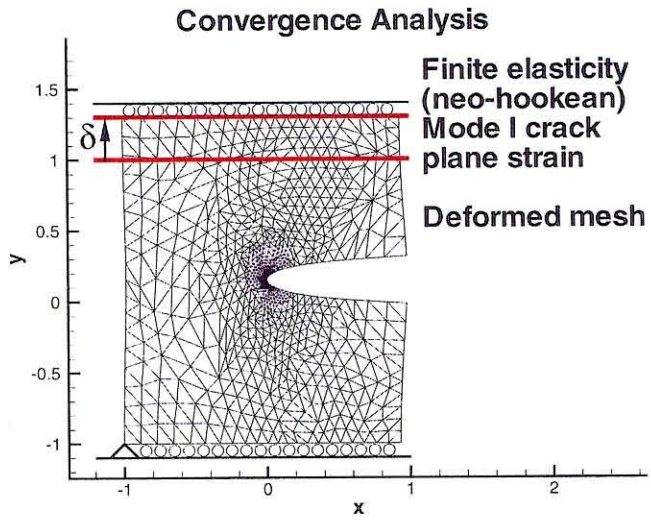

(a)

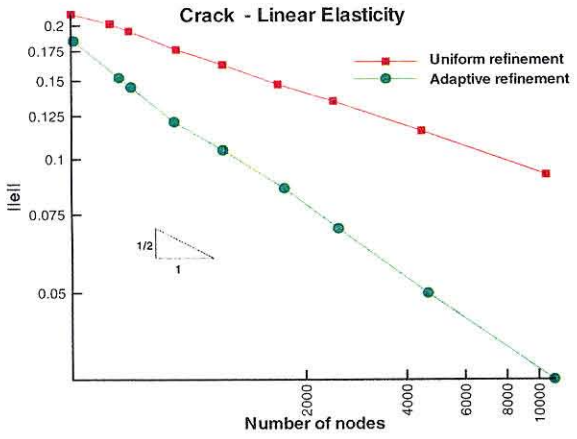

(b)

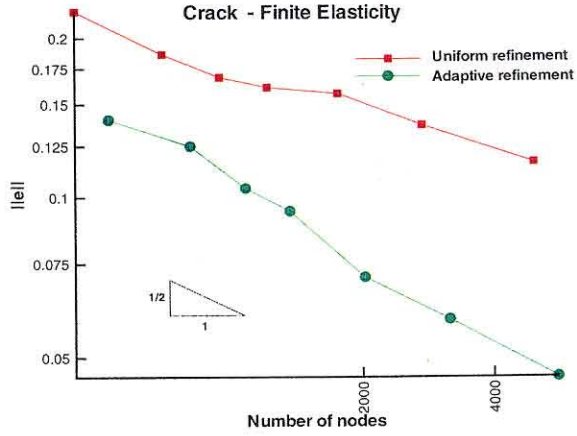

(c)

Figure 4.4: Cracked elastic 2D solid. a) Schematic; b) convergence rates for linear elastic behavior; c) convergence rates for nonlinear elastic behavior

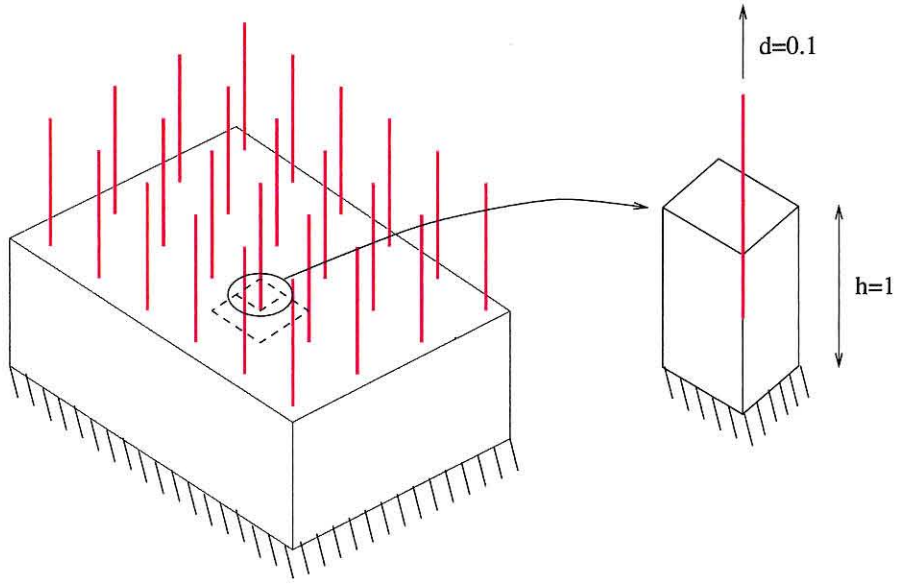

Figure 4.5: Schematic of an idealized fiber pull-out problem

4.7.2 Fiber pull-out

The performance of the method of adaption in three dimensions is illustrated next. To this end, we apply the method to the analysis of load transmission into a nonlinear elastic matrix by a periodic array of partially embedded and perfectly bonded rigid fibers of vanishingly small diameter, Fig. 4.5. This problem is one of importance in the study of fiber-reinforced composites and in soil mechanics.

The analytical treatment of problems in this category dates back to the landmark paper of Mindlin [95], who obtained the solution to the problem of a point load inside an elastic halfspace. Muki and Steinberg [97, 98] studied the problem of transmission of axial loads through a cylindrical bar embedded in–and bonded to–an elastic halfspace. They reduced the problem to the solution of a Fredholm integral equation and presented extensive numerical results illustrating the load decay as well as the asymptotic behavior of the solution. More recently, Freund [44] has investigated the mechanics of a fiber sliding through a hole in an elastic matrix. Freund has obtained exact asymptotic solutions for the limiting cases of a very stiff and a very compliant fiber and has provided numerical results for intermediate cases.

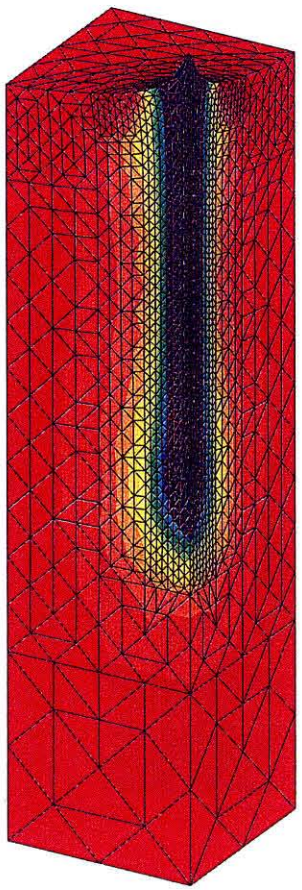

Figure 4.6: Adapted, deformed meshes and axial stress σ_{33} contours computed for the idealized fiber pull-out problem

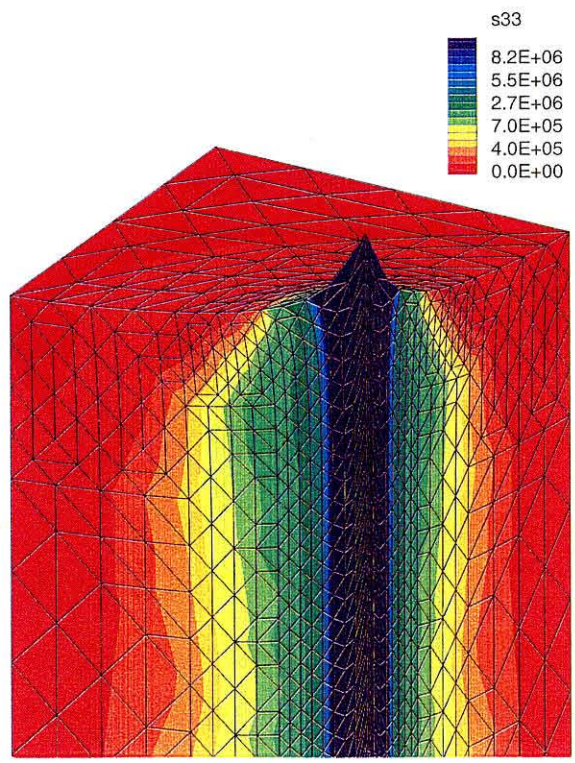

Figure 4.7: Adapted, deformed meshes and σ_{33} contours for the idealized fiber pull-out problem - Detailed view around the fiber

Owing to the presence of singularities along the fiber and at the end points of the fiber, the fiber pull-out problem just defined furnishes a demanding three-dimensional test of the method of adaption. In view of the periodicity of the fiber layout, the analysis may be restricted to one unit cell. The remaining symmetries of the problem enable the calculations to be further restricted to one quarter of the unit cell. The material is assumed to be nonlinear elastic and to obey the Neo-Hookean constitutive law (4.17). The bottom surface of the matrix is fully constrained and an outward displacement is prescribed quasistatically on the fiber. The initial mesh is coarse and uniform. Based on the error estimator, the mesh-size distribution function is determined and the mesh reconstructed accordingly. The meshes are generated by the application of an octree nodal insertion method followed by Delaunay triangulation (see Chapter 2 and [115]). The meshes consist of quadratic ten-node tetrahedra. Figs. 4.6 and 4.7 show the adapted deformed mesh after five levels of refinement. The figures also depict the corresponding contours of axial stress σ_{33}. As is evident from the figures, the sharp gradients in the solution in regions adjacent to the fiber are finely resolved by the adapted mesh.

4.7.3 Dynamic tests

The next two tests are intended to assess the performance of the method under dynamic conditions. The tests concern compressive waves traveling down a shock tube for which exact analytical solutions can be obtained in closed form. These analytical solutions provide a suitable basis for a detailed accuracy assessment. The first problem is concerned with isothermal conditions and does not involve any history variables. The second problem concerns an adiabatic compressive wave and temperature is treated as an internal variable. This aspect of the calculation effectively tests the accuracy of the mesh-to-mesh transfer algorithm.

Isothermal case

A simple test of the mesh adaption capability for nonlinear dynamics is provided by the problem of a plane shock traveling down a highly compressible material. Since our primary focus is on applications to solids, we carry out the analysis in lagrangian setting. The equations to be satisfied comprise the equation of conservation of linear momentum (4.4); compatibility (4.2); and the constitutive relations formulated in Section 4.2.2.

A class of analytically tractable problems is obtained when the free energy is assumed to depend on deformation only through the Jacobian of the deformation, i. e.,

$$A = A(J, T) \tag{4.120}$$

whereupon the equilibrium part of the first Piola-Kirchhoff stress tensor becomes

$$P^{\mathrm{e}}_{iJ} = A_{,J}\,(J, T) J F^{-1}_{Ji} \tag{4.121}$$

In particular, the pressure field follows as

$$p = A_{,J}\,(J, T) \tag{4.122}$$

It should be carefully noted that we have tacitly adopted the solids sign convention for the pressure, i. e., the pressure is positive in tension and negative in compression. In addition, the viscous part of the first Piola-Kirchhoff stress tensor follows from (4.21) and (4.22). In the reminder of this section, attention is restricted to isothermal deformations and, consequently, the temperature T will be omitted throughout.

Next we specialize the above relations to a plane-shock geometry. Let X_1 measure the distance in the direction of propagation of the shock. Assume that the deformation is uniaxial and, therefore, fully described by the component $\varphi_1(X_1, t)$ of the

deformation mapping. The corresponding deformation gradient is of the form:

$$\mathbf{F} = \begin{pmatrix} \varphi_{1,1} & 0 & 0 \\ 0 & 1 & 0 \\ 0 & 0 & 1 \end{pmatrix} \tag{4.123}$$

The Jacobian of the deformation is:

$$J = \varphi_{1,1} \tag{4.124}$$

The rate of deformation evaluates to:

$$\mathbf{d} = \mathrm{sym}(\dot{\mathbf{F}}\mathbf{F}^{-1}) = \begin{pmatrix} \dot{\varphi}_{1,1}/\varphi_{1,1} & 0 & 0 \\ 0 & 0 & 0 \\ 0 & 0 & 0 \end{pmatrix} \tag{4.125}$$

and its deviatoric part to:

$$\begin{aligned} \mathbf{d}^{\mathrm{dev}} &= \mathrm{sym}(\dot{\mathbf{F}}\mathbf{F}^{-1}) \\ &= \begin{pmatrix} (2/3)\dot{\varphi}_{1,1}/\varphi_{1,1} & 0 & 0 \\ 0 & -(1/3)\dot{\varphi}_{1,1}/\varphi_{1,1} & 0 \\ 0 & 0 & -(1/3)\dot{\varphi}_{1,1}/\varphi_{1,1} \end{pmatrix} \end{aligned} \tag{4.126}$$

Furthermore, the equation of conservation of linear momentum (4.4) reduces to:

$$\rho_0 \ddot{\varphi}_1 = P_{11,1} \tag{4.127}$$

where P_{11} follows from (4.8), (4.121), (4.21) and (4.22) in the form:

$$P_{11} = p(\varphi_{1,1}) + \frac{4\eta}{3}\frac{\dot{\varphi}_{1,1}}{\varphi_{1,1}} \tag{4.128}$$

Inserting this expression into (4.127) leads to the governing equation:

$$\rho_0 \ddot{\varphi}_1 = \left[p(\varphi_{1,1}) + \frac{4\eta}{3} \frac{\dot{\varphi}_{1,1}}{\varphi_{1,1}} \right]_{,1} \tag{4.129}$$

to be solved for $\varphi_1(X_1, t)$. We shall seek steady state solutions of (4.129) of the form:

$$\varphi_1 = \varphi_1(X_1 - Vt) \tag{4.130}$$

for some propagation velocity V to be determined. Insertion of (4.130) into (4.129) gives the autonomous equation:

$$\rho_0 V^2 \varphi_{1,11} = \left[p(\varphi_{1,1}) - \frac{4\eta V}{3} \frac{\varphi_{1,11}}{\varphi_{1,1}} \right]_{,1} \tag{4.131}$$

to which we append the boundary conditions:

$$\lim_{X_1 \to \pm\infty} \varphi_{1,1}(X_1) = J^{\pm} \tag{4.132}$$

where $J^{\pm}$ are given. Evidently, eq. (4.131) admits the first integral:

$$\rho_0 V^2 \varphi_{1,1} = p(\varphi_{1,1}) - \frac{4\eta V}{3} \frac{\varphi_{1,11}}{\varphi_{1,1}} + C \tag{4.133}$$

for some constant C. Specializing this expression for $X_1 \to \pm\infty$ and noting that, in these limits, $\varphi_{1,11} \to 0$ in view of (4.132), gives:

$$C = \rho_0 V^2 J^- - p(J^-) = \rho_0 V^2 J^+ - p(J^+) \tag{4.134}$$

whence the propagation velocity V follows as:

$$\rho_0 V^2 = \frac{p(J^+) - p(J^-)}{J^+ - J^-} \tag{4.135}$$

which is the familiar formula for the velocity of propagation of a shock [139]. Eq. (4.133)

can be recast in terms of the Jacobian J, with the result:

$$\rho_0 V^2 J = p(J) - \frac{4\eta V}{3}\frac{J_{,1}}{J} + C \tag{4.136}$$

Evidently, this equation is separable and yields the implicit solution:

$$X_1 = \frac{4\eta V}{3}\int_{(J^- + J^+)/2}^{J} \frac{d\xi}{[C + p(\xi) - \rho_0 V^2 \xi]\xi} \tag{4.137}$$

where we have arbitrarily chose the Jacobian at $X_1 = 0$ to be $(J^- + J^+)/2$.

The integral in (4.137) can be carried out analytically in closed form for certain simple equations of state $p(J)$. Assume, for instance, the relation

$$p(J) = \frac{K}{2}(J - J^{-1}) \tag{4.138}$$

where K is the bulk modulus of the undeformed material. This relation, in conjunction with Newtonian viscosity, provides a reasonable description of the compressibility of polymeric foams such as employed in automotive industry applications [135, 141]. Then, (4.135) gives

$$\rho_0 V^2 = \frac{K}{2}\left(1 + \frac{1}{J^- J^+}\right) \tag{4.139}$$

and (4.137) reduces to:

$$X_1 = -\frac{8\eta V}{3K} J^- J^+ \int_{(J^- + J^+)/2}^{J} \frac{d\xi}{(\xi - J^-)(\xi - J^+)} \tag{4.140}$$

This integral is elementary and evaluates to:

$$X_1 = L \log \frac{J - J^-}{J^+ - J} \tag{4.141}$$

where

$$L = \frac{8\eta V}{3K}\frac{J^- J^+}{J^+ - J^-} \tag{4.142}$$

is a measure of the width of the shock. Finally, (4.141) can be inverted to give:

$$J = \frac{J^- + J^+}{2} + \frac{J^+ - J^-}{2} \tanh \frac{X_1}{2L} \tag{4.143}$$

which is the sought explicit solution. The density field, deformation mapping and velocity field follow directly from (4.143) in the form

$$\rho = \rho_0 / J \tag{4.144}$$

$$\varphi_1 = X_1 + \left[\frac{J^- + J^+}{2} - 1\right](X_1 - Vt) + (J^+ - J^-)L \left\{\log\left[\cosh\left(\frac{X_1 - Vt}{2L}\right)\right] - \log 2\right\} \tag{4.145}$$

$$\dot{\varphi}_1 = \frac{V}{2}\left\{2 - (J^- + J^-) - (J^+ - J^-)\tanh\left(\frac{X_1 - Vt}{2L}\right)\right\} \tag{4.146}$$

These fields are taken as initial conditions and entrance and exit boundary conditions in calculations. The evolution of the analytical density field, deformation mapping and velocity field is shown in Fig. 4.8 for the parameters listed in Table 4.1.

ρ_0	1
K	1
η	0.025
J^+	1
J^-	0.1

Table 4.1: Parameters used in simulations of isothermal compression wave

Adiabatic case

The preceding example effectively tests the adaptive procedure in the context of nonlinear dynamics. However, it lacks state variables in the constitutive description

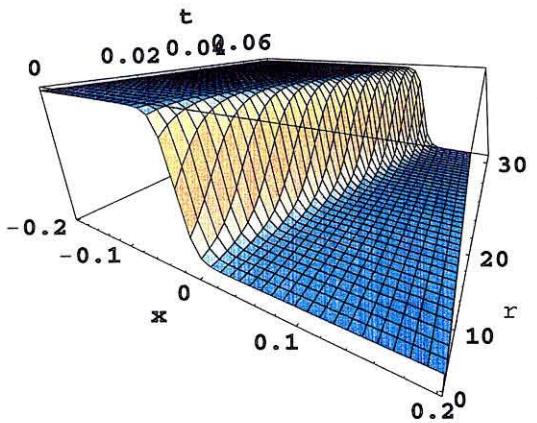

(a) Mass Density field

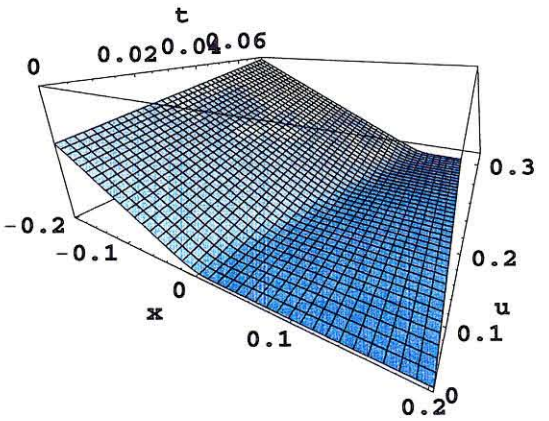

(b) Displacement field

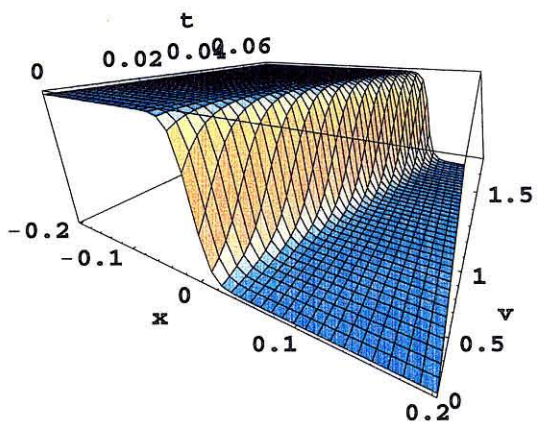

(c) Velocity field

Figure 4.8: Analytical solution for an isothermal compressive wave in a shock tube configuration

and, therefore, does not fully exercise the state-variable transfer operator. A simple extension of the preceding example that overcomes this shortcoming is to account for thermal effects within an adiabatic framework.

Under the conditions just stated, the governing equation (4.129) becomes

$$\rho_0 \ddot{\varphi}_1 = \left[p(\varphi_{1,1}, T) + \frac{4\eta}{3} \frac{\dot{\varphi}_{1,1}}{\varphi_{1,1}} \right] ,_1 \tag{4.147}$$

An additional equation is, therefore, required to determine the temperature field T. This equation is furnished by conservation of energy and is assumed to take the form

$$\rho_0 C_v T_{,t} = P_{iJ} V_{i,J} + H_{I,I} \tag{4.148}$$

where C_v is the heat capacity at constant volume and $\boldsymbol{H}$ is the material heat flux. The energy balance equation (4.148) may be written in conservation form as:

$$(\rho_0 C_v T + \rho_0 |\mathbf{V}|^2/2)_{,t} - (P_{iJ} V_i + H_J)_{,J} = 0 \tag{4.149}$$

For a plane-shock geometry, this equation reduces to:

$$\left(\rho_0 C_v T + \frac{\rho_0}{2} \dot{\varphi}_1^2 \right) ,_t - \left[\left(p(\varphi_{1,1}, T) - \frac{4}{3} \eta \frac{\dot{\varphi}_{1,1}}{\varphi_{1,1}} \right) \dot{\varphi}_1 + H_1 \right] ,_1 = 0 \tag{4.150}$$

Next we make the steady-state assumption:

$$\varphi_1 = \varphi_1(X_1 - Vt) \tag{4.151}$$

$$T = T(X_1 - Vt) \tag{4.152}$$

for some propagation velocity V to be determined. Inserting this representation into (4.147) and (4.150) gives:

$$\rho_0 V^2 \varphi_{1,11} = \left[p(\varphi_{1,1}, T) - \tfrac{4\eta V}{3} \tfrac{\varphi_{1,11}}{\varphi_{1,1}} \right] ,_1 \tag{4.153}$$

$$\left[\rho_0 C_v T + \tfrac{1}{2} \rho_0 V^2 \varphi_{1,1}^2 \right] ,_1 - \left[p(\varphi_{1,1}, T) \varphi_{1,1} - \tfrac{4}{3} \eta V \varphi_{1,11} + H_1 \right] ,_1 = 0 \tag{4.154}$$

which we supplement with the boundary conditions

$$\lim_{X_1 \to \pm\infty} \varphi_{1,1} = J^{\pm} \tag{4.155}$$

$$\lim_{X_1 \to \infty} T = T^{+} \tag{4.156}$$

where T^+ is the temperature ahead of the shock, which is assumed known. Eqs. (4.153) and (4.154) admit the first integral:

$$\rho_0 V^2 \varphi_{1,1} = p(\varphi_{1,1}, T) - \tfrac{4\eta V}{3} \tfrac{\varphi_{1,11}}{\varphi_{1,1}} + C \tag{4.157}$$

$$\rho_0 C_v T + \tfrac{1}{2}\rho_0 V^2 \varphi_{1,1}^2 - p(\varphi_{1,1}, T)\varphi_{1,1} + \tfrac{4}{3}\eta\varphi_{1,11} + H_1 = B \tag{4.158}$$

for some constants B and C. Proceeding as in the preceding section, these constants follow from the identities:

$$C = \rho_0 V^2 J^- - p(J^-, T^-) = \rho_0 V^2 J^+ - p(J^+, T^+) \tag{4.159}$$

$$\begin{aligned} B &= \rho_0 C_v T^+ + \tfrac{1}{2}\rho_0 V^2 J^+ - p(J^+, T^+) J^+ \\ &= \rho_0 C_v T^- + \tfrac{1}{2}\rho_0 V^2 J^- - p(J^-, T^-) J^- \end{aligned} \tag{4.160}$$

where $T^- = T(-\infty)$ and we have assumed that $H_1 \to 0$ as $X_1 \to \pm\infty$. From (4.159) it follows that

$$\rho_0 V^2 = \frac{p(J^+, T^+) - p(J^-, T^-)}{J^+ - J^-} \tag{4.161}$$

whereas (4.160) determines T^-. Proceeding again as in the isothermal case leads to the implicit solution:

$$X_1 = \frac{4\eta V}{3} \int_{(J^- + J^+)/2}^{J} \frac{d\xi}{[C + p(\xi, T) - \rho_0 V^2 \xi]\xi} \tag{4.162}$$

Furthermore, assume that the deformation is adiabatic and H_1 can be neglected.

Then, eq. (4.158) becomes algebraic in T, namely,

$$\rho_0 C_v T + \frac{1}{2}\rho_0 V^2 \varphi_{1,1}^2 - p(\varphi_{1,1}, T)\varphi_{1,1} + \frac{4}{3}\eta\varphi_{1,11} = B \tag{4.163}$$

Solving this equation for T gives a relation of the form:

$$T = T(\varphi_{1,1}) \tag{4.164}$$

whereupon (4.162) becomes:

$$X_1 = \frac{4\eta V}{3}\int_{(J^- + J^+)/2}^{J} \frac{d\xi}{[C + p(\xi, T(\xi)) - \rho_0 V^2 \xi]\xi} \tag{4.165}$$

which is the sought solution.

The adiabatic solution (4.164) and (4.165) can be obtained analytically in closed form for certain simple equations of state. Perhaps the simplest form which is amenable to such treatment is:

$$p = -TS'(J), \qquad S'(J) = \frac{\rho_0 C_v}{J(a_0 J^2 + a_1 J + a_2)} \tag{4.166}$$

where a_0, a_1 and a_2 are dimensionless material constants. The equation of state (4.166) may be thought of as describing the behavior of a van der Waals-like gas. The boundary conditions (4.155) and (4.155) furnish the relations

$$a_0 = \frac{1}{2J^+ J^-} \tag{4.167}$$

$$a_1 = -\frac{J^+ + J^-}{J^+ J^-} \tag{4.168}$$

Furthermore, in order to simplify subsequent expressions, we parametrize the material constant a_2 as

$$a_2 = 1 + \frac{\rho_0 C_v T^+}{K} + \frac{1}{2}\frac{J^+}{J^-} \tag{4.169}$$

in terms of the parameter K. Then, (4.161) gives

$$\rho_0 V^2 = \frac{K}{J^- J^+} \tag{4.170}$$

Inserting the equation of state (4.166) into (4.163), solving for T and applying the boundary condition (4.156), we find:

$$T = \frac{K}{\rho_0 C_v}(a_0 J^2 + a_1 J + a_2) \tag{4.171}$$

The constant C in (4.159) is obtained as:

$$C = \frac{K(J^+ + J^-)}{J^+ J^-} \tag{4.172}$$

Inserting (4.172) and (4.166) into (4.165) we find:

$$X_1 = -\frac{4\eta}{3\rho_0 V} \int_{(J^- + J^+)/2}^{J} \frac{d\xi}{(\xi - J^-)(\xi - J^+)} \tag{4.173}$$

This integral is elementary and evaluates to:

$$X_1 = L \log \frac{J - J^-}{J^+ - J} \tag{4.174}$$

where

$$L = \frac{4\eta}{3\rho_0 V(J^+ - J^-)} \tag{4.175}$$

Finally, inverting (4.173) gives the explicit solution:

$$J = \frac{J^- + J^+}{2} + \frac{J^+ - J^-}{2} \tanh \frac{X_1}{2L} \tag{4.176}$$

which is of the same form as (4.143). The deformation mapping and the velocity field also retain the same form as before, respectively eqs. (4.145) and (4.146), whereas

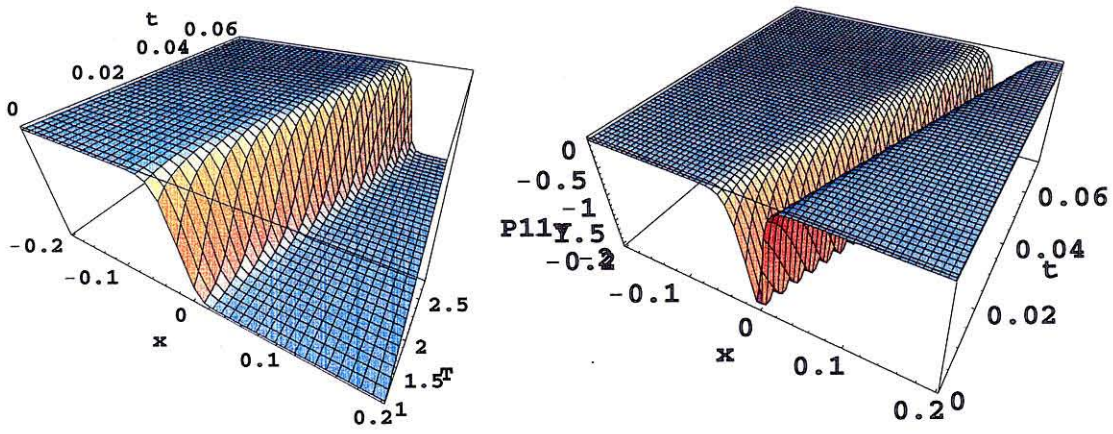

(a) Temperature field

(b) P^v_{11} field

Figure 4.9: Analytical solution for an adiabatic compression wave in a shock tube configuration

the temperature field follows from (4.171) as

$$T(X_1,t) = \frac{1}{8\rho_0 C_v J^- J^+}\Bigg[-3J^{-2}K + J^{+2}K + 2J^- J^+(K + 4\rho_0 C_v T^+) + (J^{-2} - J^{+2})K\tanh\frac{X_1 - Vt}{2L}\left[2 + \tanh\frac{X_1 - Vt}{2L}\right]\Bigg] \quad (4.177)$$

The viscous stresses follow from (4.21) and (4.22) as

$$P^v_{11} = -2P^v_{22} = -2P^v_{33} = \frac{1}{4}(J^+ - J^-)^2\rho_0 V^2 \mathrm{sech}^2\frac{X_1 - Vt}{2L} \quad (4.178)$$

The evolution of the analytical temperature and viscous stress fields is shown in Fig. 4.9 for the parameters listed in Table 4.2. These fields are used as initial conditions for the numerical solution of the energy equation.

Numerical implementation

Some issues of implementation of the dynamic tests just described merit further comment. While the compression waves are one-dimensional in nature, the problems are solved as if they were two or three-dimensional. The domain of analysis is dis-

ρ_0	1
C_v	1
T^+	1
K	1
η	0.025
J^+	1
J^-	0.1

Table 4.2: Parameters used in simulations of adiabatic compression wave

cretized using six-node triangular elements in two dimensions, and ten-node tetrahedral elements in three dimensions. In both cases the interpolation is quadratic, i. e., $k = 2$. The stress update is effected in accordance with the procedure outlined in Section 4.3.2 for a compressible fluid with Newtonian viscosity. The equivalent static problem which results from the use of implicit time-stepping algorithms is solved by a Newton-Raphson solution procedure based on exact or consistent tangents. It bears emphasis that, due to the potential structure of the stress update, the resulting stiffness matrices are symmetric.

Both implicit and explicit time integration are considered. In the implicit case we set Newmark's parameters to $\gamma = 0.5$ and $\beta = 0.25$. In the explicit case we set $\beta = 0$ and $\gamma = 0.5$, which corresponds to the second order accurate central difference scheme [11, 58]. In this case, we estimate the stable time step as

$$\Delta t \leq \min \left\{ \frac{h_{\min}}{V}, \frac{\rho_0 h_{\min}^2}{\eta} \right\} \tag{4.179}$$

where $h_{\min}$ is the minimum element inradius.

In the adiabatic compression wave case, the temperatures are calculated at the quadrature points from the energy equation by recourse to the explicit forward-Euler scheme:

$$T_{n+1} = T_n + \frac{\triangle t}{\rho_0 C_v} \left(\mathbf{P}_n \cdot \nabla_0 \mathbf{V}_n + \nabla_0 \cdot \mathbf{Q}_n \right) \tag{4.180}$$

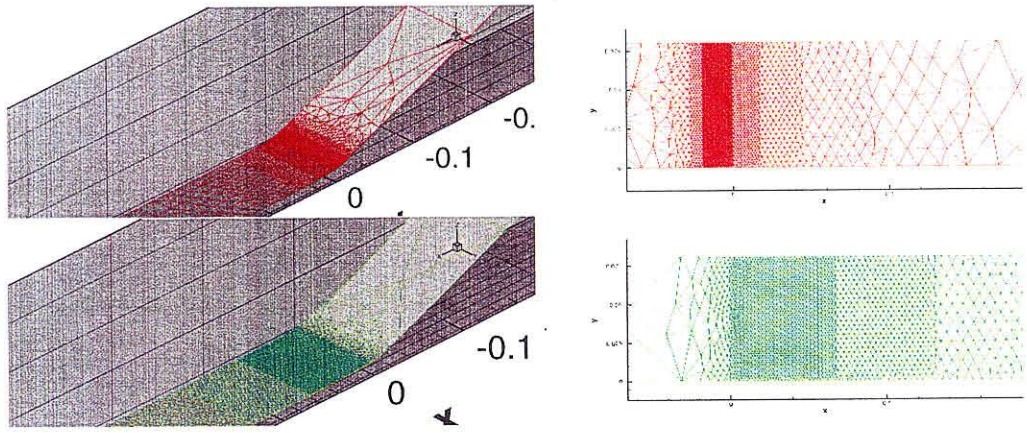

(a) Analytical displacement field

(b) Mesh details

Figure 4.10: Mesh adapted on the deformed configuration (top) *vs.* mesh adapted on the undeformed configuration and subsequently pushed forward to the deformed configuration (bottom)

The corresponding stable time step is estimated as

$$\triangle t \leq \frac{\rho_0 C_v T^+ L}{KV(J^+ - J^-)} \tag{4.181}$$

It bears emphasis that the temperature is treated as a parameter as regards the formulation of state updates. In all the tests reported here, however, the stable time step is always dictated by the explicit dynamics.

From the analytical solution (4.145) and the expressions for the optimal mesh size distribution in the reference (4.112) and the deformed configurations (4.115), it is possible to obtain expressions for the optimal mesh-size distribution, with the result

$$h(X_1) = 2\sqrt{\frac{HL\tanh(l/2L)}{E}}\cosh\frac{X_1}{2\,L}, \tag{4.182}$$

and

$$h(x_1) = A\sqrt{\frac{L\left[J^+ + J^- + (J^+ - J^-)\,\tanh(x_1/2L)\right]^3}{2(J^+ - J^-)}}\cosh\frac{x_1}{2\,L} \tag{4.183}$$

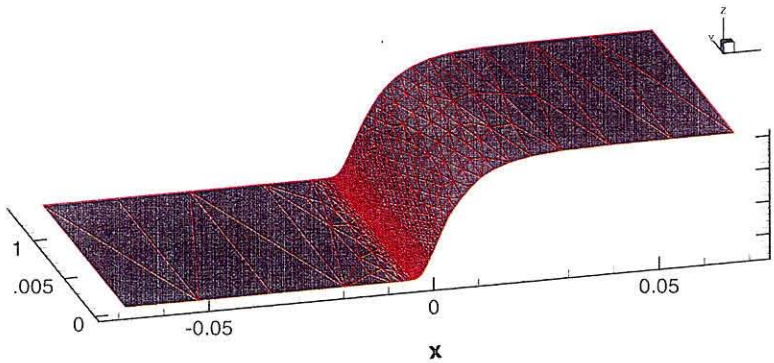

(a) Spatial volumetric deformation field $J(x_1)$.

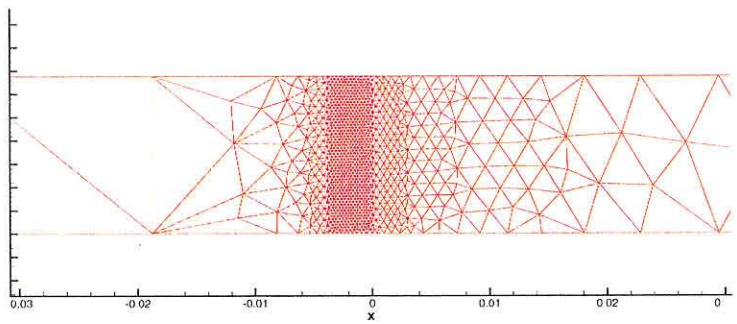

(b) Mesh adapted according to (4.115)

Figure 4.11: Spatial shock profile showing symmetry breaking of the adapted mesh density

where

$$A = \frac{2\sqrt{(H/E)(J^{+2} - J^{-2}\sinh(l/L)}}{[(J^- + J^+)\cosh(l/2L) + (J^- - J^+)\sinh(l/2L)][J^- + J^+ + (J^+ - J^-)\tanh(l/2L)]}$$

where l is the length of the computational domain, H the width, and E is the prescribed number of elements.

Fig. 4.10 shows the analytical displacement field (4.145) on deformed meshes adapted in the deformed configuration, according to the mesh size distributions (4.183) and (4.182). It is evident from the figure that, owing to the very large deformations, the mesh adapted on the reference configuration, eq. (4.182), fails to resolve the shock structure adequately, by exhibiting refinement in regions of slow variation in the solution. By contrast, the mesh adapted directly on the deformed configuration, eq. (4.183), exhibits the strongest refinement across the shock and rapidly coarsens elsewhere, as expected. These observations illustrate the need to adapt the mesh directly on the deformed configuration, as remarked in Section 4.6. It is interesting to note that the optimal mesh-size distribution (4.183) lacks symmetry with respect to the centerline of the shock, Fig. 4.11.

All two and three-dimensional meshes shown here and subsequently are generated by the combination of an octree nodal insertion method and an advancing-front/Delaunay triangulation procedure as presented in Chapter 2 and in [115]. The ability of the mesher to conform to very steep gradients in the mesh-size distribution function, such as required to resolve a very narrow shock, is particularly remarkable, Fig. 4.12.

Dynamic convergence tests

The accuracy and convergence attributes of the method of adaption, and particularly the attendant rates of convergence, may be exhibited with the aid of conventional convergence plots. The calculations start from the analytical solution for a shock centered within the domain of analysis. A numerical time integration step is subsequently carried out. The initial mesh is adapted to the analytical solution, thus

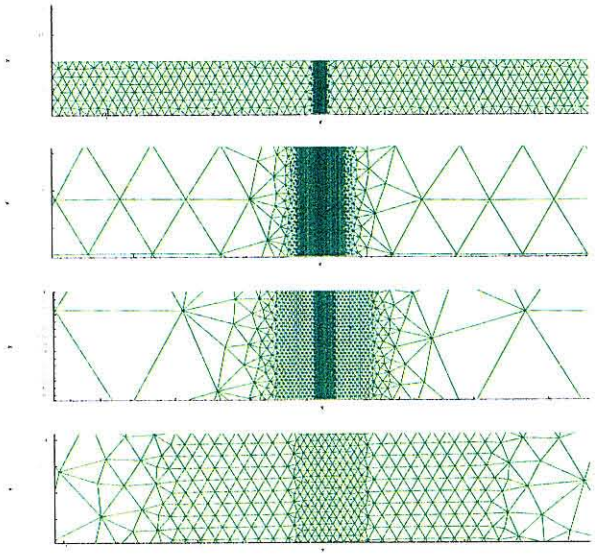

Figure 4.12: Exploded views of the adapted mesh illustrating the ability of the mesh generator to deal with steep mesh-size gradients

minimizing the initial interpolation error. Following the time integration step, the mesh is adapted again to the updated numerical solution, and all fields are transferred to the new mesh using the mesh-to-mesh transfer operator defined in eqs. (4.90-4.94). At this point, the norms of the error functions $\varphi - \varphi_h$ and $\varphi_h - \tilde{\varphi}_h$ are computed. Here as previously, φ is the exact deformation mapping, φ_h is the quadratic finite element deformation mapping, $k = 2$, and $\tilde{\varphi}_h$ is its linear interpolant, $k = 1$. These errors are then plotted against the number of degrees of freedom on log-log axes. The slopes of the resulting curves are the corresponding rates of convergence. It bears emphasis that the errors induced by the mesh-to-mesh transfer operator, eqs. (4.90-4.94), are taken into account in the convergence analysis. However, it should be carefully noted that the state transfer operator (4.94) is exercised in the adiabatic case only.

The parameters listed in Tables 4.1 and 4.2 are used in calculations. The length of the domain of the analysis is $l = 20L$, where L is the width of the shock.

Figs. 4.13 and 4.14 show the convergence curves obtained in the isothermal and adiabatic cases, for both explicit and implicit time integration. It should be noted that in all cases the time step is chosen within the range of stability and, consequently,

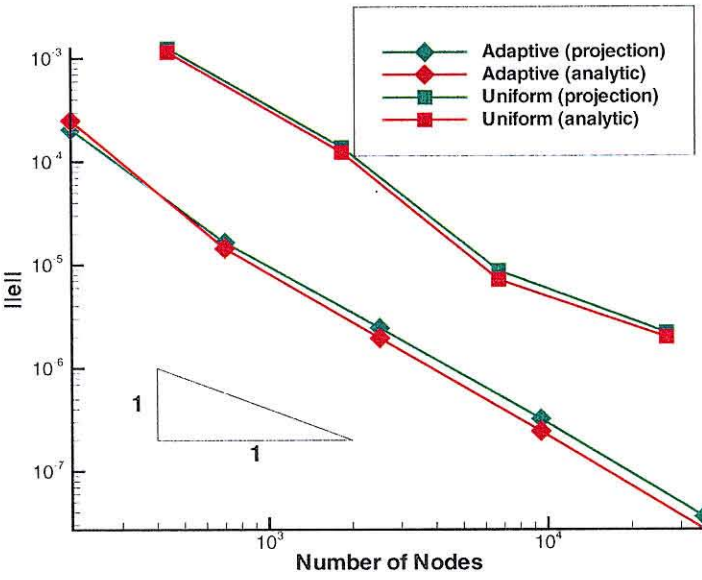

(a) Explicit time integration

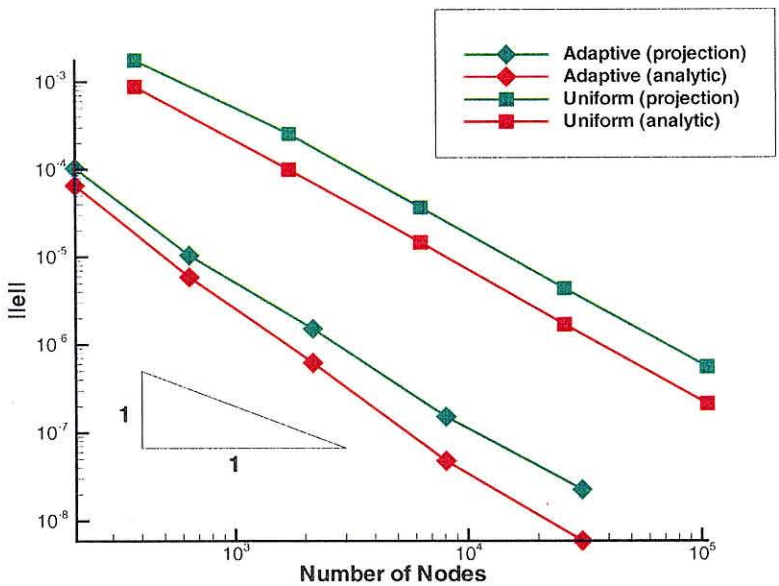

(b) Implicit time integration

Figure 4.13: Convergence plots for isothermal compressive wave problem

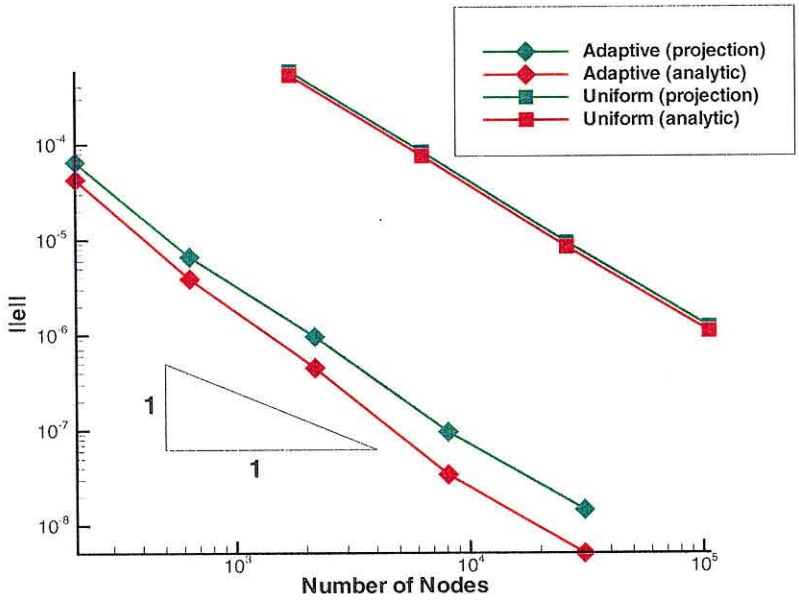

(a) Explicit time integration

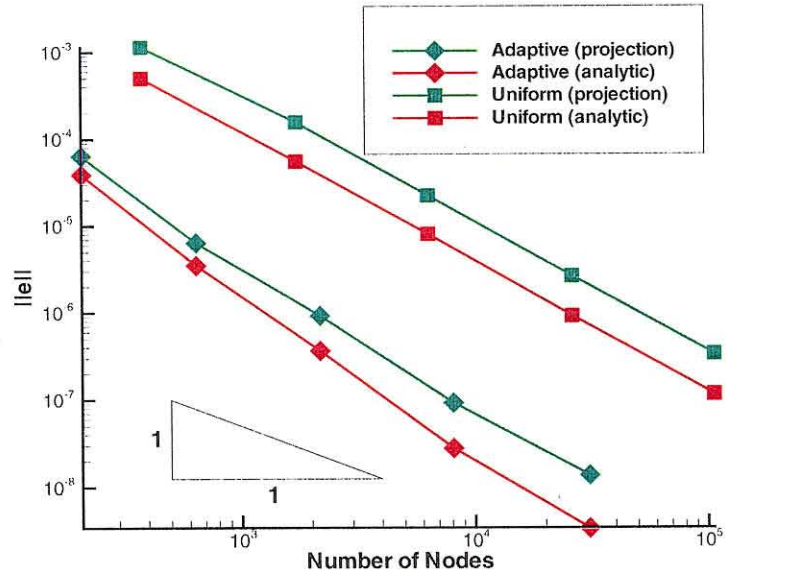

(b) Implicit time integration

Figure 4.14: Convergence plots for adiabatic compressive wave problem

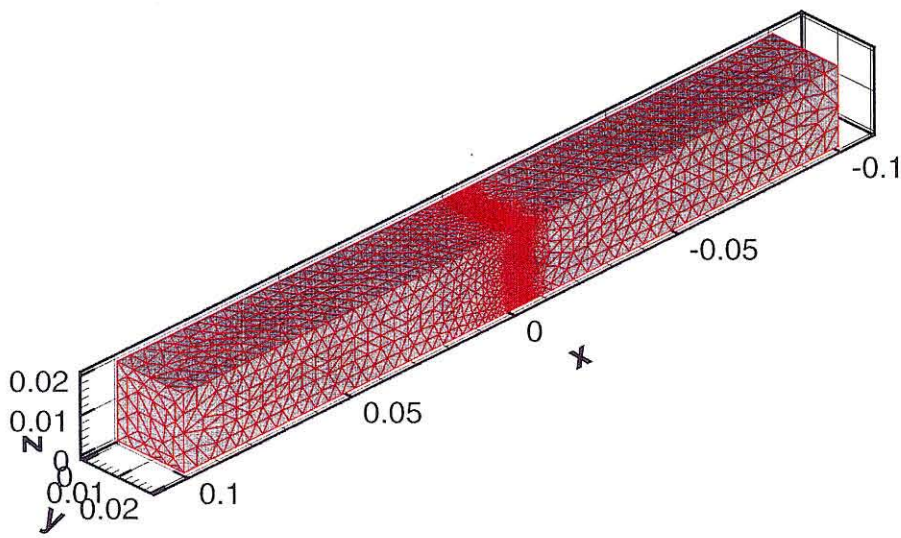

(a) Surface mesh

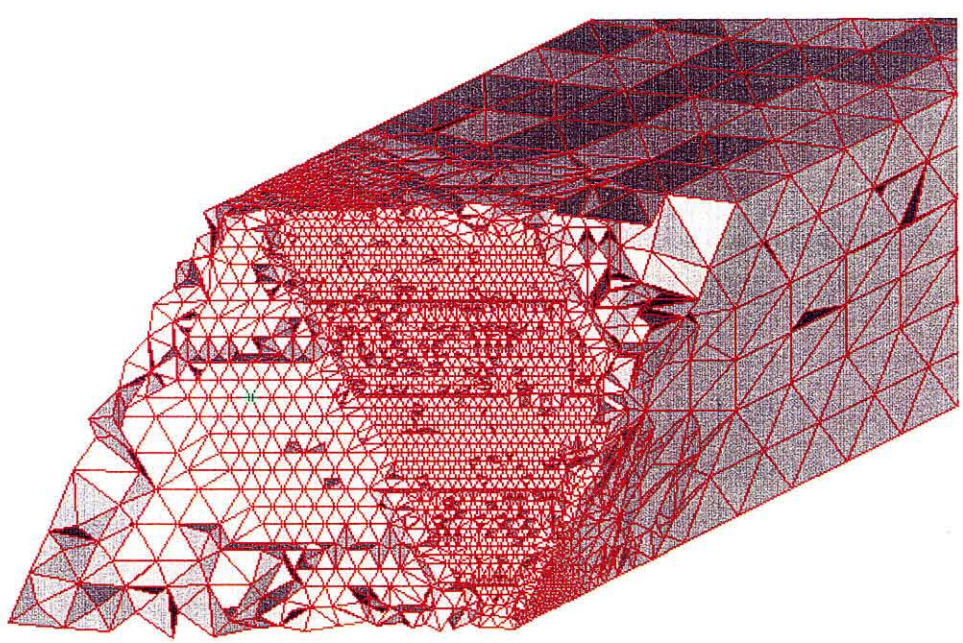

(b) Detail of the mesh in the interior

Figure 4.15: 3D mesh adaption, mesh detail. The mesh contains 205, 384 elements.

decreases as the mesh is refined. Each plot collects four curves, corresponding to uniform and adaptive refinement, and two different measures of the error: $\|\varphi - \varphi_h\|_1$ and $\|\varphi_h - \tilde{\varphi}_h\|_1$. As is evident from the convergent plots, the rate of convergence obtained in the dynamic tests is faster than in the static cases discussed in the foregoing. A plausible explanation is that, as the time step is decreased, the inertia–or L_2–term in the Dirichlet form (4.79) becomes dominant. From a purely heuristic viewpoint, this may be interpreted as a decrease in the order of the Dirichlet form from $m = 1$ to $m = 0$. Under these conditions, the theoretical rate of convergence may be expected to be closer to $O(N^{-k/d})$ than to the static value $O(N^{-(k-1)/d})$, as born out by the computed convergence plots.

The errors in the adaptive case are considerably smaller than their uniform refinement counterparts at an equal number of degrees of freedom. Conversely, the number of degrees of freedom required to attain the same level of accuracy is vastly larger in the case of uniform refinement than in the case of mesh adaption. In addition, the ratio between the two increases monotonically as a power of N. The benefits of mesh adaption are therefore more considerable for large meshes. These differences notwithstanding, it is observed that the uniform refinement solutions attain the same convergence rate as the adaptive solutions, as expected from the absence of singularities in the solution.

Finally, Fig. 4.15 shows a detail of the mesh of a 3D shock adapted according to the procedure described earlier. The mesh contains 205,384 elements, which are densely concentrated within the shock front. The errors computed after the application of the mesh-to-mesh transfer operator are $\|\varphi_h - \tilde{\varphi}_h\|_1 = 4.081195 \times 10^{-10}$ and $\|\varphi - \varphi_h\|_1 = 8.714430 \times 10^{-14}$, which demonstrates the ability of the mesh adaption procedure to accurately resolve fine features of three-dimensional solutions.

Simulation of shock propagation

Finally, we present full simulations of the propagation of a planar compression wave in a highly compressible material under isothermal and adiabatic conditions. As in the preceding convergence study, the problem is modeled after the analytical solutions

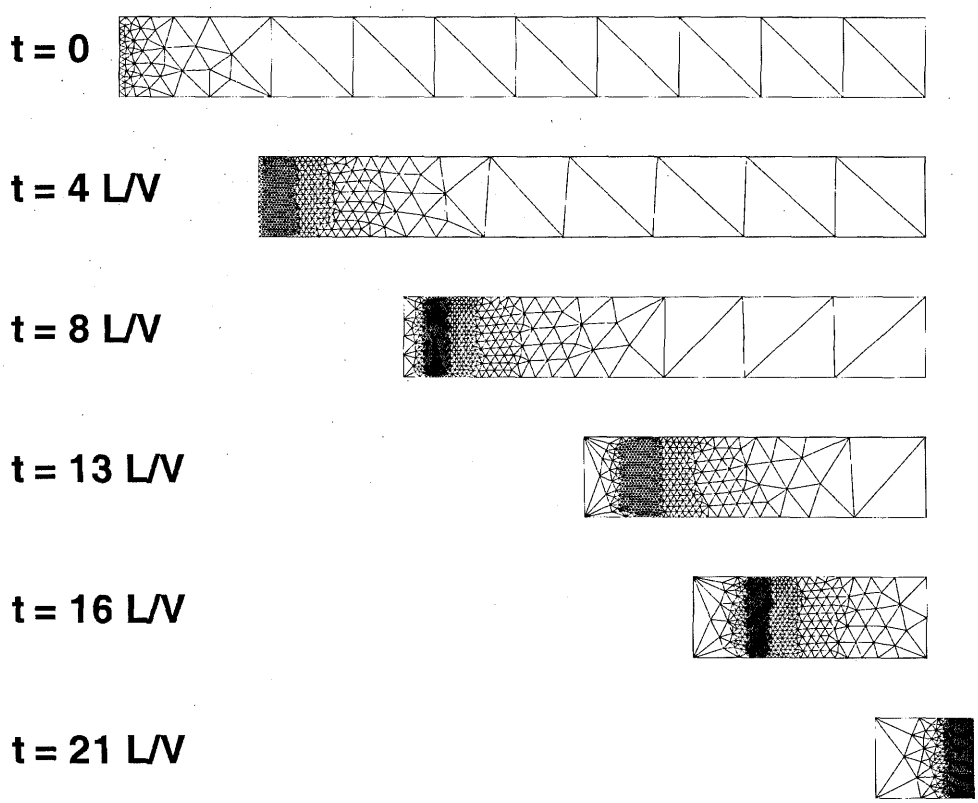

Figure 4.16: Propagation of a planar compression wave. Adapted meshes at several times (isothermal case)

derived in Sections 4.7.3 (isothermal case) and 4.7.3 (adiabatic case). The analytical solutions provide the initial and boundary conditions, eqs. (4.144), (4.145) and (4.146). In the adiabatic case, we use eqs. (4.177) and (4.178) as initial conditions for the energy equation.

We simulate the entrance, propagation and exit of the shock in a tube of length $l = 20L$ in the direction of propagation. The parameters in Tables 4.1 and 4.2 are used in the simulations. The center of the shock is initially located at the tube's left end and the shock propagates from left to right. The mesh is adapted every time the shock front has traveled its characteristic width, *i. e.*, at $\frac{L}{V}$ time intervals. After each remeshing, the nodal fields and state variables are transferred from the old mesh to the new mesh using the mesh-to-mesh transfer operator (4.90-4.94). The stable time

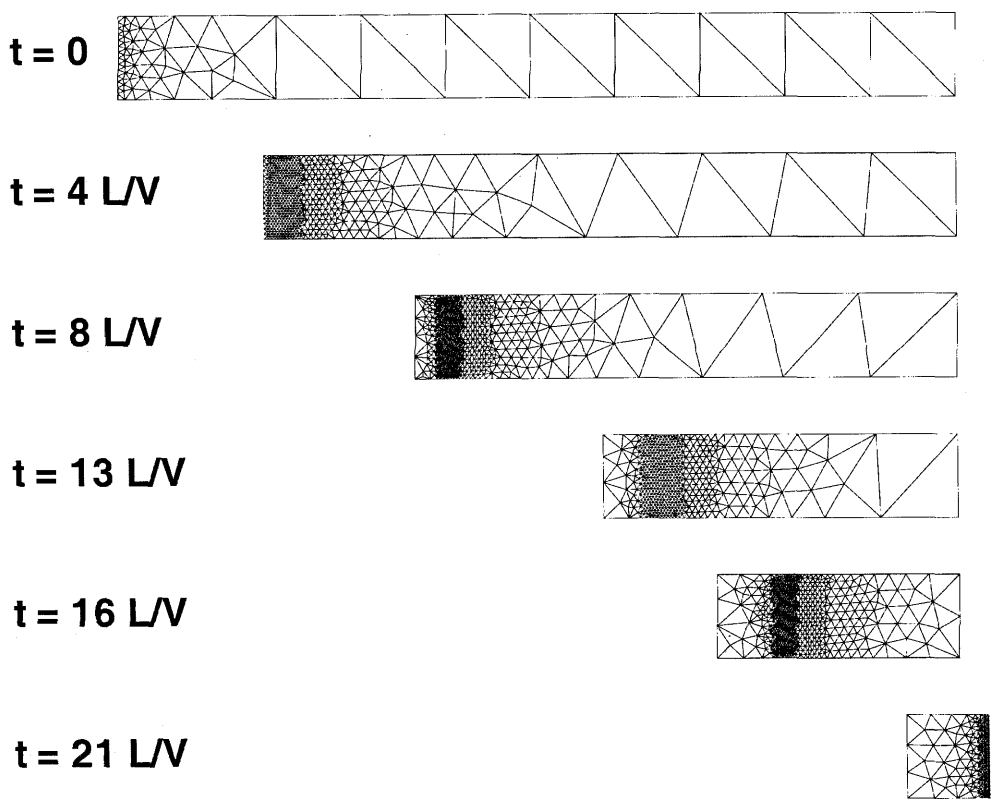

Figure 4.17: Propagation of a planar compression wave. Adapted meshes at several times (adiabatic case)

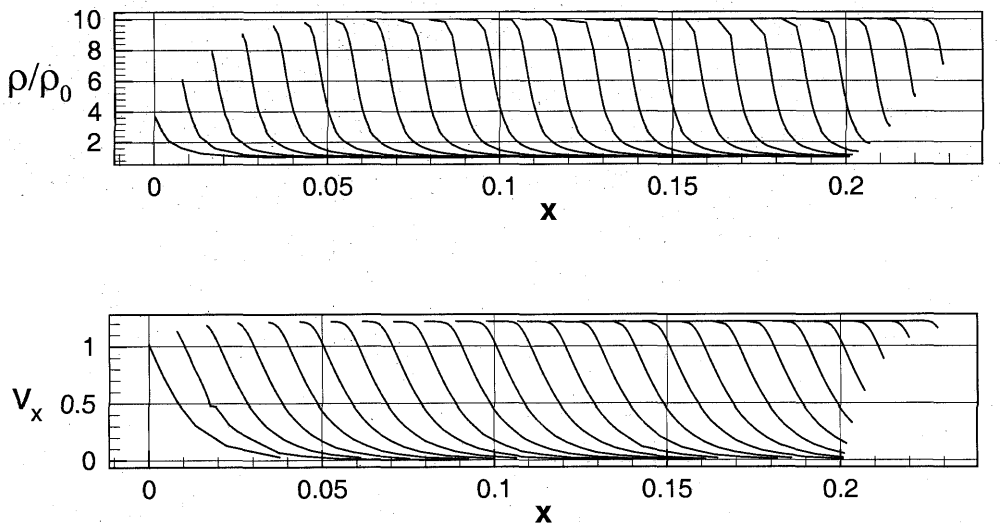

Figure 4.18: Propagation of a planar compression wave. Time evolution of the computed density and velocity fields (isothermal case)

step is then recomputed according to (4.179) and (4.181).

Figs. 4.16 and 4.17 show a sequence of snapshots of the evolution of the adapted mesh during the simulation. It can be observed from these figures that the mesh adaption procedure accurately resolves the shock front and coarsens the mesh behind and ahead of it. The ability of the refined mesh to track the shock as it travels down the tube is quite remarkable.

Figs. 4.18 and 4.19 show the time evolution of the relevant fields, namely, density and velocity in the isothermal case, Fig. 4.19; and pressure, and the temperature in the adiabatic case, Fig. 4.19. The fields are sampled at time intervals of $\frac{L}{V}$. The numerical solutions are ostensibly free of oscillations and exhibit very little dispersion. As a quantitative measure of the accuracy of the solutions, we have computed the time evolution of the energy norm of the error functions $\varphi - \varphi_h$ and $\varphi_h - \tilde{\varphi}_h$. In both the isothermal or the adiabatic case, all error measures remain at levels below 10^{-9} throughout the analysis. We have also computed the retardation in the propagation speed $\frac{V-V_h}{V}$, where V_h is the numerical propagation velocity. The position of the

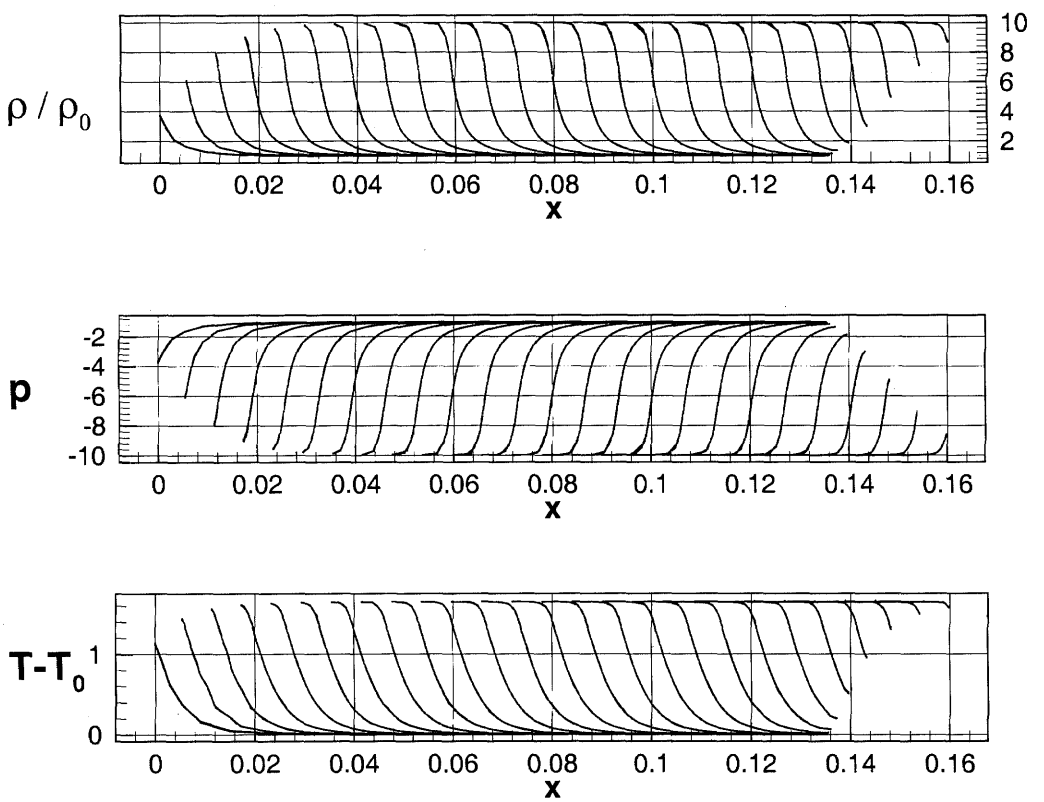

Figure 4.19: Propagation of a planar compression wave. Time evolution of the computed density, pressure and temperature fields (adiabatic case)

shock front used in the computation of V_h is conventionally identified with the point at which $J = (J^+ + J^-)/2$. After the shock has traveled a distance equal to ten times the characteristic shock width L, the computed value for the retardation is 0.6% in the isothermal case and 0.8% in the adiabatic case. The ability of the mesh adaption procedure to accurately track the shock structure is noteworthy.

4.8 Summary and conclusions

We have developed a framework for mesh adaption in strongly nonlinear, possibly dynamic, problems. As in the recent work of Friesecke and Dolzmann [45], we reduce the dynamic problem to an equivalent static problem by recourse to time discretization. We then show that the solutions of the incremental boundary value problem for a wide class of materials obey a minimum principle, provided that the constitutive updates are formulated appropriately. We have taken this minimum principle as a basis for error estimation. In particular, we chose to monitor the error of a lower-order projection of the finite element solution. The optimal mesh size distribution then follows from error indicators which are rigorously local and *a posteriori*. The requisite mesh-to-mesh transfer operators, whereby the nodal and state variables are remapped to the new mesh, also follow consistently from the variational principle.

The advantages attendant to monitoring the error of a lower-order projection of the finite element solution, and adapting the mesh based on this error, seem to have gone unnoticed heretofore. While the emphasis in this thesis has been on nonlinear dynamic problems, the approach is equally attractive within the framework of linear problems. Thus, the method requires only a local comparison between the finite element solution and its lower-order interpolant. It also requires only the calculation of derivatives of the finite element solution which are well-defined locally, thus bypassing the need for smoothing the solution over adjacent elements in an effort to extract derivatives of unnaturally high order.

We have demonstrated the accuracy, robustness and versatility of the computational framework with the aid of demanding convergence tests and examples of

application. To this end, we have found analytically tractable problems involving isothermal and adiabatic shocks particularly useful as stringent tests of the overall accuracy of the method, including spatial and time-stepping discretization errors, and the error incurred as a result of the mesh-to-mesh transfer operator. The ability of method to adaptively resolve the shock structure and yield convergent approximations is particularly satisfying.

Bibliography

[1] N. Amenta and M. Bern. Surface reconstruction by Voronoi filtering. To appear in 14th Annual ACM Symposium on Computational Geometry, 1998.

[2] F. Armero. Large-Scale Modeling of Localized Dissipative Mechanisms in a Local Continuum: Applications to the Numerical Simulation of Strain Localization in Rate-Dependent Inelastic Solids. Technical report, Department of Civil and Environmental Engineering, University of California, Berkeley, August 1997.

[3] R. J. Asaro and J. R. Rice. Strain localization in ductile single crystals. *Journal of the Mechanics and Physics of Solids*, 25:309, 1977.

[4] P. Bach and O. Hassager. An algorithm for the use of the lagrangian specification in newtonian fluid mechanics and applications to free surface flow. *Journal of Fluid Mechanics*, 152:173–190, 1985.

[5] P. L. Baehmann, S. L. Wittchen, M. S. Shephard, K. R. Grice, and M. A. Yerry. Robust, Geometrically Based, Automatic Two-Dimensional Mesh Generation. *International Journal for Numerical Methods in Engineering*, 24:1043–1078, 1987.

[6] T. J. Baker. Automatic mesh generation for complex three-dimensional regions using a constrained Delaunay triangulation. *Engineering with Computers*, 5:161–175, 1989.

[7] J. M. Ball. Constitutive inequalities and existence theorems in nonlinear elastostatics. In R. J. Knops, editor, *Nonlinear Analysis and Mechanics: Heriot-Watt Symposium*, volume I, pages 187–241. Pitman Publising Ltd., 1977.

[8] J. M. Ball and R. D. James. Fine Phase Mixtures as Minimizers of Energy. *Archive for Rational Mechanics and Analysis*, 100:13–52, 1987.

[9] J. M. Ball and J. E. Marsden. Quasiconvexity at the boundary, positivity of the second variation and elastic stability. *Archive for Rational Mechanics and Analysis*, 86:251–277, 1984.

[10] M.W. Beall and M. S. Shephard. A general topology-based mesh data structure. *International Journal for Numerical Methods in Engineering*, 40:1573–1596, 1997.

[11] T. Belytschko. An overview of semidiscretization and time integration procedures. In T. Belytschko and T. J. R. Hughes, editors, *Computational Methods for Transient Analysis*, pages 1–65. North-Holland, 1983.

[12] T. Belytschko, J. Fish, and B. E. Engelmann. A finite element with embedded localization zones. *Computer Methods in Applied Mechanics and Engineering*, 70(1):59–89, 1988.

[13] T. Belytschko and M. Tabbara. H-Adaptive Finite Element Methods for Dynamic Problems, with Emphasis on Localization. *International Journal for Numerical Methods in Engineering*, 36:4245–4265, 1993.

[14] T. B. Belytschko and J.M. Kennedy. A fluid-structure finite element method for the analysis of reactor safety problems. *Nuclear Engineering and Design*, 38:71–81, 1976.

[15] H. Borouchaki and S. H. Lo. Fast Delaunay triangulation in three dimensions. *Computer Methods in Applied Mechanics and Engineering*, 128:153–167, 1995.

[16] A. Bowyer. Computing dirichlet tesslations. *The Computer Journal*, 24(2):162–166, 1981.

[17] E.G. Buratynski. Fully automatic three-dimensional mesh generator for complex geometries. *International Journal for Numerical Methods in Engineering*, 30:931–952, 1990.

[18] G. T. Camacho. *Computational Modelling of Impact Damage and Penetration of Brittle and Ductile Solids.* PhD thesis, Brown University, Providence, Rhode Island, May 1996.

[19] G. T. Camacho and M. Ortiz. Computational Modelling of Impact Damage in Brittle Materials. *International Journal of Solids and Structures*, 33 (20-22):2899–2938, 1996.

[20] G. T. Camacho and M. Ortiz. Adaptive Lagrangian Modelling of Ballistic Penetration of Metallic Targets. *Computer Methods in Applied Mechanics and Engineering*, 142:269–301, 1997.

[21] C. Carstensen and P. Plechac. Adaptive mesh refinement in scalar non-convex variational problems. *Berichsreihe des Mathematischen Seminars Kiel*, 97-2:1–12, 1997.

[22] C. Carstensen and P. Plechac. Numerical Solution of the Scalar Double-Well Problem Allowing Microstructure. *Mathematics of Computation*, 66(219):997–1026, 1997.

[23] P. Carter and J. B. Martin. Work bounding functions for plastic materials. *Journal of Applied Mechanics*, 98:434–438, 1976.

[24] J. C. Cavendish, D. A. Field, and W. H. Frey. An Approach to Automatic Three-Dimensional Finite Element Mesh Generation. *International Journal for Numerical Methods in Engineering*, 21:329–347, 1985.

[25] C. T. Chan and K. Anastasiou. An automatic tetrahedral mesh generation scheme by the advancing-front method. *Communications in Applied Numerical Methods*, 13:33–46, 1997.

[26] B. Chazelle et al. Application challenges to computational geometry: Impact task force report. Technical Report TR-521-96, Princeton Univ., 1996.

[27] P. Chew. Constrained Delaunay triangulations. *ACM*, 1987.

[28] M. Chipot and D. Kinderlehrer. Equilibrium configurations of crystals. *Archive for Rational Mechanics and Analysis*, 103:237–277, 1988.

[29] P. G. Ciarlet. *Numerical analysis of the finite element method.* Les Presses de L'Universite de Montreal, Quebec, Canada, 1976.

[30] A. W. Craig, M. Ainsworth, J. Z. Zhu, and O. C. Zienkiewicz. *h* and *h-p* Version Error Estimation and Adaptive Procedures from Theory to Practice. *Engineering with Computers*, 5:221–234, 1989.

[31] A. M. Cuitiño and M. Ortiz. Computational Modelling of Single Crystals. *Modelling and Simulation in Materials Science and Engineering*, 1:255–263, 1992.

[32] B. Dacorogna. *Direct Methods in the Calculus of Variations.* Springer-Verlag, New York, 1989.

[33] E. A. Dari. *Contribuciones a la triangulación automática de dominios tridimensionales.* PhD thesis, Instituto Balseiro, Bariloche, Argentina, 1994.

[34] B. Delaunay. Sur la sphere vide. In *Classe Sci. Mat. Nat.*, volume VII, pages 793–800. Bull. Acad. Sci. USSR, 1934.

[35] P. Devloo, J. T. Oden, and T. Strouboulis. Implementation of an adaptive refinement technique for the SUPG algorithm. *Computer Methods in Applied Mechanics and Engineering*, 61, 1987.

[36] A. R. Diaz, N. Kikuchi, and J. E. Taylor. A method of grid optimization for finite element methods. *Computer Methods in Applied Mechanics and Engineering*, 41, 1983.

[37] J. Donea. An arbitrary lagrangian-eulerian finite element method for transient fluid-structure interactions. *Computer Methods in Applied Mechanics and Engineering*, 33:689–723, 1982.

[38] N. Dyn and D. Levin. A Butterfly Subdivision Scheme for Surface Interpolation with Tension Control. *AMC Transaction on Graphics*, 9:160–169, 1990.

[39] S. Farestam and R. B. Simpson. A framework for advancing front techniques of finite element mesh generation. *BIT*, 35:210–232, 1995.

[40] J. Fish and T. Belytschko. Elements with embedded localization zones for large deformation problems. *Computers and Structures*, 30(1-2):247–256, 1988.

[41] J. Fish and T. Belytschko. A finite element with a unidirectionally enriched strain field for localization analysis. *Computer Methods in Applied Mechanics and Engineering*, 78(2):181–200, 1990.

[42] P. Fleischmann and S. Selberherr. Three-dimensional Delaunay mesh generator using a modified advancing front approach. In *Proceedings of the 6th. international meshing roundtable*, pages 267–276, Park City, Utah, 1997. Sandia National Laboratories.

[43] L Freitag and C. Ollivier-Gooch. A comparison of tetrahedral mesh improvement techniques. In *Proceedings of the 5th International Meshing Roundtable*, pages 87–100, Pittsburgh, Pennsylvania, October 1996. Sandia National Laboratories.

[44] L. B. Freund. The axial force needed to slide a circular fiber along a hole in an elastic material and impications for fiber pull-out. *Eur. J. Mech., A/Solids*, 11(1):1–19, 1992.

[45] G. Friesecke and G. Dolzmann. Implicit time discretization and global existence for quasi-linear evolution equation with nonconvex energy. *SIAM J. Math. Anal.*, 28:363–380, 1997.

[46] P. L. George and F. Hermeline. Delaunay's Mesh of a Convex Polyhedron in Dimension d. Application to Arbitrary Polyhedra. *International Journal for Numerical Methods in Engineering*, 33:975–995, 1992.

[47] S.T. Grilli and R. Subramanya. Numerical modeling of wave breaking induced by fixed or moving boundaries. *Computational Mechanics*, 17:374–391, 1996.

[48] V. Guillemin and A. Pollack. *Differential Topology.* Prentice-Hall, Englewood Cliffs, N. J., 1974.

[49] C. Hammond. *Introduction to crystallography.* Oxford University Press, 1990.

[50] F. H. Harlow and J. E. Welch. Numerical calculation of time-dependent viscous incompressible flow of fluid with free surface. *Physics of Fluids*, 8:2182–2189, 1965.

[51] K. S. Havner. On the mechanics of crystalline solids. *Journal of the Mechanics and Physics of Solids*, 21:383, 1973.

[52] C. Hazlewood. Approximating constrained tetrahedrizations. *Computer Aided Geometric Design*, 10:67–87, 1993.

[53] R. Hill and J. R. Rice. Constitutive analysis of elastic-plastic crystals at arbitary strains. *Journal of the Mechanics and Physics of Solids*, 20:401, 1972.

[54] C. W. Hirt, J. L. Cook, and T. D. Butler. A lagrangian method for calculation of the dynamics of an incompressible fluid with a free surface. *Journal of Computational Physics*, 5:103, 1970.

[55] C. M. Hoffmann. *Geometric and Solid Modeling.* Morgan Kaufmann Publishers, San Mateo, California, 1989.

[56] T. Y. Hou and X. H. Wu. A multiscale finite element method for elliptic problems in composite materials and porous media. *Journal of Computational Physics*, 134(1):169–189, 1997.

[57] A. Huerta and F. Casadei. New ale applications in non-linear fast-transient solid dynamics. *Engineering Computations*, 11:317–345, 1994.

[58] T. J. R. Hughes. Analysis of transient algorithms with particular reference to stability behavior. In T. Belytschko and T. J. R. Hughes, editors, *Computational Methods for Transient Analysis*, pages 67–155. North-Holland, 1983.

[59] T. J. R. Hughes. Multiscale phenomena – green's functions, the dirichlet to neumann formulation, subgrid scale models and the origins of stabilized methods. *Computer Methods in Applied Mechanics and Engineering*, 127(1-4):387–401, 1995.

[60] D. Hull and D. J. Bacon. *Introduction to dislocations*, volume 37 of *International Series on Materials Science and Technology.* Elsevier Science Inc., 3rd edition, 1984.

[61] H. Jin and R. I. Tanner. Generation of Unstructured Tetrahedral Meshes by Advancing Front Technique. *International Journal for Numerical Methods in Engineering*, 36:1805–1823, 1993.

[62] H. Jin and N. E. Wiberg. Two-Dimensional Mesh Generation, Adaptive Remeshing and Refinement. *International Journal for Numerical Methods in Engineering*, 29:1501–1526, 1990.

[63] B. Joe. Three-dimensional triangulations from local transformations. *SIAM Journal on Scientific and Statistical Computing*, 10:718–741, 1989.

[64] B. Joe. Construction of three-dimensional improved-quality triangulations using local transformations. *SIAM Journal on Scientific Computing*, 16(6):1292–1307, November 1995.

[65] M. Kawahara and A.Anjyu. Lagrangian finite element method for solitary wave propagation. *Computational Mechanics*, 3:299–307, 1988.

[66] R.V. Kohn. The relaxation of a double-well energy. *Continuum Mechanics and Thermodynamics*, 3:193–236, 1991.

[67] E.V. Laitone. The second approximation to cnoidal waves. *Journal of Fluid Mechanics*, 9:430–, 1960.

[68] T. S. Lau and S. H. Lo. Finite element mesh generation over analytical curved surfaces. *Computers and Structures*, 59(2):301–309, 1996.

[69] E. H. Lee. Elastic-plastic deformation at finite strains. *Journal of Applied Mechanics*, 36:1, 1969.

[70] N. S. Lee and K. J. Bathe. Error indicators and adaptive remeshing in large deformation finite element analysis. *Finite Elements in Analysis and Design*, 16:99–139, 1993.

[71] Y. Leroy and M. Ortiz. Finite element analysis of strain localization in frictional materials. *International Journal for Numerical and Analytical Methods in Geomechanics*, 13(1):53–74, 1989.

[72] Y. Leroy and M. Ortiz. Localization analysis under dynamic loading. *Institute of Physics Conference Series*, 102:257–265, 1989.

[73] Y. Leroy and M. Ortiz. Finite element analysis of transient strain localization phenomena in frictional materials. *International Journal for Numerical and Analytical Methods in Geomechanics*, 14(2):93–124, 1990.

[74] Y. Leroy, M. Ortiz, and A. Needleman. An overview of finite element methods for the analysis of strain localization. In J. Mazars and Z. P. Bazant, editors, *Cracking and Damage: Strain Localization and Size Effect*, pages 269–294. Elsevier Applied Science, New York, NY, 1989.

[75] A. Liu and B. Joe. Relation between tetrahedron shape measures. *BIT*, 34:268–287, 1994.

[76] S. H. Lo. Finite element mesh generation over curved surfaces. *Computers and Structures*, 29(5):731–742, 1988.

[77] S. H. Lo. Volume discretization into tetrahedra-ii. 3d triangulation by advancing front approach. *Computers and Structures*, 39(5):501–511, 1991.

[78] S. H. Lo. Volume discretization into tetrahedra-ii. verification and orientation of boundary surfaces. *Computers and Structures*, 39(5):493–500, 1991.

[79] S. H. Lo. Automatic mesh generation over intersecting surfaces. *International Journal for Numerical Methods in Engineering*, 38:943–954, 1995.

[80] R. Löhner. Some Useful Data Structures for the Generation of Unstructured Grids. *Communications in Applied Numerical Methods*, 4:123–135, 1988.

[81] R. Löhner. Finite elements in CFD: grid generation, adaptivity and parallelization. In *AGARD Report*, volume 787, chapter 8. NATO, 1992.

[82] R. Löhner. Regridding surface triangulations. *Journal of Computational Physics*, 126:1–10, 1996.

[83] R. Löhner and P. Parikh. Generation of Three-Dimensional Unstructure Grids by the Advancing-Front Method. *International Journal for Numerical Methods in Fluids*, 8:1135–1149, 1988.

[84] J. Lubliner. On the Thermodynamic Foundations of Non-Linear Solid Mechanics. *International Journal of Non-Linear Mechanics*, 7:237–254, 1972.

[85] J. Lubliner. On the Structure of the Rate Equations of Materials with Internal Variables. *Acta Mechanica*, 17:109–119, 1973.

[86] G. Maier. Some theorems for plastic strain rates and plastic strains. *Journal de Mécanique*, 8:5, 1969.

[87] J. Mandel. Plasticité classique et viscoplasticité. Technical report, Lecture Notes, Int. Centre for Mech. Sci., Udine, Berlin:Springer, 1972.

[88] M. Mantyla. *An Introduction to Solid Modeling.* Computer Science Press, Rockwille, Maryland, 1988.

[89] J. E. Marsden and T. J. R. Hughes. *Mathematical foundations of elasticity.* Prentice-Hall, Englewood Cliffs, N.J., 1983.

[90] J. B. Martin and A. R. S. Ponter. A note on a work inequality in linear viscoelasticity. *Quarterly of Applied Mathematics*, 24:161, 1966.

[91] T. D. Marusich and M. Ortiz. Modelling and Simulation of High-Speed Machining. *International Journal for Numerical Methods in Engineering*, 38:3675–3694, 1995.

[92] D. J. Mavriplis. An advancing-front Delaunay triangulation algorithm designed for robustness. paper 93-0671, AIAA, 1993.

[93] D. J. Mavriplis. Unstructured mesh generation and adaptivity. Technical Report 95-26, NASA, 1995.

[94] M. L. Merriam. An efficient advancing-front algorithm for Delaunay triangulation. paper 91-0792, AIAA, 1991.

[95] R. D. Mindlin. Force at a point in the interior of a semi-infinite solid. *Physics*, 7:195, 1936.

[96] P. Möller and P. Hansbo. On advancing front mesh generation in three dimensions. *International Journal for Numerical Methods in Engineering*, 38:3551–3569, 1995.

[97] R. Muki and E. Steinberg. On the diffusion of an axial load from an infinite cylindrical bar embedded in an elastic medium. *International Journal of Solids and Structures*, 5:587–605, 1969.

[98] R. Muki and E. Steinberg. Elastostatic load-transfer to a half-space from a partially embedded axially loadad rod. *International Journal of Solids and Structures*, 6:69–90, 1970.

[99] A. Nacar, A. Needleman, and M. Ortiz. A finite element method for analyzing localization in rate-dependent solids at finite strains. *Computer Methods in Applied Mechanics and Engineering*, 73(3):235–258, 1989.

[100] A. Needleman. Material rate-dependence and mesh sensitivity in localization. *Computer Methods in Applied Mechanics and Engineering*, 67(1):69–85, 1988.

[101] J. Oliver. Modeling strong discontinuities in solid mechanics via strain softening. *International Journal for Numerical Methods in Engineering*, 39(21):3601–3623, 1996.

[102] M. Ortiz, Y. Leroy, and A. Needleman. A finite element method for localized failure analysis. *Computer Methods in Applied Mechanics and Engineering*, 61(2):189–214, 1987.

[103] M. Ortiz and A. Pandolfi. A class of cohesive elements for the simulation of three-dimensional crack propagation. Submitted for publication, September 1997.

[104] M. Ortiz and A. Pandolfi. Solid modeling aspects of three-dimensional fragmentation. Submitted for publication, March 1998.

[105] M. Ortiz and J. J. Quigley. Adaptive Mesh Refinement in Strain Localization Problems. *Computer Methods in Applied Mechanics and Engineering*, 90:781–804, 1991.

[106] M. Ortiz and E. A. Repetto. Nonconvex energy minimization and dislocation structures in ductile single crystals. *Journal of the Mechanics and Physics of Solids*, 1998.

[107] V. N. Parthasarathy, C. M. Graichen, and A. F. Hathaway. A Comparison of Tetrahedron Quality Measures. *Finite Elements in Analysis and Design*, 15:225–261, 1993.

[108] J. Peraire and J. Peiro. Adaptive Remeshing for Three-Dimensional Compressible Flow Computations. *Journal of Computational Physics*, 103:269–285, 1992.

[109] J. Peraire, J. Peiro, L. Formaggia, K. Morgan, and O.C. Zienkiewicz. Finite Element Euler Computations in Three Dimensions. *International Journal for Numerical Methods in Engineering*, 26:2135–2159, 1988.

[110] J. Peraire, M. Vahdati, K. Morgan, and O. C. Zienkiewicz. Adaptive Remeshing for Compressible Flow Computations. *Journal of Computational Physics*, 72:449–466, 1987.

[111] R. Perucchio, M. Saxena, and A. Kela. Automatic mesh generations from solid models based on recursive spatial decompositions. *International Journal for Numerical Methods in Engineering*, 28:2469–2501, 1989.

[112] P. Ponte-Castañeda. Nonlinear composites. *Advances in Applied Mechanics*, 34:171–301, 1998.

[113] R. Radovitzky and M. Ortiz. Lagrangian finite element analysis of newtonian fluid flows. *To appear in International Journal for Numerical Methods in Engineering*, 1997.

[114] R. Radovitzky and M. Ortiz. Error estimation and adaptive meshing in strongly nonlinear dynamic problems. *Computer Methods in Applied Mechanics and Engineering*, 1998.

[115] R. Radovitzky and M. Ortiz. Tetrahedral mesh generation based on node insertion in crystal lattice arrangements and advancing-front-Delaunay triangulation. In preparation, 1998.

[116] V.T. Rajan. Optimality of the Delaunay triangulation in R^d. *Discrete & Computational Geometry*, 12:189–202, 1994.

[117] B. Ramaswamy. Numerical Simulation of Unsteady viscous Free Surface Flow. *Journal of Computational Physics*, 90:396–430, 1990.

[118] B. Ramaswamy and M. Kawahara. Lagrangian finite element analysis applied to viscous free surface flow. *International Journal for Numerical Methods in Fluids*, 7:953–984, 1987.

[119] B. Ramaswamy, M. Kawahara, and T. Nakayama. Lagrangian finite element method for the analysis of two-dimensional sloshing problems. *International Journal for Numerical Methods in Fluids*, 6:659–670, 1986.

[120] A. A. G. Requicha. Representations for Rigid Solids: Theory, Methods and Systems. *Computing Surveys*, 12:437–465, 1980.

[121] J. R. Rice. Inelastic constitutive relations for solids: an internal-variable theory and its applications to metal plasticity. *Journal of the Mechanics and Physics of Solids*, 19:433, 1971.

[122] J. R. Rice. Continuum mechanics and thermodynamics of plasticity in relation to microscale deformation mechanisms. In A.S. Argon, editor, *Constitutive Equations in Plasticity*, pages 23–79, Cambridge, Mass, 1975. MIT Press.

[123] D. Rypl and P. Krysl. Triangulation of 3d surfaces. *Engineering with computers*, 13(2):87–98, 1997.

[124] H. Samet. *The Design and Analysis of Spatial Data Structures.* Addison-Wesley, New York, 1990.

[125] W. J. Schroeder and M. S. Shephard. Geometry-based fully automatic mesh generation and the Delaunay triangulation. *International Journal for Numerical Methods in Engineering*, 26:2503–2515, 1988.

[126] W. J. Schroeder and M. S. Shephard. A combined octree/Delaunay method for fully automatic 3-d mesh generation. *International Journal for Numerical Methods in Engineering*, 29:37–55, 1990.

[127] M. S. Shephard and M. K. Georges. Automatic Three-Dimensional Mesh Generation by the Finite Octree Technique. *International Journal for Numerical Methods in Engineering*, 32(4):709–749, 1991.

[128] J. C. Simo and F. Armero. Geometrically nonlinear enhanced strain mixed methods and the method of incompatible modes. *International Journal for Numerical Methods in Engineering*, 33(7):1413–1449, 1992.

[129] J. F. Soechting and R. H. Lance. A bounding principle in the theory of work-hardening plasticity. *Journal of Applied Mechanics*, 36:228, 1969.

[130] T. A. Standish. *Data Structures, Algorithms and Software Principles in C.* Addison-Wesley, New York, 1995.

[131] M. Tanemura, T. Ogawa, and N. Ogita. A new algorithm for three-dimensional Voronoi tesselation. *Journal of Computational Physics*, 51(2):191–207, 1983.

[132] C. Teodosiu. A dynamic theory of dislocations and its applications to the theory of the elastic-plastic continuum. In J. A. Simmons, editor, *Conf. Fundamental Aspects of Dislocation Theory*, volume 2, page 837, Washington, 1969. Natl. Bureau of Standards Special Publication.

[133] L. van Hove. Sur le signe de la variation seconde des intégrales multiples à plusieurs fonctions inconnues. *Koninkl. Belg. Acad., Klasse der Wetenschappen, Verhandelingen*, 24, 1949.

[134] R. Verfürth. *A Review of A Posteriori Error Estimation and Adaptive Mesh-Refinement Techniques.* John Wiley & Sons and B. G. Teubner Publishers, New York, NY, 1996.

[135] K. Vorspohl, J. Mertes, R. Zschiesche, H. D. Lutter, and R. Drumm. Time-dependence of hardness of cold cure molded flexible foams and its importance for system development. *Journal of Cellular Plastics*, 30(4):361–374, 1994.

[136] D. F. Watson. Computing the n -Dimensional Delaunay Tesslation with Application to Voronoi Polytopes. *The Computer Journal*, 24(2):167–172, 1981.

[137] N. P. Weatherill and O. Hassan. Efficient three-dimensional Delaunay triangulation with automatic point creation and imposed boundary constraints. *International Journal for Numerical Methods in Engineering*, 37:2005–2039, 1994.

[138] N.P. Weatherill. The reconstruction of boundary contours and surfaces in arbitrary unstructured triangular and tetrahedral grids. *Engineering Computations*, 13(8):66–81, 1996.

[139] G. B. Whitham. *Linear and nonlinear waves.* Pure and applied mathematics. Wiley, New York, 1974. A Wiley-Interscience publication.

[140] J. P. Wright and A. G. Jack. Aspects of three-dimensional constrained Delaunay meshing. *International Journal for Numerical Methods in Engineering*, 37:1841–1861, 1994.

[141] M. Wronski. A new hypoelastic model of the mechanical behavior of polyurethane foams. *Computational Materials Science*, 5(1-3):271–276, 1996.

[142] M. A. Yerry and M. S. Shephard. Automatic mesh generation for three-dimensional solids. *Computers and Structures*, 20:211–223, 1985.

[143] O. C. Zienkiewicz and J. Z. Zhu. A Simple Error Estimator and Adaptive Procedure for Practical Engineering Analysis. *International Journal for Numerical Methods in Engineering*, 24:337–357, 1987.

[144] O. C. Zienkiewicz and J. Z. Zhu. A simple error estimator and adaptive procedure for practical engineering analysis. *International Journal for Numerical Methods in Engineering*, 24, 1987.

[145] D. Zorin, P. Schroeder, and W. Sweldens. Interpolating subdivision for meshes with arbitrary topology. In *SIGGRAPH 96'*, 1996.